



# University of HUDDERSFIELD

## University of Huddersfield Repository

Bruton, David

Investigation of a Compact Accelerator for Radioisotope Production

### Original Citation

Bruton, David (2018) Investigation of a Compact Accelerator for Radioisotope Production. Doctoral thesis, University of Huddersfield.

This version is available at <http://eprints.hud.ac.uk/id/eprint/34972/>

The University Repository is a digital collection of the research output of the University, available on Open Access. Copyright and Moral Rights for the items on this site are retained by the individual author and/or other copyright owners. Users may access full items free of charge; copies of full text items generally can be reproduced, displayed or performed and given to third parties in any format or medium for personal research or study, educational or not-for-profit purposes without prior permission or charge, provided:

- The authors, title and full bibliographic details is credited in any copy;
- A hyperlink and/or URL is included for the original metadata page; and
- The content is not changed in any way.

For more information, including our policy and submission procedure, please contact the Repository Team at: [E.mailbox@hud.ac.uk](mailto:E.mailbox@hud.ac.uk).

<http://eprints.hud.ac.uk/>

# Investigation of a Compact Accelerator for Radioisotope Production

*University of*  
**HUDDERSFIELD**

David Bruton

Centre for Doctoral Training in Next Generation Accelerators

International Institute for Accelerator Applications

University of Huddersfield

A thesis submitted to the University of Huddersfield  
in partial fulfilment of the requirements for the degree of

*Doctor of Philosophy*

September 2018

---

## Copyright

i. The author of this thesis (including any appendices and/or schedules to this thesis) owns any copyright in it (the “Copyright”) and he/she has given The University of Huddersfield the right to use such Copyright for any administrative, promotional, educational and/or teaching purposes.

ii. Copies of this thesis, either in full or in extracts, may be made only in accordance with the regulations of the University Library. Details of these regulations may be obtained from the Librarian. This page must form part of any such copies made.

iii. The ownership of any patents, designs, trade marks and any and all other intellectual property rights except for the Copyright (the “Intellectual Property Rights”) and any reproductions of copyright works, for example graphs and tables (“Reproduction”), which may be described in this thesis, may not be owned by the author and may be owned by third parties. Such Intellectual Property Rights and Reproductions cannot and must not be made available for use without the prior written permission of the owner(s) of the relevant Intellectual Property Rights and/or Reproductions.

---

## Abstract

In this thesis the design and performance of a non-linear non-scaling Fixed Field Alternating Gradient (FFAG) accelerator is described. The imagined application of the design is for radioisotope production and in particular the production of  $^{99m}\text{Tc}$  and  $^{211}\text{At}$ . The performance of the design in combination with an internal target and recycled beam, is also investigated as a potential way to increase isotope yields.

The basic design consists of four separate radial sector magnets and two RF cavities. The design differs from a conventional cyclotron in that the edge angles have been optimised with the field gradient to produce a lattice that is isochronous to  $\pm 0.15\%$  and has stabilised tunes.

Simulations conducted using the OPAL code showed that the dynamic apertures are large, peaking at 150 and  $41.4 \pi \text{ m mrad}$  in the horizontal and vertical planes respectively. Acceleration with protons is possible at up to the 5th harmonic with 100 kV/turn accelerating gradient and at the 1st harmonic for alpha particles.

Space charge simulations suggested strong performance under high current conditions. A proton beam of 20 mA was simulated with 2.3% losses, dropping to 0% losses at 4 mA. Alpha particle beams were simulated with beam currents of up to  $800 \mu\text{A}$  with minimal losses. The best harmonic to operate at for handling high currents was found to be either the 2nd or 3rd.

Simulations of the internal target demonstrated that ionisation cooling has an effect even with high Z materials. Two aspects were identified as key to increasing beam survival; the vertical aperture and cooling the beam longitudinally. It was found that increasing the vertical aperture by  $\pm 1 \text{ cm}$  could double the beam survival time. Additionally by using a combination of a wedge shaped target and RF stabilisation to cool the beam longitudinally, a 140% increase in beam survival time was achieved.

Finally several iterations of the design were created investigating possible improvements to the design including tune adjustment by introducing a magnet shift, a dual proton alpha particle design and a compact 35 MeV design.

---

## Acknowledgements

I would like to thank the EPSRC for their financial assistance without which this PhD would not have been possible.

I would also like to thank my wife Zara for her unending support and proofreading skills, my supervisor Roger Barlow for his advice and patience, Jordan Taylor and Haroon Rafique for keeping me sane for four years, and the NGACDT cohort for many shenanigans.

*I dedicate this thesis to my family; past, present and future.*

# Contents

<b>List of Figures</b>	<b>9</b>
<b>List of Tables</b>	<b>13</b>
<b>1 Beam Dynamics in Cyclotrons and Synchrotrons</b>	<b>15</b>
1.1 Charged Particle Motion in a Magnetic Field . . . . .	15
1.1.1 Betatron Motion and Tunes . . . . .	16
1.1.2 Dispersion . . . . .	17
1.1.3 Chromaticity . . . . .	17
1.1.4 Emittance . . . . .	17
1.2 Acceleration . . . . .	19
1.2.1 Electrostatic Acceleration . . . . .	19
1.2.2 RF Acceleration . . . . .	20
1.2.2.1 Phase Stability . . . . .	21
1.2.2.2 Transit Time Factor . . . . .	21
1.3 Cyclotrons . . . . .	22
1.3.1 The Classical Cyclotron . . . . .	22
1.3.2 The Isochronous Cyclotron . . . . .	23
1.3.3 AVF Cyclotrons . . . . .	24
1.3.4 Spiral Sector Cyclotrons . . . . .	25
1.3.5 Synchrocyclotrons . . . . .	26
1.3.6 Injection . . . . .	26
1.3.6.1 Axial Injection . . . . .	27
1.3.6.2 Radial Injection . . . . .	29
1.3.6.3 Beam Bunching . . . . .	29
1.3.7 Extraction . . . . .	32

1.3.7.1	Internal Target . . . . .	32
1.3.7.2	Charge Exchange . . . . .	32
1.3.7.3	Electrostatic Extraction . . . . .	34
1.4	Synchrotrons . . . . .	34
1.4.1	Lattice Structures . . . . .	35
1.4.2	Synchrotron Motion . . . . .	36
1.5	Summary . . . . .	37
<b>2</b>	<b>FFAG Dynamics and Some Notable Examples</b>	<b>39</b>
2.1	FFAG Dynamics . . . . .	39
2.1.1	Scaling FFAG Dynamics . . . . .	40
2.1.2	Non-Scaling FFAG Dynamics . . . . .	40
2.2	Existing FFAGs . . . . .	42
2.2.1	POP . . . . .	42
2.2.2	KEK/KURRI . . . . .	43
2.2.3	ERIT . . . . .	44
2.2.4	EMMA . . . . .	46
2.2.5	Proposed FFAG Designs . . . . .	47
2.2.5.1	PAMELA . . . . .	48
2.2.5.2	e-RHIC and CBETA . . . . .	50
2.3	Conclusions . . . . .	52
<b>3</b>	<b>Radioisotopes</b>	<b>53</b>
3.1	Radioisotopes . . . . .	53
3.1.1	Medical Applications . . . . .	53
3.1.2	Accelerator Production of Radioisotopes . . . . .	58
3.1.3	Targets . . . . .	59
3.1.3.1	Internal Targets . . . . .	59
3.1.3.2	External Targets . . . . .	60
3.1.3.3	Beam Target Interactions . . . . .	61
3.2	Conclusions . . . . .	62
<b>4</b>	<b>Compact Proton FFAG</b>	<b>65</b>
4.1	Accelerator Design Overview . . . . .	65

4.2	Computational Investigation of the Design . . . . .	68
4.2.1	COSY INFINITY . . . . .	68
4.2.2	OPAL . . . . .	68
4.2.3	PyZgoubi . . . . .	69
4.2.4	Closed Orbits, ToF, Tunes and Dynamic Aperture . . . . .	71
4.2.5	Acceleration . . . . .	75
4.2.6	Helium Acceleration . . . . .	79
4.2.7	Field Errors . . . . .	82
<b>5</b>	<b>Space Charge Studies</b>	<b>87</b>
5.1	Proton Dynamics Under Space Charge . . . . .	87
5.2	Space Charge Effect in He <sup>2+</sup> Beams . . . . .	93
5.3	Conclusions . . . . .	97
<b>6</b>	<b>Internal Target Studies</b>	<b>99</b>
6.1	Ionisation Cooling . . . . .	100
6.2	Computational Investigation of an Internal Target . . . . .	102
6.3	Longitudinal Cooling . . . . .	105
6.4	Conclusions . . . . .	108
<b>7</b>	<b>Further Design Iterations</b>	<b>111</b>
7.1	Introducing an Effective Spiral Angle to Avoid Resonance Crossings . .	111
7.2	A Dual Particle Design Optimised for Both Protons and Alpha Particles	115
7.3	A Field Map Optimised for Alpha Particles . . . . .	119
7.4	Compact 35 MeV Design . . . . .	120
7.5	Conclusions . . . . .	125
<b>8</b>	<b>Summary and Conclusions</b>	<b>127</b>
8.1	Future Work . . . . .	129
8.2	Conclusions . . . . .	130
	<b>References</b>	<b>131</b>

Total word count: 31,433

# List of Figures

1.1	The phase space ellipse in $x x'$ the area of which describes the emittance. The extents of the ellipse relates to the Twiss functions $\alpha \beta$ and $\gamma$ . . . .	18
1.2	The basic concept of a cyclotron as described by Lawrence in his original patent from 1934 . . . . .	22
1.3	Diagram of the spiral sector concept. The angle between the magnet centre and the radius is the spiral angle $\delta$ . . . . .	25
1.4	Schematic of a magnetic mirror inflector. The beam is reflected $90^\circ$ by the magnetic field between the high voltage electrode and the grid. . . .	28
1.5	Diagram of a charge exchange injection system. A -Yoke, B -Cryostat, C -Carbon stripping foil, D -Steering magnet, E -Injection radius, F -Inner equilibrium radius, G -Effective field boundary, H -Matching radius. . .	30
1.6	Bunching efficiency of different types of buncher. The maximum bunching efficiency is achieved with the double drift buncher. . . . .	31
1.7	Charge exchange extraction diagram. By adjusting the position of the extraction foil different energies can be made to extract and converge on a single point. . . . .	33
1.8	Diagram of a FODO cell. Blue line is the beam envelope, red line is the path of an individual particle as it traverses the lattice . . . . .	36
2.1	RF phase space structure with serpentine channel looping around the stationary buckets (right) and highlight of the serpentine channel (left).	42
2.2	POP lattice made up of 8 DFD cells. . . . .	43
2.3	The KURRI main ring FFAG lattice made up of 12 DFD cells. The $H^-$ charge exchange scheme and first orbit are shown. . . . .	44
2.4	Eight FDF cells make up the ERIT lattice. . . . .	45
2.5	The EMMA doublet cell and cavity. The offset between quadrupoles creates the bending field. . . . .	47
2.6	PAMELA Layout showing the proton ring (inner) and carbon ring (outer).	49

## LIST OF FIGURES

---

2.7	The matching scheme for eRHIC that adiabatically removes the quadrupole offset bringing the beams onto a single orbit for the straight sections. . .	50
2.8	Floor plan of the CBETA accelerator featuring FFAG arcs, a superconducting ERL and phase matching sections. . . . .	51
3.1	Cross-sections of competing reaction for alpha particles incident on $^{209}\text{Bi}$ . Above 30 MeV production of $^{210}\text{At}$ and $^{210}\text{Po}$ begin to pollute the $^{211}\text{At}$ sample. . . . .	55
3.2	Cross-sections of competing reactions from the proton irradiation of $^{100}\text{Mo}$ . Energies of up to 20 MeV are commonly used for $^{99m}\text{Tc}$ production, however the higher the energy used, the greater the level of impurities. . . . .	57
3.3	Diagram of a typical internal target set up. The target would be placed in such a way that the target material is at an angle to the beam, spreading the beam power over a greater area. . . . .	60
3.4	Diagram of a gas target. The target chamber widens to account for beam growth from scattering. . . . .	61
4.1	General layout of the design, with the position of magnets in red and RF cavity position in green. Two sectors are left empty and can be used to locate injection/extraction devices. . . . .	66
4.2	Closed Orbits for protons from 75 keV (at 89.4 mm) to 28 MeV (at 1686.5 mm). . . . .	67
4.3	Time of flight variation as a function of energy. Maximum variation is $\pm 0.15\%$ and integrated variation is 0.632 %. The spread is small enough to allow CW operation. . . . .	71
4.4	The betatron tunes calculated as in OPAL, COSY and pyZgoubi. All three show good agreement with each other, showing the same features such as depressed vertical tune at low energy and resonance crossing. . .	72
4.5	Dynamic Apertures in both horizontal and vertical planes. The smallest DA's are at injection (75keV) and the largest at 12.5 MeV. . . . .	73
4.6	The RF phase space for various cavity voltages at the first harmonic. At 20kV/turn a acceleration channel to 28 MeV opens up but with very limited phase acceptance. For greater phase acceptance and reduced energy spread a voltage of $>100\text{kV/turn}$ or more is needed. . . . .	74

4.7	The RF phase space for different harmonics at 200kV/Turn. As the harmonic number increases so does the phase slip, so a compromise must be made between the harmonic number and the accelerating efficiency. Otherwise increasing the accelerating voltage can compensate for the increased phase slip. . . . .	76
4.8	Turn Separation for voltages from 50-400 kV/Turn. The separation reduces with increased energy making extraction difficult. Increasing the accelerating voltage increases the separation linearly. . . . .	77
4.9	Effect of increasing the longitudinal length of the beam on the final radial emittance of the beam. Crosses are simulation result, line is a $y \propto \tan(x)$ fit. . . . .	78
4.10	Emittances as a function of accelerating voltage. Lower voltages result in higher emittances. At around 22 MeV there is a artefact that is causing significant growth for voltages less than 250 kV/turn. . . . .	79
4.11	Beam rigidity of protons and $\text{He}^{2+}$ in the energy range up to 35 MeV. At 28 MeV the rigidities vary by less than 0.9 %. . . . .	80
4.12	Comparison of betatron tunes and dynamic apertures for protons and $\text{He}^{2+}$ . . . . .	81
4.13	RF phase space for $\text{He}^{2+}$ ions at different harmonics and voltages. By the second harmonic an accelerating gradient of at least 300kV/Turn is required. . . . .	82
4.14	Emittances and energy spread for Alphas at 1 <sup>st</sup> (Blue Line) and 2 <sup>nd</sup> (Purple Line) harmonics for 300 kv/Turn. . . . .	83
4.15	Dynamic aperture distortion and restriction for a random field error . .	84
4.16	Average dynamic apertures for a dipole component field error . . . . .	85
5.1	Emittances for a 20 mA beam current. . . . .	89
5.2	Beam losses on a $\pm 20\text{mm}$ aperture. Losses are first observed at 8 mA and continue to grow, reaching 2.9% by 20mA. . . . .	91
5.3	Radial emittances for a 5mA, 2mm spherical bunch at varying harmonics. The 2nd and 3rd harmonics produce the lowest final emittances. . . . .	92
5.4	Longitudinal shape of a proton bunch on the 150th turn at increasing beam currents. The development of filamentation and micro bunching under strong longitudinal space charge forces is observed. . . . .	94
5.5	Radial and vertical emittances for a $\text{He}^{2+}$ beam at various beam currents.	95
5.6	Beam losses on a $\pm 20\text{mm}$ aperture. Losses are first observed at 800 $\mu\text{A}$ and continue to grow, reaching 33% by 10mA. . . . .	96

## LIST OF FIGURES

---

5.7	Longitudinal shape of a $\text{He}^{2+}$ bunch on the 60th turn at increasing beam currents. The development of filamentation and micro bunching under strong longitudinal space charge forces is observed. . . . .	97
6.1	Visualisation of how Ionisation cooling works to reduce the angle of the momentum vector through energy loss and re-acceleration . . . . .	100
6.2	How different factor affect the efficiency of Ionisation cooling. . . . .	102
6.3	Emittance growth with and without ionisation cooling showing the emittance suppression effect. . . . .	102
6.4	Effect of thickness on beam survival. Total distance traversed through target over all turns is independent of target thickness. . . . .	103
6.5	Effect of vertical aperture on beam survival. Increasing the aperture leads to significantly improved survival. . . . .	104
6.6	Location of losses in the machine from scattering through the target. Losses are concentrated in areas where the vertical beta function is large.	105
6.7	Comparison of loss control effectiveness between wedge target and RF stabilisation. The combined use of a wedge target and RF stabilisation gives a significant improvement over either one used on its own. . . . .	106
6.8	Effect of RF stabilisation on beam survival and the energy spread of the beam. Maximum beam survival is found at 60kV and a significant reduction in the energy spread of the beam is observed. . . . .	107
6.9	Effect on integrated beam current on target for different phases and voltages. The phase is relative to the phase of the main (accelerating) RF cavities. . . . .	108
7.1	The new magnet configuration introduces a spiral angle ( $\delta$ ) into the design. The spiral angle is radius dependent and its contribution to the tunes go by $2 \times \tan^2(\delta)$ creating an even steeper drop off in its effect with radius. . . . .	112
7.2	Comparison of tune maps for the original and tune modified designs. The modified tunes are higher and no longer pass through any resonances.	113
7.3	Beta functions of the modified design. The new vertical beta function is not symmetric creating a alternating gradient structure. . . . .	114
7.4	RF spaces for protons and alpha particles on field maps optimised for each particle respectively. . . . .	116

7.5	Comparison of the magnetic field of the new dual proton/alpha design with the original. The new field varies from the original by no more than $\pm 0.005$ T. . . . .	117
7.6	RF space for protons and alpha particles at the 1st and 3rd harmonics. The acceleration channel to 28 MeV is lost at higher harmonics. . . . .	118
7.7	Magnetic field for the dedicated $\text{He}^{2+}$ design. . . . .	119
7.8	RF space at the 8th harmonic and tune map for the dedicated alpha field map. The phase acceptance is now around $100^\circ$ compared to the original that could not be accelerated at all on the 8th harmonic. The vertical tune is now lower than in the original design and no longer crosses an integer resonance. . . . .	120
7.9	Comparison of the magnetic fields of the Compact 35 MeV design and the original. . . . .	121
7.10	The tunes and beta functions for the new design. Both are very similar to those of the original design. The beta functions are a little smaller due to the higher magnetic fields. . . . .	122
7.11	Radial and vertical emittances for increasing beam current at 1st harmonic.	123
7.12	Effect of harmonic number on radial emittance for different beam lengths.	123
7.13	Beam profiles for the last 2 turns under normal conditions and when a coherent oscillation has been induced. The orbit separation is significantly improved by the oscillations, easing extraction. . . . .	124

## List of Tables

3.1	Table of radioisotopes that are commonly used in brachytherapy. . . . .	54
3.2	Table of potential alpha emitting radioisotopes for brachytherapy. $^{211}\text{At}$ is of particular interest due to its half-life and its single alpha decay. . . . .	54
3.3	Table of common imaging isotopes that can be produced with a particle accelerator. . . . .	56

## LIST OF TABLES

---

# 1

## Beam Dynamics in Cyclotrons and Synchrotrons

In this thesis the characteristics and performance of a cyclotron type Fixed Field Alternating Gradient (FFAG) accelerator will be described. The envisioned application for this accelerator design is the production of radioisotopes, in particular  $^{99m}\text{Tc}$  which is discussed in chapter 3. The specifics of FFAG accelerators will be discussed in chapter 2 but before that the basic principles underpinning particle accelerators are discussed below. The fundamentals of charged particle motion in magnetic fields are outlined and common terms and concepts described. The principle of acceleration by electric fields will also be described. As the most common and well established circular accelerators, the beam dynamics of both cyclotrons and synchrotrons are discussed. Particular focus is given to cyclotrons as their dynamics are especially relevant to the design on which this thesis is focused, and most current accelerator based radioisotope production is done using cyclotrons.

### 1.1 Charged Particle Motion in a Magnetic Field

At its simplest, the motion of charged particles in an electromagnetic field is governed by the Lorentz equation:

$$\vec{F} = q(\vec{E} + \vec{x} \times \vec{B}), \quad (1.1)$$

where  $q$  is the particle charge,  $\vec{x}$  is the particle velocity,  $\vec{E}$  is the electric field component and  $\vec{B}$  is the magnetic field. With this the trajectory of a charged particle in a magnetic field can be calculated. Consider a bending magnet through which a particle is moving

## 1. BEAM DYNAMICS IN CYCLOTRONS AND SYNCHROTRONS

---

in a circular arc. In this case the force of the magnetic field on the particle is acting as the centripetal force, which is given by:

$$F = \frac{\gamma m v^2}{\rho}, \quad (1.2)$$

where  $\gamma$  is the Lorentz factor,  $m$  the particle mass,  $v$  its velocity and  $\rho$  is the bending radius of the trajectory. Combining these equations leads to:

$$B\rho = \frac{\gamma m v}{q} = \frac{p}{q}, \quad (1.3)$$

where  $p$  is the particles momentum.  $B\rho$  is known as the beam rigidity, and is a measure of how difficult it is to bend the beam. From this the field needed to bend a particle through a set angle at any given radius can be calculated.

### 1.1.1 Betatron Motion and Tunes

The ideal path for a particle to follow in an accelerator is known as the reference orbit. A particle that has been displaced from the reference orbit will oscillate around it. This occurs because a displaced particle with the same energy as the reference particle will have the same radius of curvature in a uniform magnetic field, but a displaced origin. The path of the displaced particle and the reference particle must therefore cross before completing a circle. These oscillations are referred to as betatron oscillation [1].

The number of betatron oscillation per turn is called the betatron tune. There is a machine tune in all three planes but only the horizontal and vertical are betatron tunes, as the mechanism driving the longitudinal oscillation is different. For a uniform magnetic field in a classical cyclotron the number of oscillation per turn must be one. If the field is nonuniform then the number of oscillation per turn will be determined by the focusing properties of the magnetic field structure.

The beta function describes the relative magnitude of these oscillations at each point around the machine. Where the beta function is smallest the physical beam size will be at a minimum, and when the beta function is at its largest the beam will be at its maximum physical size. The betatron tunes can be calculated by integrating the inverse beta function around the machine

$$\nu = \frac{1}{2\pi} \int_s^{s+C} \frac{ds}{\beta(s)}, \quad (1.4)$$

where  $\nu$  is the betatron tune,  $\beta(s)$  the beta function,  $s$  is the longitudinal position of

## 1.1 Charged Particle Motion in a Magnetic Field

---

the beam and  $C$  is the circumference of the machine.

### 1.1.2 Dispersion

The beta function describes how a physical displacement of a particle affects its motion. The dispersion function describes how a momentum displacement affects the transverse motion of a particle [2]. A particle that has a momentum that is different from the reference particle will have a different radius of curvature in a magnetic field and so end up with a transverse displacement. The magnitude of this displacement is given by

$$x(s) = D(p, s) \frac{\delta p}{p_0}. \quad (1.5)$$

where  $x(s)$  is the transverse displacement,  $D(p, s)$  is the dispersion function,  $\delta p$  the momentum shift and  $p_0$  is the reference momentum. As dispersion comes from the different bending radius of off-momentum particles it is generated in dipole magnets. As there is no vertical bending of the beam the vertical dispersion should theoretically be zero.

### 1.1.3 Chromaticity

An off-momentum particle will not only experience a transverse shift but also a change in the focusing effects. The strength of the magnetic focusing is stronger for momenta under that of the reference energy and weaker for momenta that are higher. The effect of this is a tune shift, increasing for particles at lower energies and decreasing for higher energies. The tune shift is given in equation 1.6 [3].

$$\Delta Q = \frac{1}{4\pi} \oint \Delta K(s) \beta(s) ds, \quad (1.6)$$

where  $\Delta Q$  is the tune shift,  $\Delta K$  is the change in effective focusing strength and  $\beta$  is the beta function of the machine. This can be corrected by using non-linear fields that more strongly focus larger amplitude particles. The dispersion means that off-momentum particles will have larger amplitudes and so receive the corrective focusing.

### 1.1.4 Emittance

The emittance is a measure of the size of the beam in  $x/x'$  space. As a particle revolves around the machine its transverse position and momentum at a particular point will precess and draw out an ellipse. The area of this ellipse is the emittance. The maximum

## 1. BEAM DYNAMICS IN CYCLOTRONS AND SYNCHROTRONS

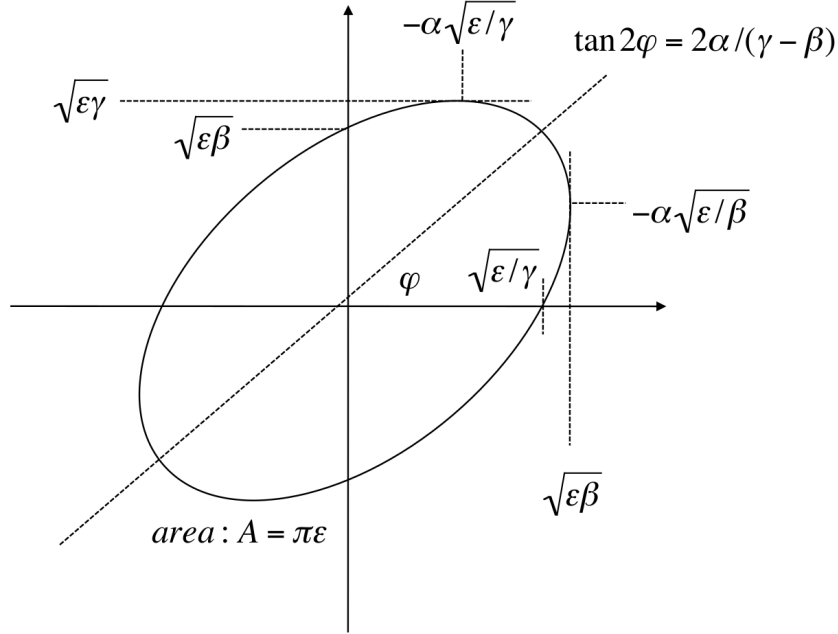


**Figure 1.1:** The phase space ellipse in  $x$   $x'$  the area of which describes the emittance. The extents of the ellipse relates to the Twiss functions  $\alpha$   $\beta$  and  $\gamma$ . Taken from [4].

extents of this ellipse in  $x$  and  $x'$  relate to the lattice functions as shown in fig 1.1 [4]. As such the emittance is a function of the lattice and is therefore invariant ignoring collective effects. It can be calculated from the lattice functions using equation 1.7

$$\epsilon = \gamma x^2 + 2\alpha x x' + \beta x'^2, \quad (1.7)$$

where  $\gamma$ ,  $\alpha$  and  $\beta$  are the Twiss parameters. In a beam each individual particle precesses creating a collection of ellipses of the same angle and ratio of major to minor axis, but with different sizes depending on their displacement.

When looking at a beam it is useful to consider the emittance of an entire bunch rather than individual particles. The most commonly used definition of beam emittance is the RMS emittance which is given by

$$\epsilon_{rms} = \sqrt{\langle x^2 \rangle \langle p_x^2 \rangle - \langle x p_x \rangle^2}. \quad (1.8)$$

As the beam is accelerated the increased momentum decreases the emittance, as the same transverse momentum will result in a smaller angle to the longitudinal momentum vector. To account for this the emittance is often normalised to the beam energy and

is given by

$$\epsilon_{Norm} = \gamma\beta\epsilon, \tag{1.9}$$

where  $\gamma$  and  $\beta$  are the relativistic terms.

## 1.2 Acceleration

Magnetic fields are very effective at bending and controlling the beam but cannot impart any energy to it as magnetic fields always act perpendicularly to the velocity. For this electric fields are required.

### 1.2.1 Electrostatic Acceleration

By passing the beam through an electric field the particles will be accelerated by the potential difference associated with it. The main problem that needs to be overcome is creating the high voltages that are needed. Several different methods have been employed to achieve this.

The Van de Graaff generator produces a large accelerating voltage by accumulating static charge off a rotating belt [5]. The belt is made of an insulating material, usually rubber. As it rotates static charge is transferred on to the belt, which then via the rotation mechanically transports the charge to the electrode at the top of the generator. A metal comb inside the electrode removes the charge from the belt. The charge is stored on the outside of the electrode which is shaped as a hollow sphere. Gauss's law says that the electric field inside a shell of charge is zero and so despite the build up of charge the field at the centre where the charge is exchanged remains small. This allows for the build up of a large amount of charge over time. This method was used in early linear accelerators including the Nuclear Structure Facility at Daresbury which achieved a 30 MV potential [6].

Although effective, the Van de Graaff generator is a large and heavy device and a lighter more compact means of generating large DC voltages was sought. This was achieved by using the Cockcroft-Walton generator [7]. A voltage multiplier circuit consisting of a network of capacitors and diodes is used to convert a low voltage AC input into a high voltage DC output. At each stage the capacitor is charged during one half of the cycle. During the second half of the cycle when the polarity is reversed the diodes prevent the charge from flowing back to ground and so instead it is driven to the next stage of the multiplier. In this way a potential difference is created between

## 1. BEAM DYNAMICS IN CYCLOTRONS AND SYNCHROTRONS

---

each stage such that the potential difference from the last stage to ground is

$$V_O = 2NV_P, \quad (1.10)$$

where  $V_O$  is the output voltage,  $N$  is the number of stages and  $V_P$  is the peak voltage of the AC driving voltage.

One technique commonly used with electrostatics is tandem acceleration [8]. Normally a charged particle will only be accelerated down the potential gradient towards the high voltage electrode. If the particle charge state can be changed as it passes the high voltage electrode it will be repelled by it and accelerated further. This can effectively double the energy gain from the same potential. A foil made of carbon is usually used to strip the electrons from the nucleus as the ion passes through it. The electrodes are commonly housed in a high voltage tank filled with a dielectric material to prevent electrostatic break down. Both Cockcroft-Walton and Van de Graaff generators are commonly used with the tandem accelerator setup [9] [10]. A common application of tandem accelerators is ion implantation as the required energy is easily achievable with this technology and the capital and running cost of tandem accelerators is relatively small [11].

### 1.2.2 RF Acceleration

Electrostatic accelerators are limited by dielectric breakdown under large accelerating voltages. This can be circumvented by switching the polarity of the voltage on the electrode as the particle traverses it. The particle then sees another accelerating voltage to the next electrode. Much smaller voltages can now be used as only the voltage between the individual electrodes needs to be held off, not the total voltage seen by the particle. Sinusoidal waves are used as they are easier to create than square waves and so the voltage varies as

$$V = V_0 \cos \phi. \quad (1.11)$$

where  $V_0$  is the peak voltage and  $\phi$  is the RF phase equal to  $\omega t$ . The frequencies used are similar to those used in radio broadcasts and so this method of acceleration is known as Radio Frequency (RF) acceleration.

The use of resonant cavities brings further advantages. By matching the cavity length to half an RF wavelength multiple RF waves can be superimposed allowing higher fields to be reached by low power RF sources. How efficient the cavity is at

storing energy is defined by the Q-factor which is defined in equation 1.12 [12].

$$Q = \frac{\omega U}{P}. \quad (1.12)$$

where  $\omega$  is the angular frequency,  $U$  is the energy stored in the cavity and  $P$  is the power dissipated in the cavity walls.

The maximum achievable acceleration is no longer limited by dielectric breakdown but by the length of the accelerator and the ability to maintain the synchronisation of the field switching, with the particle crossing as it is accelerated. As a particle is accelerated its velocity increases and the time taken to reach the next electrode decreases. As a result, in order to keep the particle and RF in phase either the distance between electrodes or the frequency of the RF needs to be changed.

### 1.2.2.1 Phase Stability

In linear accelerators the phase stability is maintained by a combination of cavity spacing [13] and using different frequencies. Depending on the size of the accelerator it will be separated into several sections each running at a different frequency. For a high energy linear accelerator there are typically three sections, low beta, medium beta and high beta, where beta is the relativistic beta referring to the ratio of the particle velocity to the speed of light. The frequency of each section is different in order to compensate for the increasing particle velocity. This goes some way to maintaining the phase, but as the frequency is constant across a section consisting of many RF cavities further measures must be taken. Within each section the gap between accelerating gaps is varied, increasing with particle velocity to maintain the phase stability.

In circular accelerators the cavity is reused on each revolution. The path length taken by the particle before returning to the cavity is now determined by the magnetic field and so the conditions needed for phase stability are different depending on the type of accelerator used. In isochronous cyclotrons the revolution time is independent of energy and so the phase is stable [14]. In synchrocyotrons and synchrotrons the RF frequency is varied to match the revolution frequency as the beam is accelerated.

### 1.2.2.2 Transit Time Factor

The electric field in RF accelerators is not constant and so the time it takes for the particles to traverse the accelerating gap is now important, as the field will change during this time [15]. From equation 1.13 and the transit time of the particle over the accelerating gap the energy gained by said particle will be

## 1. BEAM DYNAMICS IN CYCLOTRONS AND SYNCHROTRONS

$$\Delta E = qV_0T \cos \phi. \quad (1.13)$$

where  $q$  is the particle charge and  $T$  is the transit time factor. The transit time factor is an integration of the RF phase over the particle transit time and has a maximum value of 1 when the accelerating gap is infinitely small.

### 1.3 Cyclotrons

#### 1.3.1 The Classical Cyclotron

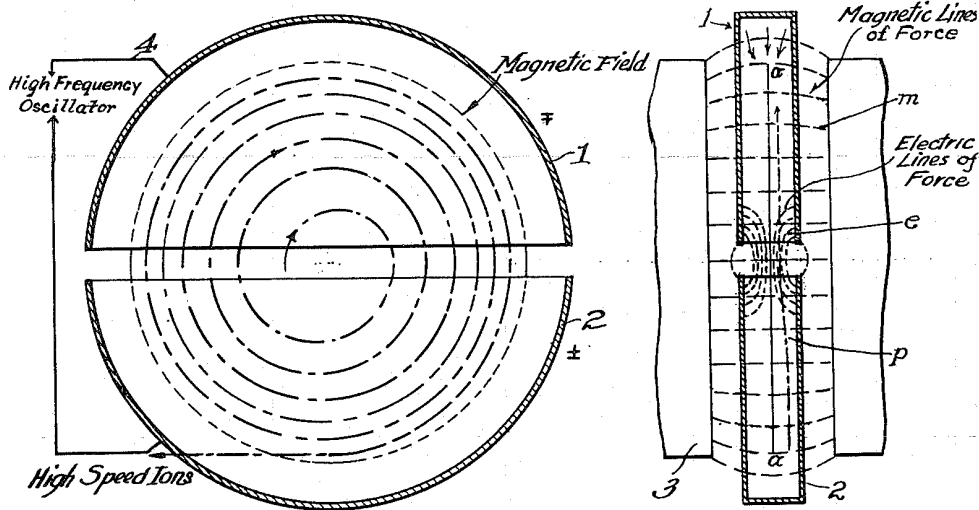


**Figure 1.2:** The basic concept of a cyclotron as described by Lawrence in his original patent from 1934 [16].

In 1929 Lawrence proposed using two semi-circular hollow plates with an RF voltage across them, placed in a uniform magnetic field as a method for accelerating light ions [14]. This method would later be dubbed the cyclotron, the basic concept for which is shown in fig 1.2 [16]. What Lawrence realised was that particles in a uniform magnetic field have a constant revolution frequency, now known as the cyclotron frequency, that is independent of both radius and velocity given by

$$\omega_{cyc} = \frac{eB_0}{m}, \quad (1.14)$$

where  $B_0$  is the magnetic field strength,  $e$  is the ion charge and  $m$  is the particle mass.

Using equation 1.14 the magnetic field can be set such that the cyclotron frequency matches the RF frequency applied across the dee electrodes and hence particles can be accelerated each time they traverse the gap between the electrodes. The ability to reuse the same accelerating cavity as the beam gains energy drastically reduced the size of the cyclotron compared to the linear accelerators that came before.

### 1.3.2 The Isochronous Cyclotron

Lawrence's observation about the revolution frequency only holds true for non-relativistic particles. As the particle is accelerated and relativistic effects become important the mass  $m$  in equation 1.14 increases and must be modified to  $\gamma m_0$ . To keep the cyclotron frequency constant at higher energies the magnetic field must be increased to counter the increasing mass [17]. The magnetic field must therefore be scaled radially by

$$B(r) = \gamma(r)B_0, \quad (1.15)$$

where  $B(r)$  is the magnetic field at any given radius,  $\gamma(r)$  is the Lorentz factor of the beam at that radius and  $B_0$  is the magnetic field when the particle is not relativistic i.e. when  $\gamma = 1$ .

Focusing in classical cyclotrons comes from the field index  $n$ , defined in equation 1.16, which is a characterisation of the radial field variation given by:

$$n = \frac{R}{B(r)} \frac{dB(r)}{dR}. \quad (1.16)$$

where  $R$  is the radius,  $B(r)$  is the magnetic field at that radius and  $dB(r)/dR$  is the rate of change of the magnetic field with radius. For an isochronous cyclotron where the field increases with radius the field index is  $n = \gamma^2 - 1$ .

The betatron frequencies in a classical cyclotron are related to the field index and given by

$$\nu_r = \sqrt{1 + n}, \quad (1.17)$$

$$\nu_z = \sqrt{-n}, \quad (1.18)$$

where  $\nu_r$  and  $\nu_z$  are the radial and vertical tunes. From this it can be seen that for an isochronous cyclotron the radial tune is positive and therefore focused, but the vertical tune is imaginary i.e. defocusing. At non-relativistic energies stability can be achieved

## 1. BEAM DYNAMICS IN CYCLOTRONS AND SYNCHROTRONS

---

if

$$-1 < n > 0, \quad (1.19)$$

ie. if the field is gently decreasing with  $r$ . This produces both positive  $\nu_r$  and positive  $\nu_z$  but isochronicity is lost at higher energies.

### 1.3.3 AVF Cyclotrons

The problem of focusing in isochronous cyclotrons limits the achievable energy. This is either by a lack of phase stability at higher energies when using a gently decreasing field, or a lack of vertical focusing when following the isochronous condition resulting in poor beam transmission. The azimuthal varying field (AVF) cyclotron has magnetic fields that follow the isochronous condition given in equation 1.15. To counter the resulting instability in the vertical plane an additional focusing term is needed. This is achieved by varying the field in the azimuthal direction by creating valley sections where the field is reduced relative to the main hill sections [18]. As the field varies it becomes non-perpendicular to the particle trajectory. This in turn causes field components in the X and Y planes that have an affect on the vertical motion. This focusing term is known as the flutter and is defined as

$$F = \frac{\bar{B}_z^2 - \bar{B}_z'^2}{\bar{B}_z^2}. \quad (1.20)$$

This in turn affects the betatron frequencies, adding an additional term to the tune equations [19];

$$\nu_r^2 = 1 + n + \frac{3N^2}{(N^2 - 1)(N^2 - 4)} F(1 + 2 \tan^2 \delta), \quad (1.21)$$

$$\nu_z^2 = -n + \frac{N^2}{N^2 - 1} F(1 + 2 \tan^2 \delta), \quad (1.22)$$

where  $N$  is the number of sectors and  $F$  is the flutter. The  $\delta$  term is the spiral angle and is discussed in section 1.3.4. As well as being able to maintain isochronicity and vertical focusing simultaneously, AVF cyclotrons allow the designer more freedom as both the hill/valley angle and the hill/valley magnetic field ratio can be varied.

From equation 1.20 it can be seen that increasing the difference between the hill and valley sections will increase the flutter. By creating entirely separate magnet sections the valley field can be taken to 0, maximizing the flutter and therefore the betatron

tunes. This type of AVF cyclotron is known as the Separate Sector Cyclotron (SSC). The lower magnetic field in the valley sectors means that the machine is less compact than an AVF cyclotron. This extra space can however aid with both injection and extraction.

### 1.3.4 Spiral Sector Cyclotrons

In the betatron tune equations given in 1.21 and 1.22,  $\delta$  is the spiral angle, which is the angle between the radius to the centre of the magnet and the magnet centroid as shown in fig 1.3 [20].

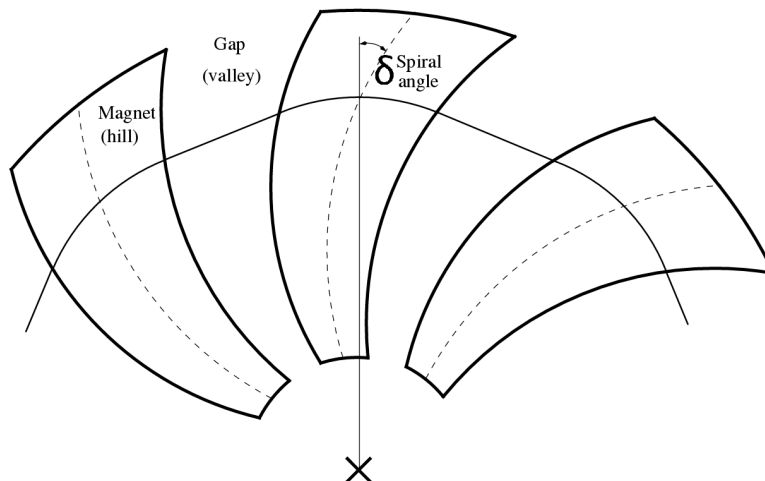


**Figure 1.3:** Diagram of the spiral sector concept taken from [20]. The angle between the magnet centre and the radius is the spiral angle  $\delta$ .

This term, which is 0 in radial sector cyclotrons, is the result of the edge crossing angle. The spiral makes the crossing angle more acute at the entrance (increasing the focusing) and more obtuse at the exit (decreasing the focusing). This creates an alternating focusing/defocusing structure which has a net focusing effect. This technically makes spiral sector cyclotrons a type of FFAG. The most powerful accelerators in the world are spiral sector cyclotrons with the ring cyclotron at PSI holding the record for beam power [21]. By applying AVF and spiral sectors they have the strongest focusing achievable in a cyclotron and their isochronicity allows for CW operation. Thus they are able to accelerate high average beam currents to relatively high energies. For high instantaneous beam power synchrotrons are still preferred as they can reach much

## 1. BEAM DYNAMICS IN CYCLOTRONS AND SYNCHROTRONS

---

higher energies.

The energy reach of all types of isochronous cyclotron is limited by relativistic effects. As the beam becomes increasingly relativistic the field gradient grows to such a level that the magnets become difficult to design and manufacture.

### 1.3.5 Synchrocyclotrons

Another method of accounting for relativistic effects is the synchrocyclotron. In a synchrocyclotron the conditions in equation 1.19 of a gently decreasing field are maintained to provide focusing. In order to keep the particles and the RF synchronised the RF frequency applied to the dees is varied during acceleration such that it matches with the particle revolution frequency [22]. With the RF synchronised to the beam frequency there should not be any phase slip during acceleration. As a result much lower accelerating voltages can be used. Since there is no azimuthal variation of the magnetic field, synchrocyclotrons can be made very compact. The most significant disadvantage of synchrocyclotrons is that the frequency modulation means that only during a small portion of the RF cycle can particles be injected and maintain phase stability. This results in much lower beam currents than can be achieved with isochronous cyclotrons. Additionally the RF system and power supplies are more complicated.

Modern synchrocyclotrons are most commonly used in proton therapy machines. For this application high beam currents are not usually required and the synchrocyclotron's ability to reach high energies in a compact machine is highly desirable. By making the magnet superconducting Mevion have produced a proton therapy solution where the synchrocyclotron is mounted on the gantry [23]. The superconducting magnets are both lighter and can produce higher magnetic fields making it light and compact enough to be mounted on the gantry. This makes the whole system simpler and more compact, with no need for transfer lines and the ability to fit it into a single room.

### 1.3.6 Injection

Injecting the beam is a critical stage in the acceleration process. For high current running it is important to have a high capture efficiency, i.e. to inject as many particles from the ion source onto a stable phase and trajectory as possible. In a cyclotron the beam can be injected axially from above or below, or radially from the side.

### 1.3.6.1 Axial Injection

In early cyclotrons the ions were generated in the central region of the machine using a filament to ionise the residual gas[24]. This produced poor quality beams as there was little control over the ion distribution. Internal ion sources improved beam quality but still had draw backs. The beam was injected directly from the ion source into the accelerating gap between the dees. The capture efficiency of this technique was low as the ions initial momentum is perpendicular to the accelerating direction. Consequently control of the vertical particle distribution as the beam is injected was limited, resulting in many of the ions moving away from the mid-plane of the accelerator and ultimately being lost on the beam pipe aperture. Efforts were made to find a way to inject the beam onto the mid-plane of the accelerator, with its momentum in the same direction as the accelerating gradient. Additionally by moving the ion source outside the cyclotron magnet additional elements could be introduced to shape the beam such as einzel lenses and RF bunchers.

In 1965 W.B. Powell and B.L. Reece invented a technique for bending the beam through  $90^\circ$  and on to the median plane with electrostatic deflectors[25]. An electrostatic field is created between a pair of electrodes consisting of a high voltage plate and a wire grid orientated at  $45^\circ$  to both the mid-plane and the axial plane as shown in fig 1.4 [26]. This is known as a mirror inflector as the angle of incidence and reflection are the same ( $45^\circ$ ) and the vertical profile of the bunch is flipped, just as with an optical mirror. Disadvantages of this design are that high electrode voltages are required to bend the particles and the wire grid electrode is susceptible to damage and degradation from the beam [27].

The mirror inflector requires such high voltages as the electric field is not perpendicular to the particle velocity, other than at a single point half way through the bend. Consequently the electric field is not only acting to bend the beam, but decelerates it as it enters the inflector and accelerates it as it exits. By shaping the electrodes to follow the particle trajectory and thus keeping the field perpendicular, the beam will follow an equipotential surface and the voltages can be reduced. As the beam is bent the component of its velocity perpendicular to the cyclotrons magnetic field increases. As a result the particle trajectories begin to be bent in the radial plane, further complicating the inflector design. The spiral inflector invented by Belmont and Pabot compensated for this by twisting as it bends the particles, thus keeping the beam on an equipotential surface [28]. As the the spiral inflector maximises the bending from the electric field and utilises the magnetic field to begin radial circular motion the injection set up can

## 1. BEAM DYNAMICS IN CYCLOTRONS AND SYNCHROTRONS

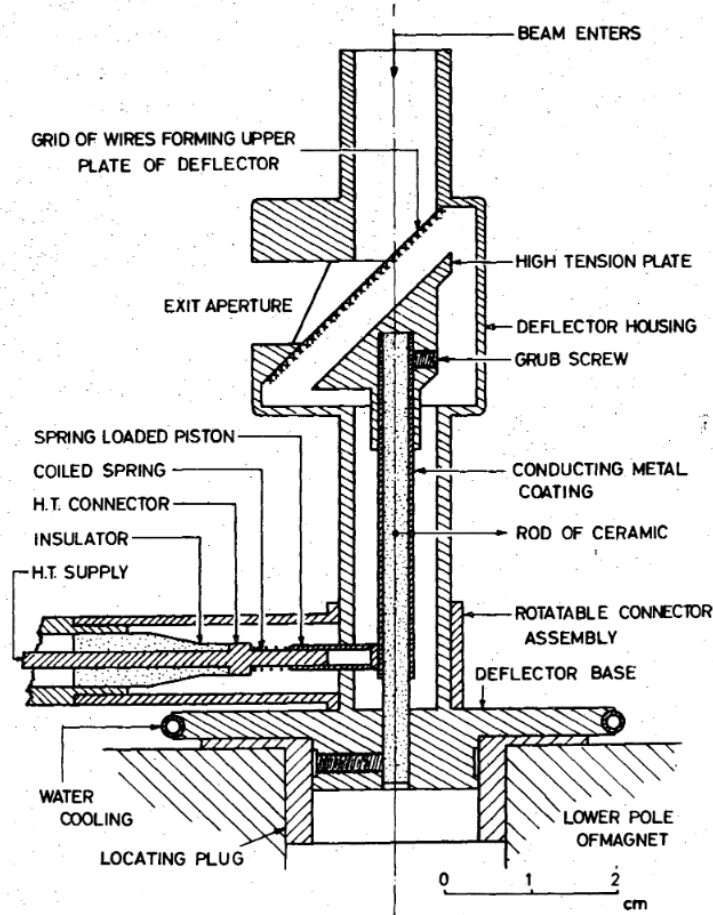


**Figure 1.4:** Schematic of a magnetic mirror inflector taken from [26]. The beam is reflected  $90^\circ$  by the magnetic field between the high voltage electrode and the grid.

be made quite compact. The electric bending radius and the tilt parameter  $k$ , which defines how quickly the electrodes twist, can be varied allowing for some design freedom [29]. One downside of a spiral inflector is that the complicated geometry makes it relatively difficult to manufacture.

The hyperbolic inflector first proposed by Muller also bends the beam on a equipotential surface but unlike the spiral inflector maintains rotational symmetry [30]. In this case whilst the field remains perpendicular to the particle velocity, it does not remain perpendicular to the injection axis resulting in less vertical bend as the particle approaches the median plane. Consequently this design is less compact than other types of inflector. Its advantages are in its simplicity of design, manufacture and in

calculating beam optics which can be done analytically [31].

### 1.3.6.2 Radial Injection

By injecting radially along the median plane the use of an inflector can be avoided. However the effects of the magnetic fields are significantly more problematic. For large separate sector cyclotrons where the magnetic field is zero or close to zero in the valley sectors, radial injection is relatively simple. The beam can be injected down a valley sector without needing to compensate for magnetic fields, then bent magnetically or electrostatically on to the accelerated orbit. For non-separate sector designs, or very compact separate sector designs, a method of coping with the non zero magnetic field must be found.

One early proposal for countering the magnetic field was to use electrodes placed along the injection path to oppose any deviation from the desired trajectory [32]. This method is very difficult to make work properly and only a 4% transmission at injection was achieved. Another technique is trochoidal injection which uses the magnetic field to spiral the beam path along the magnet edge and to the centre of the machine [33]. This only works for low energy gain machines i.e. the ratio of extraction energy to injection energy is small. If this ratio is too big then the magnetic field will bend the injection beam too tightly causing the spirals to overlap. Due to their problems neither of these techniques are regularly used anymore.

The main method used today for radial injection into compact cyclotrons is charge exchange injection. Often used for median to heavy ions the beam enters the cyclotron not fully stripped. The lower charge means that the beam is bent more gently and by controlling the charge and the energy of the beam it can be directed towards the first equilibrium orbit. A stripping foil is placed at the equilibrium orbit which removes the remaining electrons from the particles. The beam is now bent more tightly on to the desired orbit. This technique has been successfully used at the Chalk River Superconducting Cyclotron for injecting both carbon and uranium ions. A schematic of the injection system used is shown in fig 1.5 [34].

### 1.3.6.3 Beam Bunching

The RF cycle is only in the accelerating phase 50% of the time so the maximum phase acceptance in a idealised machine is  $180^\circ$ . Real machines are never perfectly isochronous and so they have a phase slip during acceleration that further reduces the acceptance. Additionally to reduce growth in the energy spread of the beam only a fraction of that

## 1. BEAM DYNAMICS IN CYCLOTRONS AND SYNCHROTRONS

---

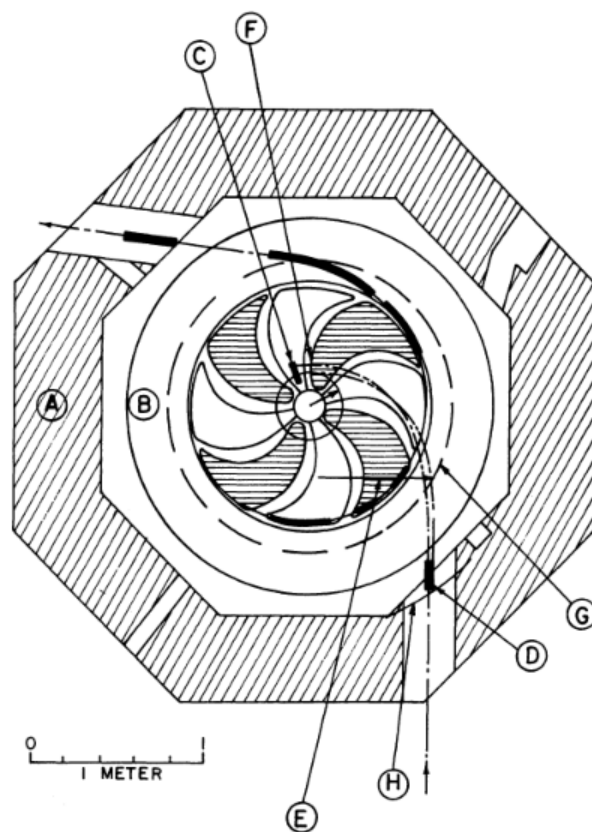


**Figure 1.5:** Diagram of a charge exchange injection system, taken from [34]. A -Yoke, B -Cryostat, C -Carbon stripping foil, D -Steering magnet, E -Injection radius, F -Inner equilibrium radius, G -Effective field boundary, H -Matching radius.

acceptance would ideally be used. As a result the capture efficiency of a continuous beam injected into the cyclotron would be at best 50% and realistically closer to 10%.

In order to run at high current a way must be found increase the beam capture efficiency. RF bunchers can be used to modulate the particle velocities in such a way that over a given length the beam converges into bunches [35]. As the beam enters the RF buncher the particle velocities are modulated by the electric field. As the field is time varying, parts of the beam will be accelerated and others decelerated. These two parts of the beam converge over time on a central point (the part of the beam that saw zero electric field).

The ideal waveform for a buncher is a sawtooth wave. The linear field change, and therefore linear velocity distribution, means that all particles will have the same longitudinal focal length. As such all particles should converge at the same point.

Unfortunately sawtooth waves are difficult to generate and apply efficiently so more commonly a sine wave is used. As a sine wave has a non-linear gradient other than at small displacements from the longitudinal centre, different parts of the beam will have different longitudinal focal lengths. Consequently the capture efficiency is lower than if a sawtooth was used providing, a bunching efficiency of up to 50% depending on the phase acceptance of the machine as shown in fig 1.6 [36].

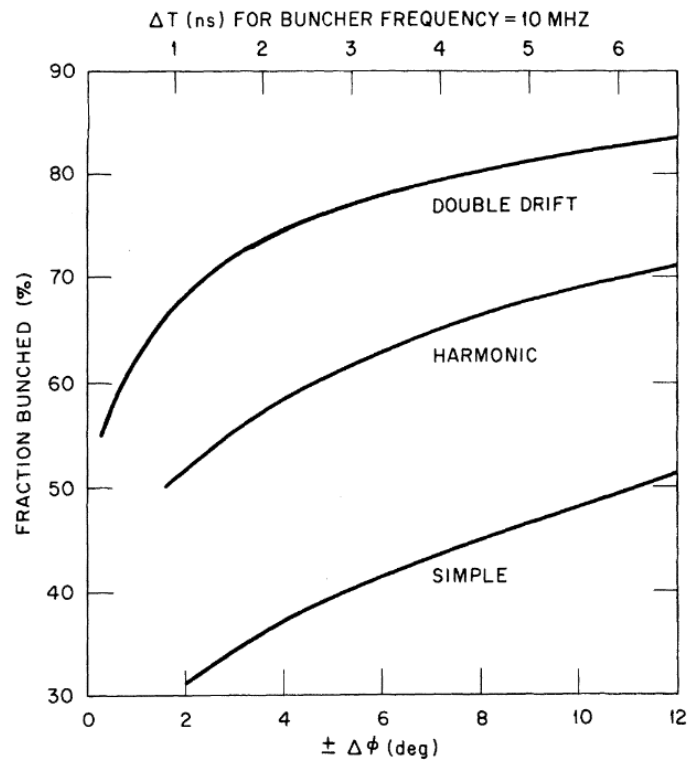


**Figure 1.6:** Bunching efficiency of different types of buncher. The maximum bunching efficiency is achieved with the double drift buncher. Taken from [36]

To create an effect closer to that of a sawtooth, and therefore increase the bunching efficiency, multiple harmonics can be combined to form a more complicated waveform. Known as a harmonic buncher this will create a larger linear, or close to linear region in the waveform. More of the beam will have a common focal length and therefore the bunching efficiency will be increased.

Another way of enhancing the bunching effect is to use a double drift buncher. In this setup two cavities are used. The first cavity operates at the fundamental bunching frequency and the second cavity at the second harmonic. As the beam has been partially

## 1. BEAM DYNAMICS IN CYCLOTRONS AND SYNCHROTRONS

---

bunched when it reaches the second cavity, more of the beam is in the region with the ideal gradient, improving its bunching efficiency [36]. As well as being more efficient the double drift buncher also has the benefit that as the two cavities operate separately they are more easily adjusted and optimised than a harmonic buncher.

### 1.3.7 Extraction

Clean extraction from cyclotrons can be difficult as the magnetic field naturally acts to trap charged particles within the machine.

#### 1.3.7.1 Internal Target

A simple solution to the problem of extraction is to not to extract the beam at all. Instead the target can be placed within the cyclotron on the orbit of the desired energy [37]. One advantage of this setup is that there are no losses from extraction. Additionally the last orbit does not have to be separated for extraction, so the orbit separation can be relaxed and a lower accelerating voltage used. If the cyclotron is self shielded the target will be within that shielding, negating the need for additional target shielding. Its disadvantages are that there is restricted space in which to place the target making setting up the optimal target geometry more difficult. Additionally there is less control over the beam that hits the target. With an extracted beam the transfer line can be used to shape the beam as desired. With an internal target the beam properties are entirely controlled by the dynamics of the cyclotron itself.

#### 1.3.7.2 Charge Exchange

If the magnetic field of a cyclotron naturally traps a charged particle inside the machine then a particle of opposite charge, in the same field and on the same initial trajectory, will be naturally ejected from the machine. Therefore if the charge state of the beam can be changed when it reaches the final orbit then it can be extracted. This is known as charge exchange extraction.

Charge exchange extraction is only used with negative ions, as it is easier to strip electrons off than to add them on. A stripping foil usually made of carbon is placed at the final orbit and as the beam passes through it the electrons are removed and the beam bent out of the machine. As there is no septum a large orbit separation is not necessary allowing for lower accelerating voltages to be used. The stripping efficiency is up to 100% and so 100% extraction efficiency is possible. The foil can be easily moved to different radii and azimuthal positions. As such it can be placed at the radii of

different energies and positioned such that the beam at any one of these energies will all converge on a single point allowing for relatively simple variable energy extraction as shown in fig 1.7 [38]. With clever placement of the foils, two or more energies can be simultaneously extracted from the same beam. By placing the foil to intercept just the top or bottom half of the beam at a lower energy, half the beam can be extracted while half continues to be accelerated. A separate foil can then be placed at higher energy to extract the rest of the beam. This technique has been successfully implemented on the TRIUMF 500 MeV cyclotron to extract two different energy beams to separate beam lines [39].

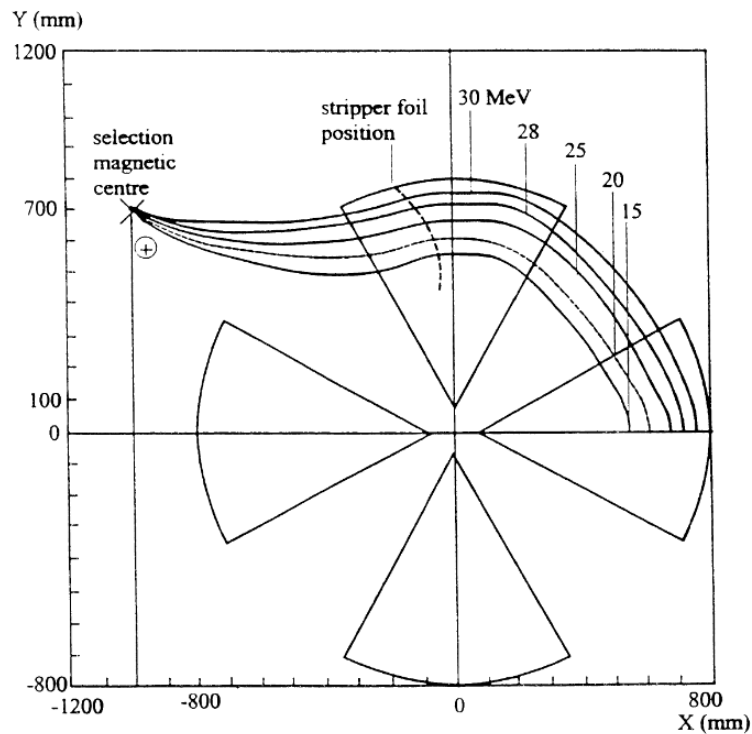


**Figure 1.7:** Charge exchange extraction diagram taken from [38]. By adjusting the position of the extraction foil different energies can be made to extract and converge on a single point.

Charge exchange extraction limits the maximum magnetic field and the accelerating gradient that can be used. Only negative ions can be used and their extra electrons are only loosely bound to the atom. High magnetic or electric fields can strip them off. If this happens before the extraction point beam losses will be incurred. This is more problematic for heavier ions as their extra electrons will be less tightly bound.

## 1. BEAM DYNAMICS IN CYCLOTRONS AND SYNCHROTRONS

---

Consequently charge exchange extraction is generally restricted to use with  $H^-$  ions.

### 1.3.7.3 Electrostatic Extraction

Since charge exchange cannot be used with positive ions another method must be used to pull the beam out of the magnetic field. An electric field applied radially can counter the magnetic field and bend the beam out. The main difficulty with this is making sure that the field is only applied over the final orbit and does not effect the beam during acceleration. To achieve this an electrostatic deflector and septum is used [40]. A high voltage electrode creates the electric field that extracts the beam. The septum is grounded and stops the electric field from permeating further into the machine. If the machine is a separate sector design with large gaps between the magnets then the deflector may be sufficient to extract the beam by itself. In more compact designs however, a channel cut through the magnet may be required to reduce the magnetic field along the extraction path.

The main disadvantage of this set up is that good orbit separation is required otherwise losses on the septum can become problematic. The ability to cool the septum is often a limiting factor on the beam current as losses on the septum generally increase with beam intensity. Activation of the septum can also be problematic especially at higher energies.

## 1.4 Synchrotrons

In terms of the energy frontier, the synchrotron has many advantages that have led to it being the accelerator of choice for high energies. In a synchrotron the magnetic fields are matched (or synchronised) to beam energy, increasing in strength as the beam is accelerated. In this way the beam follows the same orbit at all energies. All the focusing terms are also synchronised to the beam energy meaning that the beam dynamics are identical across the entire energy range. The disadvantage of this approach is that there can only be bunches of the same energy in the machine, reducing the duty cycle and limiting the current achievable. The excellent control over the beam dynamics allows for very long beam survival times, perfect for a storage ring and for reaching high energies without needing extreme accelerating gradients [41].

The stability of synchrotrons is due to the strong focusing effect created with alternating gradient structures. Although a feature of spiral sector cyclotrons, alternating gradient focusing is more powerful in synchrotrons. Part of how the beam dynamics are so well controlled in synchrotrons is that they usually use separate function magnets.

In a cyclotron the magnets are combined function providing both bending and focusing at the same time. In synchrotrons these functions have separate dedicated magnets allowing for simpler magnet design and a greater control freedom.

Dipole magnets are responsible for the beam bending. Their fields are usually uniform making them simple to design and manufacture. In order to keep the bending radius constant at all energies the field must be scaled. From equation 1.3 it can be shown that the magnetic field must scale as

$$B = B_0 \frac{p_1}{p_0}, \quad (1.23)$$

where  $B_0$  is the magnetic field strength for the injection energy,  $p_0$  is the injection momentum and  $p_1$  is the momentum at a given time during the acceleration cycle.

Quadrupoles are used to provide beam focusing. Consisting of four magnetic poles surrounding the beam pipe the field that they create is zero at the centre increasing linearly with radius. Whilst quadrupoles have a focusing (F) effect in one plane (ie. Horizontal), they will simultaneously have a defocusing (D) effect in the orthogonal plane (ie. Vertical). A net focusing effect can be realised by using a combination of F and D quadrupoles arranged in an alternating structure. The type of alternating gradient focusing structure is known as strong focusing. By having separate focusing magnets both the strength and position of the focusing elements are more easily optimised compared with a combined function magnet.

Higher order multipoles can be used to correct for non-linearities in the lattice such as chromaticity which is corrected with a sextupole. The fields in multipoles vary with radius at increasing powers. In sextupoles the field varies with  $r^2$ , octupoles with  $r^3$  etc.

### 1.4.1 Lattice Structures

There are many different focusing structures used in synchrotrons. The most common is the FODO lattice structure consisting of a horizontally Focusing quadrupole (F), a Drift (O), a Defocusing quadrupole (D) and another drift (O). This results in an overall focusing effect in both planes, with the horizontal beta function peaking in the F quadrupole and at its lowest in the D quadrupole. The beta function in the vertical plane is the opposite with a minimum in the F and maximum in the D quadrupole. The overall FODO focusing scheme is show in fig 1.8 [42].

Whilst this type of structure is effective at creating a stable beam there are situations that require particular conditions that the standard FODO lattice cannot provide.

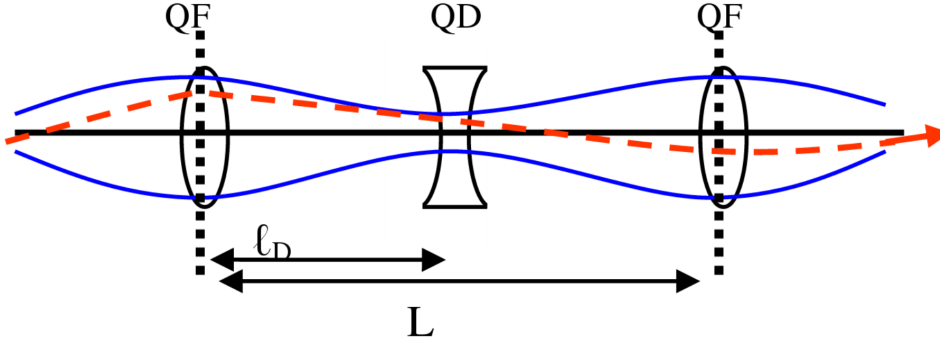


**Figure 1.8:** Diagram of a FODO cell. Blue line is the beam envelope, red line is the path of an individual particle as it traverses the lattice. Taken from [42]

In particle colliders for example, at the collision point the beta functions in both planes needs to be as small as possible to maximise the collision probabilities. In FODO lattices the beta function in one plane is the opposite of the other i.e. when maximum in horizontal it is minimised in the vertical and visa versa. To create a region of simultaneously minimised beta functions the FODO cell must be modified. The position and strength of the second quadrupole is adjusted such that the combined focal point of the quadrupoles is the same as the focal point in the vertical plane.

#### 1.4.2 Synchrotron Motion

In an ideal bunch all the particles would have the same energy, but in reality this is not the case. The injected beam will have a spread in momentum and the longitudinal position of the particles in it. During acceleration collective effects such as space charge can increase this spread. This spread in momentum will affect the revolution time of the particles and hence their phase relative to the RF phase. Depending on whether the beam is above or below transition, a particle with a positive  $\Delta P$  will either arrive early or late relative to the synchronous particle. If the machine is operating on the correct side of the RF crest the particle will receive a smaller kick. As a result on the next orbit the particle will have a longer time of flight moving it back towards the synchronous phase. A particle with a negative  $\Delta P$  will experience the opposite effect increasing its momentum and also moving toward the synchronous phase. This has the overall effect of causing the particles to oscillate around the synchronous phase. Known as synchrotron oscillations this creates longitudinal focusing [43].

The rate of these oscillations per turn is called the synchrotron tune. In the region

close to the synchronous phase ( $\phi_s$ ) the RF field varies linearly and so the frequency can be calculated using equation 1.24.

$$\nu_s = \sqrt{\frac{hqV |\eta \cos \phi_s|}{2\pi\beta^2 E}}. \quad (1.24)$$

where  $\nu_s$  is the synchrotron tune,  $h$  is the harmonic number,  $q$  is the charge of the particle,  $V$  is the RF voltage,  $\eta$  is the phase slip factor,  $\phi_s$  is the synchronous phase,  $\beta$  is the relativistic term and  $E$  is the particle energy. Increasing the voltage will increase the frequency of the synchrotron oscillations but will also increase their amplitude. If the oscillations are driven too hard then the phase can slip out of the stable region and the longitudinal focusing is lost.

## 1.5 Summary

The beam dynamics of different types of accelerator govern their different strengths and weaknesses. Cyclotrons have isochronous fields that allow CW operation with a bunch on every orbit. This allows for high average currents to be achieved but the maximum energy is limited by the size, cost and engineering of the magnets required to reach higher energies. Conversely synchrotrons use ramping magnets and variable frequency RF to constrain all energies to the same orbit but can only accelerate a single orbit at a time. This allows for high energies to be reached as the magnet size is kept small and the dynamics consistent. The down side is that synchrotrons have low average current.

This leaves a gap for high power application where both high current and high energies are required. Linacs can provide high power but are very expensive as they require a large number of RF cavities and more space than a circular machine. A technology that could solve this is the FFAG which combines aspects of both cyclotrons and synchrotrons.

## 1. BEAM DYNAMICS IN CYCLOTRONS AND SYNCHROTRONS

## 2

# FFAG Dynamics and Some Notable Examples

## 2.1 FFAG Dynamics

A fixed field alternating gradient (FFAG) accelerator combines the best features of both cyclotrons and synchrotrons, and by relaxing design constraints frees up more parameters for optimisation. They can achieve higher energies than cyclotrons and higher currents than synchrotrons making them perfect for higher power applications. They feature fixed magnetic fields, simplifying operation compared to a synchrotron, as the field no longer needs to be synchronised to the beam energy. The alternating gradient structure provides strong focusing and is achieved in one of three ways; spiral sectors, alternating bend and counter bend magnets, or offset quadrupoles.

First conceptualized in the 1950's, the Fixed Field Alternating Gradient accelerator has enjoyed a resurgence in interest in recent decades. The FFAG was invented independently by Tihiro Ohkawa, Andrei Kolomensky and Keith Symon in Japan, Russia and the USA respectively. Early development was driven by the Midwestern Universities Research Association (MURA) [44]. The main goal of the MURA collaboration was to build a multi GeV accelerator. Although this was never achieved several small FFAG accelerators were built and various larger high energy designs were proposed. The first operational FFAG developed at MURA was a 400 keV radial sector electron FFAG, with a betatron core providing the acceleration [45]. A spiral sector FFAG [46] and a 50 MeV collider [47] were also built. Spiral sector FFAGs are also known as Spiral Sector Cyclotrons and are discussed in more detail in chapter 1. The 50 MeV collider was somewhat unique in that it was capable of operating with two beams of

## 2. FFAG DYNAMICS AND SOME NOTABLE EXAMPLES

---

the same charge traveling in opposite directions in the same magnetic lattice.

### 2.1.1 Scaling FFAG Dynamics

In a scaling FFAG the magnetic field geometry and radial profile are designed in such a way as to ensure that the closed orbits at any energy are photographic enlargements of each other. This means that the beam dynamics will be identical at all energies. Consequently the focusing properties of the lattice are invariant with respect to energy and therefore so are the tunes, making the machine zero chromatic. To achieve this the magnet geometry must be identical at all energies (i.e. edges of all magnets must point towards the centre of the machine) and the radial field profile must follow the scaling law given in equation 2.1.

$$B_z = B_0 \left( \frac{r}{r_0} \right)^n, \quad (2.1)$$

where  $B_0$  is the magnetic field strength at radius  $r_0$  and  $n$  is the field index defined in equation 1.16. If this condition is met then the tunes will be fixed across the energy range. Another consequence of obeying the scaling law is that you cannot simultaneously follow the isochronous condition given in equation 1.15. This results in a non-isochronous machine that needs variable RF acceleration and can therefore only accelerate bunches of similar energies at the same time, limiting the maximum beam current that is achievable. Some of the advantages that this approach can bring are lower costs and simpler operation (from the use of fixed field magnets) and much larger dynamic apertures when compared to synchrotrons. Additionally acceleration can be done much more rapidly than in a synchrotron as the magnets don't need to be ramped. Several scaling FFAGs have been built largely in Japan, including the ERIT 11 MeV storage ring and 150 MeV main ring at the Kyoto University Research Reactor Institute (KURRI).

### 2.1.2 Non-Scaling FFAG Dynamics

Non-scaling FFAG's are based on the same principles as all FFAG's, in having fixed magnetic fields and an alternating gradient focusing structure. The difference is that in non-scaling FFAG's the scaling law of the radial magnetic field profile is dropped in order to free up more design parameters. One advantage of this is that you are now free to tailor the magnetic field profile to suit other purposes, such as making the machine isochronous which is not possible in scaling machines. The main disadvantage is that

with the scaling law broken, the lattice is no longer zero chromatic. With the tunes now varying over the energy range, resonant tune crossings now have to be accounted for. The rapid acceleration utilised in FFAGs helps mitigate this, increasing the resonance crossing rate and restricting the growth of any instabilities.

Now that the magnetic field gradient is no longer restricted to following equation 2.1 the question is how best to formulate it. By making the magnetic field linear the magnet design is simplified and non-linear effects are avoided. The relation of time of flight with energy in linear designs is a parabola [48]. This comes from the difference between the linear magnetic field and the isochronous field described in equation 1.15, where the field scales with  $\gamma$  which is non-linear. By setting the RF frequency to match the bottom of the parabola the overall time of flight variation can be kept small enough to allow fixed frequency acceleration.

Stationary bucket acceleration can be used in linear machines with injection at the bottom of the bucket and extraction at the top. To extend the height of the bucket an alternative regime can be used. If the right frequency and high enough accelerating gradient is used a channel can be opened up between the stationary buckets. This channel loops around the bottom of the lower bucket and over the top of the higher bucket, the phase continuously slipping from one RF cycle into the next as shown in figure 2.1 [49]. As this channel snakes around the buckets, it is known as the serpentine channel. The height of this channel is larger than that of the individual buckets, extending the energy range in the RF phase space. This contrasts with a synchrotron where the particles move around the bucket undergoing synchrotron motion and the changing frequency gradually increases the energy of the bucket.

More recently proposals have been put forward for non-linear non-scaling FFAGs. With another degree of freedom, these machines can be made either more isochronous and/or the tunes can be stabilised [50]. The non-linear fields are often combined with modified edge profiles that don't simply point into the centre, but are shaped to allow both isochronous acceleration and stabilised tunes. These designs have several potential benefits. The greater degree of isochronicity could potentially allow for the use of smaller accelerating gradients, simplifying the RF design and reducing both capital and running costs. Stabilised tunes will make the design more resistant to field/alignment errors and capable of handling greater space charge forces. As such this type of design is well suited to high power applications such as accelerator driven sub-critical reactors (ADSR) [51].

## 2. FFAG DYNAMICS AND SOME NOTABLE EXAMPLES

---

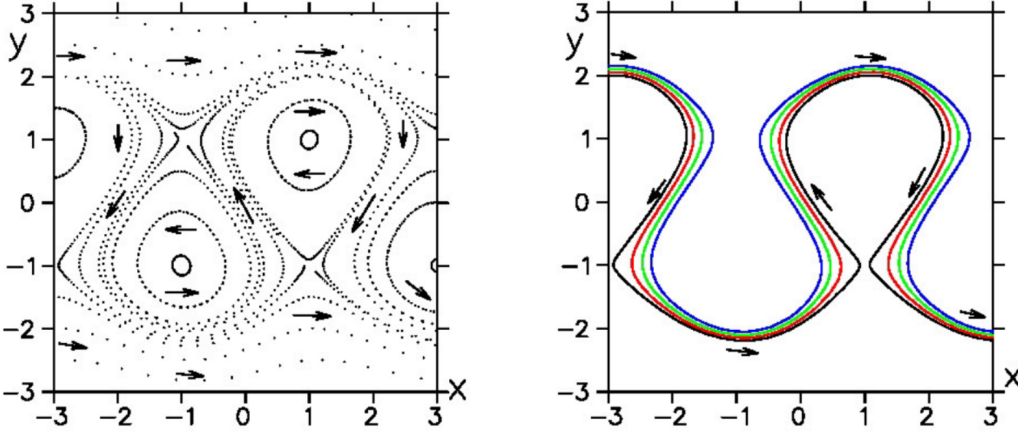


**Figure 2.1:** RF phase space structure with serpentine channel looping around the stationary buckets (right) and highlight of the serpentine channel (left). Taken from [49].

## 2.2 Existing FFAGs

### 2.2.1 POP

The first modern FFAG, which was also the first proton FFAG, was built at the KEK laboratories in Japan. The purpose of this design was to demonstrate that modern computational design and manufacturing techniques are capable of producing the complex magnetic field structures required for this type of accelerator, which held back further development of FFAGs after their initial invention in the 50's.

The proof of principle (POP) machine is a radial sector, scaling, proton FFAG. The energy range is from 50 keV to 500 keV with injection at 0.81 m and extraction at 1.14 m. The lattice is made up of 8 DFD triplet magnets as shown in figure 2.2. The maximum magnetic fields are 0.32 T in the focusing magnet and 0.13 T in the defocusing, whilst the field index is 2.5 [52].

The machine was able to demonstrate the feasibility of designing and manufacturing FFAG magnets, with the field discrepancy found to be less than a few percent and protons were successfully accelerated in an FFAG lattice for the first time [53]. Additionally fast RF sweeps were demonstrated using FINEMET RF cavities [54], which could allow for greater beam intensities compared to a synchrotron. This design was part of a resurgence of interest in FFAGs that led to the design and construction of several other FFAGs discussed below.

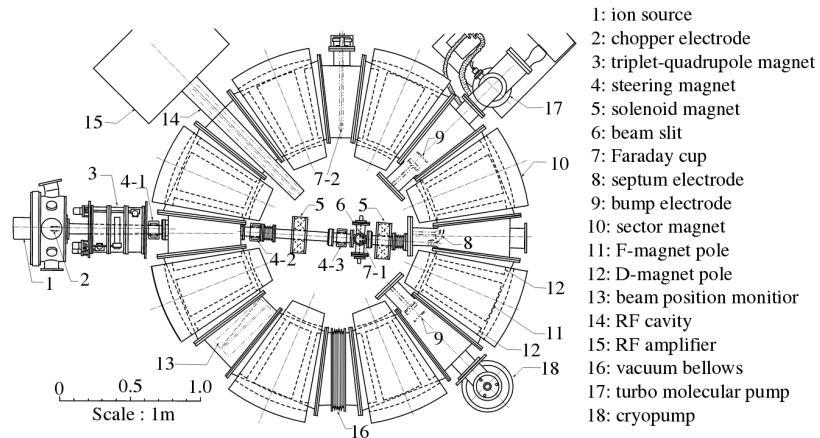


Figure 2.2: POP lattice made up of 8 DFD cells. Taken from [52].

### 2.2.2 KEK/KURRI

A 150 MeV scaling proton FFAG was built at KEK [55] and an almost identical machine at the Kyoto University Research Reactor Institute (KURRI) [56] in Japan. As the machines are very similar only the KURRI machine will be described here.

The KURRI machine is coupled to the Kyoto University Critical Assembly (KUCA) for ADSR experiments. This is the worlds first, and currently only operational ADSR experiment [58]. The energy range of the design is from 11 to 150 MeV with an average radius from 4.47 to 5.2 m. The lattice consists of 12 cells each made of a DFD triplet as shown in figure 2.3 [57]. The radial sector type magnets are constructed with a return-yoke free design where the main focusing magnet has no return yoke, the magnetic flux instead exits through the main coil and then loops back through the reverse bend sections [59]. This design allows the amount of steel and therefore the weight and cost of the magnets to be reduced, as well as allowing injection, extraction and diagnostics devices to be introduced into the main magnet from the outside. As this is a scaling machine the field follows the scaling law in equation 2.1, in this case the value of the field index  $n$  is 7.6. The maximum magnetic fields are 1.63 T in the focusing magnet and 0.78 T in the defocusing magnet. The magnet design has led to some difficulties in operation. The lack of a return yoke has made the design more susceptible to interference from other ferromagnetic materials in the vicinity and the field returning through the defocusing sections makes it difficult to decouple the F and D magnets and adjust for any errors. This has had the effect of creating a closed orbit distortion which has been observed [57].

## 2. FFAG DYNAMICS AND SOME NOTABLE EXAMPLES

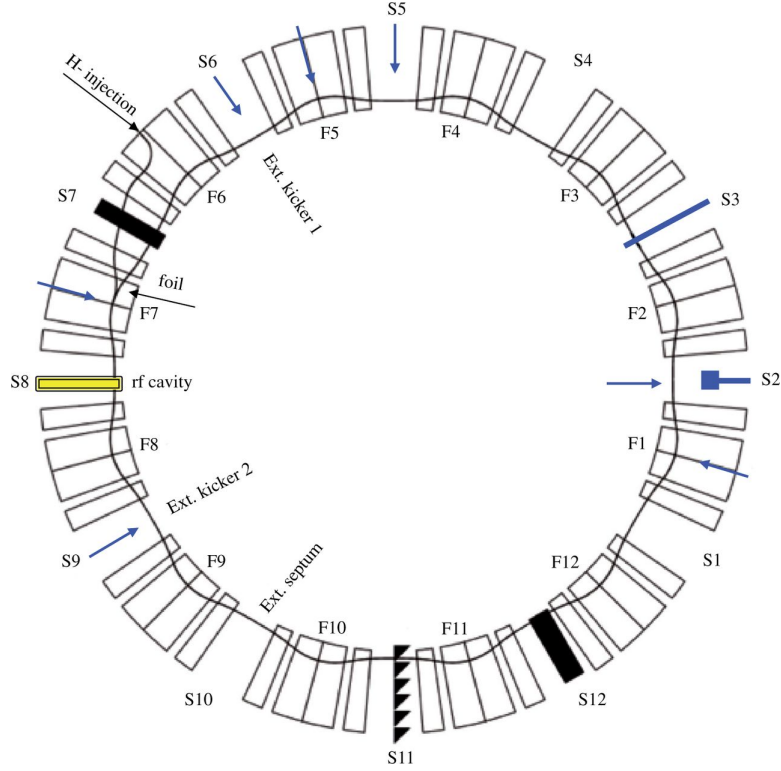


**Figure 2.3:** The KURRI main ring FFAG lattice made up of 12 DFD cells. The  $H^-$  charge exchange scheme and first orbit are shown. Taken from [57].

Injection is by charge exchange with pre-acceleration to 11 MeV from an injection linac. The beam is introduced at  $90^\circ$  to the magnet near the centre of the cell. As the beam is  $H^-$  the counter bends now bend the beam into the injection orbit, where at the centre of the next cell a stripping foil removes the electrons leaving the protons on the correct orbit. The down side of this arrangement is that as the acceleration rate in this machine is quite slow, the beam passes through the foil up to 200 times before it clears it. Each time it passes through the foil it is scattered and so emittance growth and energy straggling are observed [60].

### 2.2.3 ERIT

The emittance-energy recovery internal target (ERIT) is a radial sector, scaling proton FFAG storage ring. The purpose of the design is to demonstrate intense neutron production with an internal target and recycled beam for boron neutron capture therapy BNCT [61].



## 2. FFAG DYNAMICS AND SOME NOTABLE EXAMPLES

---

Injection is via charge exchange from the injection linac which accelerates the beam to 11 MeV [63]. A single RF cavity is used to confine the beam longitudinally and re-accelerate any protons that lose energy through the target. The cavity operates with a peak RF voltage of 200 kV and at the 6th harmonic with a frequency of 18.06 MHz.

ERIT has been able to successfully demonstrate neutron production via a thin internal target. The beam is able to survive for  $>1000$  turns [64] via ionisation cooling through the target, which suppresses the emittance growth from Coulomb scattering [65].

### 2.2.4 EMMA

Only one non-scaling FFAG has been built to date, the electron machine for many applications (EMMA) which is situated at the STFC Daresbury laboratory [66]. It is a proof of principle machine designed to demonstrate the non-scaling principle, serpentine acceleration, resonance crossing and to investigate the dynamics and performance of this type of design.

The injection energy is 10 MeV and extraction is at 20 MeV. The accelerators and lasers in combined experiments (ALICE) accelerator which is situated in the same hall acts as injector with a transfer line linking the two [67]. The lattice is very tightly packed and so a  $70^\circ$  septum magnet is required to bend the beam onto the injection orbit [68].

The lattice consists entirely of quadrupoles in a doublet configuration. Beam bending is achieved by offsetting some of these quadrupoles to create a net bending effect as the beam passes through the non zero field region of the quadrupole, as shown in figure 2.5 [69]. The quadrupoles are all mounted on mechanical sliders that allow their horizontal positions to be adjusted [70]. This allows for the investigation of different lattice configurations and adjustments to correct for field errors. There are 42 cells creating a ring with a 16.57 m circumference. As large accelerating gradients are required to open up the serpentine channel and to safely cross resonances 19 RF cavities are used in the ring, one in every other cell apart from in the injection and extraction regions [71].

EMMA was able to demonstrate a number of technical achievements including: acceleration through a non-scaling FFAG lattice with fixed frequency RF, serpentine acceleration and multiple resonance crossings, including integer resonances.

Both stationary bucket and serpentine acceleration were achieved with fixed frequency RF. With the right initial phase selected a bunch was accelerated from injec-

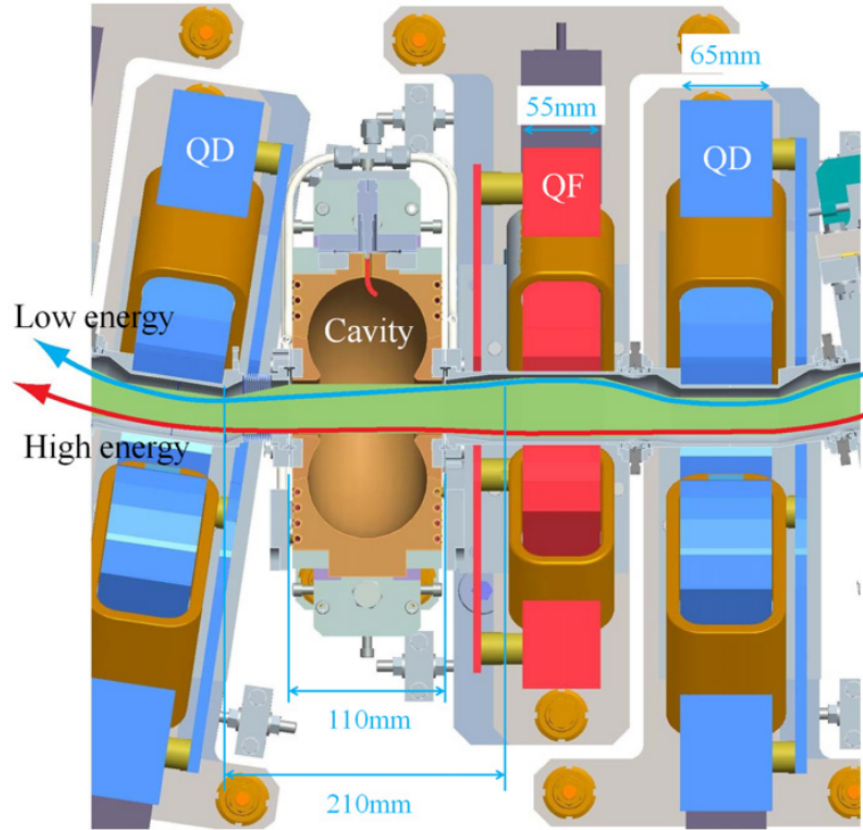


**Figure 2.5:** The EMMA doublet cell and cavity. The offset between quadrupoles creates the bending field. Taken from [69].

tion at 12 MeV to beyond 18 MeV in the serpentine channel [72]. When operating in its normal mode using the serpentine channel and rapid acceleration, extraction energy is reached in 5 - 10 turns. When crossing integer resonances in this configuration no beam growth was observed. If the crossing rate of these resonances was reduced however beam growth was observed [73].

### 2.2.5 Proposed FFAG Designs

There have been many different FFAG designs proposed in recent years as the interest in FFAG technology has increased. Some of these designs will be briefly discussed here with a more detailed description of two of the more mature designs below.

There have been several FFAGs designed for charged particle therapy. Helium ion

## 2. FFAG DYNAMICS AND SOME NOTABLE EXAMPLES

---

accelerator for radiotherapy (HEATHER) is a two stage cyclotron type, non-linear non-scaling FFAG designed to provide 900 MeV  $\text{He}^{2+}$  ions for cancer treatment [74]. Normal-conducting racetrack medical accelerator (NORMA) is a normal conducting version of the PAMELA design which is discussed in more detail below. Its energy range is from 30-350 MeV and it is a scaling, race track, proton FFAG with FDF triplet cells [75]. Work has also been carried out on an FFAG gantry design capable of transporting all energies in the same lattice and delivering them focused to the same treatment point [76]. This type of gantry could improve treatment times as the magnets would not need to be ramped between energies.

Another potential area where FFAGs could be usefully deployed is as a proton driver for an ADSR. As discussed earlier in this chapter KURRI have a 150 MeV proton FFAG coupled to sub-critical reactor. However it can only currently deliver nA's of beam current to the reactor for experiments whereas mA's of beam current and higher energies (ideally  $\approx 1\text{GeV}$ ) are needed to generate sufficient neutrons for a fully operational ADSR. A new ring has been proposed that would sit around the current machine and deliver variable energy from 200 up to 400 MeV to further the ADSR experiments [77]. A 1 GeV non-linear non-scaling FFAG design has been made for ADSR that uses edge shaping optimised with the gradient to create an isochronous machine with stabilised tunes that may be able to provide the intensity needed for a accelerator driven system [78].

FFAG technology is being considered for a possible future neutron spallation source as an upgrade/replacement for the current ISIS machine at the Rutherford Appleton Laboratories (RAL). Two different FFAG designs are being considered. The first is a pumplet model which uses five magnet dFDFd cells [79]. The other option is a DF spiral sector design where the D magnet is used to increase the flutter to create stronger vertical focusing [80].

### 2.2.5.1 PAMELA

PAMELA (particle accelerator for medical applications) is the proposed successor to EMMA developed by the CONFORM (construction of an nsFFAG for oncology, radiation and medicine) [81] collaboration. Its purpose is charged particle therapy, providing protons and carbon ions for treatment [82]. Its energy range is from 60 to 250 MeV for protons and 110 to 450 MeV for carbon ions. Although linear EMMA like lattices were initially considered, creating sufficiently long straight sections proved problematic. It was also found that the designs were overly sensitive to field and alignment errors and

so a different approach was taken.

A non-linear non-scaling design was decided upon as it would allow for the field to be tailored for longer straights as well as stabilise the tunes and make the design less sensitive to errors. The design consists of 12 cells each consisting of an FDF triplet. The magnetic field design is based on a scaling FFAG magnet with the higher order multipoles removed and the magnet edges straightened to form rectangular magnets [83].

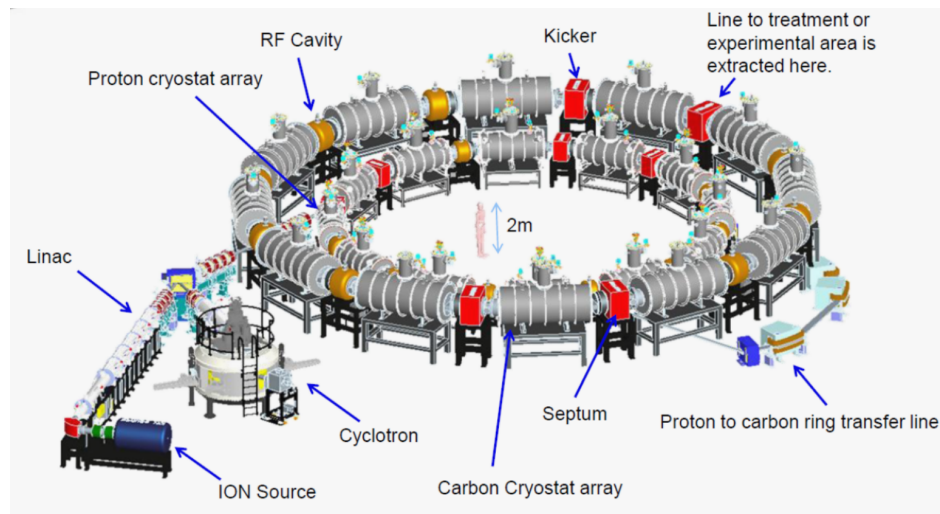


**Figure 2.6:** PAMELA Layout showing the proton ring (inner) and carbon ring (outer). Taken from [84].

With peak magnetic fields of around 4 T it is not possible to use normal conducting magnets. The proposed magnet design is a superconducting double helix design [85]. Separate windings are used for each multipole component so they can be adjusted independently.

Two concentric rings are proposed to facilitate both protons and carbon ions as shown in figure 2.6. Injection for protons would be from a cyclotron whilst a linac and charge exchange injection would be used for carbon ions. Protons would be accelerated in the inner ring whilst carbon ions would first be accelerated in the inner ring then transferred to the outer ring where they would be accelerated to their final energy.

Although the design is well developed there is little likelihood of it being taken forward to construction. This is due to the complexity and cost of the superconducting magnets and prevailing market conditions. The proton therapy market is well catered for by cyclotrons (and a few synchrotrons) whilst the light ion therapy market is very limited, with the clinical benefits of light ions yet to be conclusively proven especially

## 2. FFAG DYNAMICS AND SOME NOTABLE EXAMPLES

given the significant costs.

### 2.2.5.2 e-RHIC and CBETA

e-RHIC is a proposed upgrade to the relativistic heavy ion collider (RHIC) situated at Brookhaven National Laboratory (BNL). RHIC is a heavy ion collider consisting of two synchrotron storage rings operating in opposite directions and is capable of accelerating ions up to and including Uranium to relativistic energies [86]. The upgrade would involve the addition of an electron ring alongside the existing hadron rings allowing electron-ion collisions to investigate quantum chromodynamic (QCD) matter [87]. A non-scaling FFAG lattice with an energy recovery linac (ERL) [88] is being considered for the electron ring. The motivation for using an FFAG design is that as the magnetic fields are fixed, permanent magnets can be used reducing both the capital and operational cost of the machine.

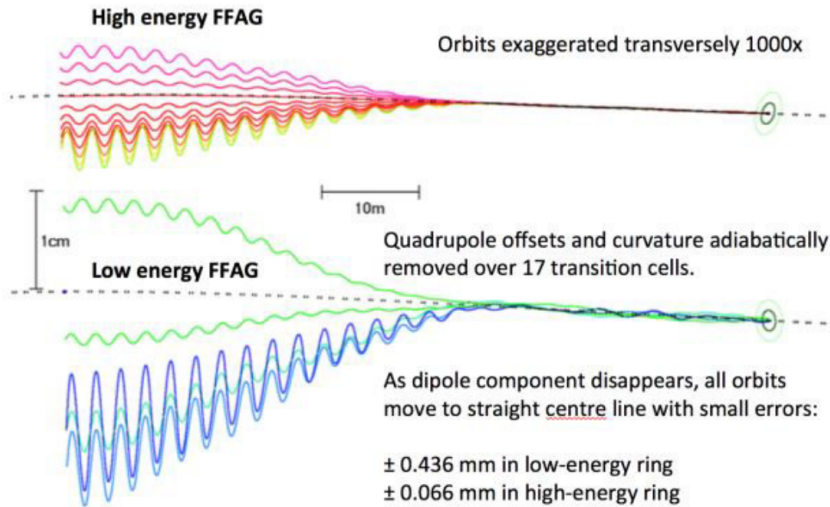


**Figure 2.7:** The matching scheme for eRHIC that adiabatically removes the quadrupole offset bringing the beams onto a single orbit for the straight sections. Taken from [89].

The design is made up of two stacked FFAG rings consisting of six FFAG arcs between straight sections. The first ring would accelerate the electrons from 1.3 to 6.6 GeV and then the second from 7.9 to 21.2 GeV. Both rings would utilise the same ERL section with individual matching sections for each energy either side to ensure that all energies arrive at the correct phase [90]. The lattice in the arcs is made up of identical offset quadrupole doublet cells which are matched into the straight sections by

adiabatically reducing the quadrupole offset and therefore the bending radius to bring all energies onto the same orbit with an error of  $\pm 0.436$  mm in the low energy ring and  $\pm 0.066$  mm in the high energy ring as shown in figure 2.7 [89]

Two different types of quadrupole magnets are being considered, an iron dominated permanent magnet and a Halbach type permanent magnet [91]. In the iron dominated design the permanent magnets are situated around the outside of the pole pieces. The iron poles transfer the magnetic flux into the centre of the magnet and allow control of the field in the central region through the shaping of the pole face [92].

In order to demonstrate the technologies required for eRHIC a smaller lower energy ring called the Cornell-BNL FFAG-ERL test accelerator (CBETA) is being developed in collaboration with Cornell University [93]. This smaller ring will accelerate electrons from 6 MeV to 150 MeV in four passes through a 36 MeV superconducting energy recovery linac, the layout of which is shown in figure 2.8. It will demonstrate all the key technologies needed for eRHIC including; permanent magnet quadrupoles, non-scaling FFAG arcs with offset quadrupole doublet cells, superconducting ERL and individual lines for each energy matching the beam from the FFAG arcs into the ERL. CBETA is well developed with prototype magnets built and tested and preparations for construction well underway.

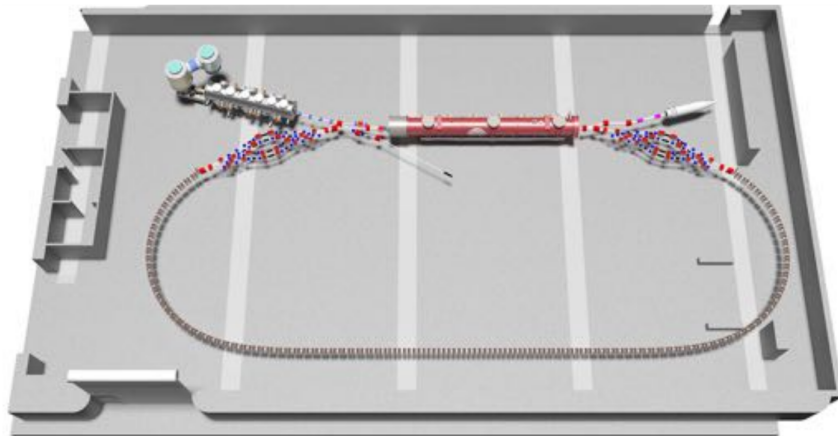


**Figure 2.8:** Floor plan of the CBETA accelerator featuring FFAG arcs, a superconducting ERL and phase matching sections. Taken from [94].

### 2.3 Conclusions

FFAGs have a wide range of potential benefits over current cyclotron and synchrotrons depending on the configuration used. The fixed magnetic fields, fast sweeping RF and zero-chromatic behaviour of scaling FFAGs allow for simpler operation, reduced costs and higher beam intensities compared to synchrotrons. Isochronous non-scaling FFAGs could reach higher energies than cyclotrons, thanks to their strong focusing, whilst maintaining high beam currents. The range of ideas and designs for FFAGs is large, however with relatively few built to date the technology is yet to be fully exploited. If the FFAGs potential is to be realised then designs must be developed for applications where they can provide a significant improvement over current technology. This is most likely in areas that require high beam intensities such as for radioisotope production.

# 3

## Radioisotopes

### 3.1 Radioisotopes

Radioisotopes have a wide variety of applications across many fields including medicine, agriculture and industry. In agriculture they are used for plant nutrition studies, insect pest management, crop improvement through radiation induced mutations and food processing and preservation [95]. In industry radioisotopes are used for measuring flow rates in fluids, resident times, leakage tests and other process investigation techniques [96]. In medicine there are many applications for radioisotopes including sterilisation, imaging and therapy [97].

#### 3.1.1 Medical Applications

There are many uses of radioisotopes in medicine but the main areas of interest are for cancer therapy and imaging.

Radiotherapy is when radiation is used to kill cancer cells. When produced externally by a particle accelerator and delivered as a radiation beam it is known as external beam radiotherapy (EBRT). The use of a sealed radiation source placed next to a tumor, either internally or externally, is known as brachytherapy. The advantage of brachytherapy is that with the source placed close to the treatment area the radiation has a much shorter distance to travel compared to external beam radiotherapy. Consequently less non-tumorous healthy tissue is irradiated and a greater biological effective dose is delivered to the tumor [98]. Several different radioisotopes are used in brachytherapy, mostly gamma and beta emitters, a list of some common examples are shown in table 3.1. Whilst most radioisotopes currently used in brachytherapy are reactor produced some, such  $^{103}\text{Pd}$ , are cyclotron produced.

### 3. RADIOISOTOPES

---

Isotope	Radiation Type	Half-Life	Energy (keV)
<sup>198</sup> Au	$\gamma$	2.7 days	412
<sup>131</sup> Cs	$\gamma$	9.7 days	<34
<sup>137</sup> Cs	$\gamma$	30 years	662
<sup>125</sup> I	X-ray	59 days	27-35
<sup>192</sup> Ir	$\gamma$	74 days	290-608
<sup>32</sup> P	$\beta$	14 days	1710
<sup>103</sup> Pd	X-ray	17 days	20-23

**Table 3.1:** Table of radioisotopes that are commonly used in brachytherapy [98].

Isotope	Radiation Type	Half-Life	Energy (MeV)
<sup>225</sup> Ac	$4\times\alpha, 2\times\beta$	10 days	5.1-8.4
<sup>211</sup> At	$\alpha$	7.2 hours	5.9/7.4
<sup>212</sup> Bi	$\alpha, \beta$	61 minutes	6.1/7.8
<sup>213</sup> Bi	$\alpha, 2\times\beta$	46 minutes	6.0/8.4
<sup>223</sup> Ra	$4\times\alpha, 2\times\beta$	11.4 days	5.7-7.5
<sup>149</sup> Tb	$\alpha$	4.1 hours	4.0
<sup>227</sup> Th	$5\times\alpha, 2\times\beta$	18.7 days	5.7-7.5

**Table 3.2:** Table of potential alpha emitting radioisotopes for brachytherapy. <sup>211</sup>At is of particular interest due to its half-life and its single alpha decay [101].

Brachytherapy is an effective treatment for many different cancer types, but the main criteria for its use are that the tumor is accessible such that the source can be placed in close proximity, and there are radio-sensitive organs in proximity to the tumor making conventional EBRT undesirable. As such some of the cancers it is used to treat include cervical, prostate, breast, skin, mouth and throat cancers [99].

In recent years there has been an increase in interest in the use of alpha emitters for brachytherapy. The potential benefits of alpha emitters are the high linear energy transfer (LET) which results in more efficient killing of tumor cells and the short penetration depth that can help localise the dose to the tumor. A list of potential alpha emitting radionuclides is shown in table 3.2. One of the most promising alpha emitters for this type of therapy is <sup>211</sup>At due to its half life of 7.2 hours and the fact that it is a sole alpha emitter with no other decay products [100].

<sup>211</sup>At is produced through the irradiation of Bismuth with alpha particles in the <sup>209</sup>Bi( $\alpha, 2n$ )<sup>211</sup>At reaction. The cross-section of this reaction shown in figure 3.1 shows that <sup>211</sup>At can be produced at energies from 21-40 MeV. Above 30 MeV alternative products such as <sup>210</sup>At and <sup>210</sup>Po begin to be created in sizable quantities so energies

are generally kept below 30 MeV to maintain purity [101]. There are relatively few cyclotrons currently capable of accelerating alpha particles to 20-30 MeV, so as interest in the use of  $^{211}\text{At}$  for brachytherapy increases there will be a demand for more capacity.

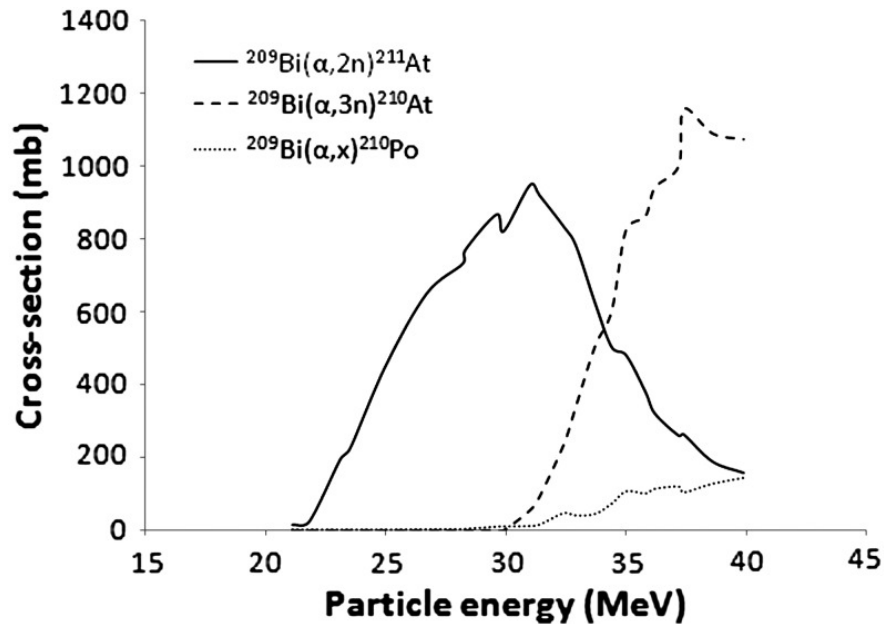


**Figure 3.1:** Cross-sections of competing reaction for alpha particles incident on  $^{209}\text{Bi}$ . Above 30 MeV production of  $^{210}\text{At}$  and  $^{210}\text{Po}$  begin to pollute the  $^{211}\text{At}$  sample. Taken from [101].

For medical imaging, radioisotopes are used in a variety of procedures but the main imaging techniques are positron emission tomography (PET) and single photon emission computed tomography (SPECT).

In PET the radioisotope is incorporated into an organic molecule that can be taken up by an organ in the body. When the radioisotope decays it produces a positron which then annihilates with an electron in the surrounding tissue. This produces a pair of photons which are detected by an array of scintillators. Due to conservation of momentum the photons will radiate in opposite directions from the annihilation site and arrive at the detector coincidentally. Computational tomography is then used to reconstruct the point of origin of the photons and hence build up an image of the organ [102].

SPECT is very similar to PET, the main difference being that in SPECT a single photon is emitted directly from the decay of the radioisotope [103]. This eliminates the error from the distance traveled by the positron in PET ( $<1\text{mm}$ ), but as only a

### 3. RADIOISOTOPES

Isotope	Reaction	Energy (MeV)	Half-Life
$^{99m}\text{Tc}$	$^{100}\text{Mo}(\text{p}, 2\text{n})$	14-30	6 hours
$^{123}\text{I}$	$^{124}\text{Xe}(\text{p}, 2\text{n})^{123}\text{Xe} \rightarrow ^{123}\text{I}$	27	13.1 hours
$^{201}\text{Tl}$	$^{203}\text{Tl}(\text{p}, 3\text{n})^{201}\text{Pb} \rightarrow ^{201}\text{Tl}$	29	73.1 hours
$^{11}\text{C}$	$^{14}\text{N}(\text{p}, \alpha)$	11-19	20.3 minutes
$^{18}\text{F}$	$^{18}\text{O}(\text{p}, \text{n})$	15	110 minutes
$^{64}\text{Cu}$	$^{64}\text{Ni}(\text{p}, \text{n})$	15	12.7 hours
$^{124}\text{I}$	$^{124}\text{Te}(\text{p}, 2\text{n})$	13	4.14 days

**Table 3.3:** Table of common imaging isotopes that can be produce with a particle accelerator. [101]

single photon is detected its point of origin cannot be determined. Instead photons from multiple decays are detected and used to estimate density of isotope in a given area. This results in a lower resolution than PET of around 1 cm.

Many of the commonly used imaging isotopes are produced with a particle accelerator and are listed in table 3.3.  $^{99m}\text{Tc}$ ,  $^{123}\text{I}$  and  $^{201}\text{Tl}$  are used for SPECT scans.  $^{99m}\text{Tc}$  is the most commonly used SPECT isotope and accounts for over 80% of all imaging procedures carried out globally [104].  $^{99m}\text{Tc}$  is produced from a Molybdenum generator.  $^{99}\text{Mo}$  is the mother isotope of  $^{99m}\text{Tc}$  and decays into it via a  $\beta$  decay. The half life of  $^{99}\text{Mo}$  is 2.75 days, much longer than the 6 hours of  $^{99m}\text{Tc}$  and so is ideal for transporting over long distances. Once at its destination the  $^{99}\text{Mo}$  will gradually decay into  $^{99m}\text{Tc}$  which can be extracted and used in procedures. Currently  $^{99}\text{Mo}$  is primarily produced in nuclear reactors, however recently there has been increased interest in alternative production methods. The majority of the world supply of  $^{99}\text{Mo}$  came from just 5 reactors worldwide. In the late 2000's planned maintenance and unexpected shutdowns resulted in only one of these being operational for an extended period of time, which led to a world wide shortage of  $^{99m}\text{Tc}$  and the cancellation of many procedures [105]. One of these reactors, the NRU, has recently been decommissioned and others are reaching the end of their lifetime.  $^{99}\text{Mo}$  is produced through the fission of  $^{235}\text{U}$  and most of the current suppliers use highly enriched uranium targets which bring regulatory and proliferation concerns. These concerns have led to a desire for a more diverse supply chain to be created [106].

One alternative to the reactor production of  $^{99}\text{Mo}$  generators is the direct production of  $^{99m}\text{Tc}$  through the proton bombardment of  $^{100}\text{Mo}$  [107]. As this skips the  $^{99}\text{Mo}$  generator, production would need to be relatively local to the point of use as the 6 hour half-life prohibits long distance distribution. The reaction that is used is  $^{100}\text{Mo}(\text{p},$

$2n)^{99m}\text{Tc}$ , the cross-section for which is shown in figure 3.2. The cross-section peak is at  $\approx 14$  MeV but in thick target production energies of between 20-30 MeV are usually used. This is to allow the beam to degrade through the cross-section peak, because if 14 MeV was used many of the protons would have lost energy and moved away from the peak before reacting. The down side of this is that the higher energies excite other reactions such as  $^{100}\text{Mo}(p, 3n)^{98}\text{Tc}$  and  $^{100}\text{Mo}(p, 2n)^{99g}\text{Tc}$  creating impurities in the final product.

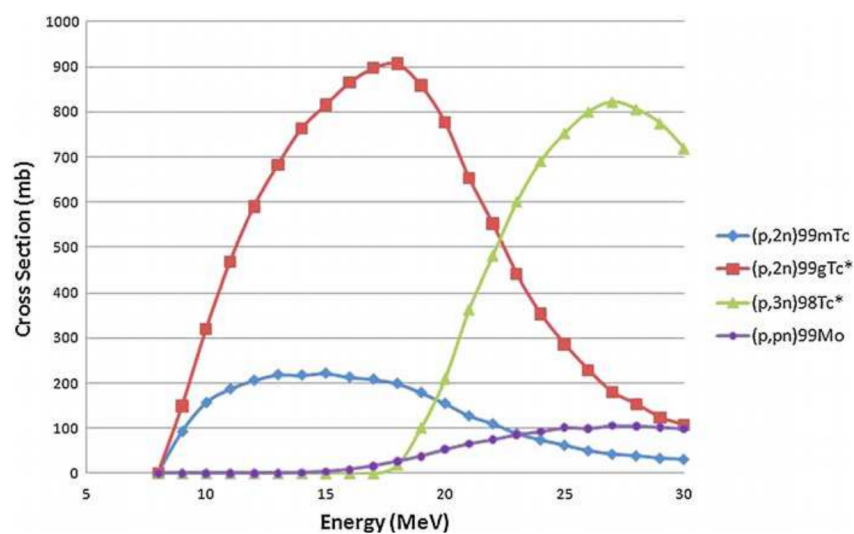


**Figure 3.2:** Cross-sections of competing reactions from the proton irradiation of  $^{100}\text{Mo}$ . Energies of up to 20 MeV are commonly used for  $^{99m}\text{Tc}$  production, however the higher the energy used, the greater the level of impurities. Taken from [108].

Other SPECT isotopes include  $^{123}\text{I}$  and  $^{201}\text{Tl}$ .  $^{123}\text{I}$  is of interest because it is easily incorporated into many different types of molecule. It is produced through the irradiation of  $^{124}\text{Xe}$  with 27 MeV protons to create  $^{123}\text{Xe}$  which then decays into  $^{123}\text{I}$ . Its cost is relatively high compared to other radioisotopes which limits its use.  $^{201}\text{Tl}$  is used in scintigraphy and for measuring blood flow in SPECT. It can be produced by the proton irradiation of  $^{203}\text{Tl}$  to form  $^{201}\text{Pb}$  which decays to  $^{201}\text{Tl}$ .

The most common isotope used in PET is  $^{18}\text{F}$ . It is produced in the  $^{18}\text{O}(p, n)^{18}\text{F}$  reaction and is most commonly used in the form of fludeoxyglucose (FDG). FDG is a sugar and is therefore readily absorbed by organs of the body. Tumor cells have a higher than normal uptake of FDG and so it is often used in cancer diagnosis and monitoring [109].

### 3. RADIOISOTOPES

---

$^{11}\text{C}$  is potentially very useful as it can in theory be substituted into almost any organic molecule. However with a half-life of just 20.3 minutes it cannot be transported any significant distance so the procedure must be carried out on the same site as the production. It is produced through the  $^{14}\text{N}(\text{p}, \alpha)^{11}\text{C}$  and  $^{11}\text{B}(\text{p}, \text{n})^{11}\text{C}$  reactions.

#### 3.1.2 Accelerator Production of Radioisotopes

In order for a reaction to occur between the nucleus of an atom and an incident particle the energy in the centre of mass frame must be greater than the Coulomb barrier which is given by:

$$E_{CB} = Zze^2/R. \quad (3.1)$$

where  $Z$  is the atomic number of the target element,  $z$  is the atomic number of the incident particle,  $e$  is the fundamental electric charge and  $R$  is the separation between the two species. Quantum tunneling however allows reactions to take place at energies much lower than that of the Coulomb barrier.

When a reaction occurs the difference between the total kinetic energy of the products and the total kinetic energy of the reactants is called the  $Q$  value. If the  $Q$  value is positive then the reaction is said to be exoergic and the reaction pathway is always available. If the  $Q$  value is negative then the reaction is said to be endoergic and a minimum energy of  $|Q|$  must be provided for the reaction to occur.

The  $Q$  factor, amongst other factors, determines the likelihood of a particular reaction pathway occurring. This probability is called the cross-section and is measured in  $\text{mb}$  or  $\text{cm}^2$ . The cross-section tends to peak when the incident particle energy is significantly greater than the coulomb barrier. As the magnitude of the coulomb barrier is dependent on the atomic number of the incident particle, cross-sections peak at higher energies for deuterons and alpha particles than for protons.

The generation of radioisotopes via nuclear reactions is countered by the natural decay of the created isotopes over time. Consequently the rate of production decreases as more of the isotope is created so this must be accounted for when calculating production rates. Other factors that influence production are the density of the target material and the incident particle flux. Combining these with the cross-section of the desired reaction gives the radioisotope production rate given in equation 3.2 [104].

$$R = nI(1 - e^{-\lambda t}) \int_{E_0}^{E_s} \frac{\sigma(E)}{dE/dx} dE, \quad (3.2)$$

where  $R$  is the net rate of nuclei formed each second,  $n$  is the target thickness in nuclei/cm<sup>2</sup>,  $I$  is the particle flux,  $\lambda$  is the decay constant of the produced nuclei,  $t$  is the irradiation time,  $\sigma$  is the cross-section of the reaction in cm<sup>2</sup>,  $E$  is the incident particle energy and  $x$  is the distance traveled by the particles in the target. As the particles will lose energy as they travel through the target the cross-section, which is energy dependent, must be integrated from the initial energy  $E_0$  to the final energy  $E_s$  of the beam.

The  $(1 - e^{-\lambda t})$  term from equation 3.2 is referred to as the saturation factor. The saturation factor determines the irradiation time used and is related to the half-life of the produced isotope. In one half-life of irradiation time the yield will reach 50% of the maximum saturated yield, for two half-lives 75% etc. Short lived isotopes like <sup>11</sup>C with a half-life of just 20.3 minutes would reach greater than 90% saturation in just 80 minutes whereas a longer lived isotope such as <sup>99m</sup>Tc would need 24 hours to reach the same level.

### 3.1.3 Targets

The targets used for radioisotope production vary widely from machine to machine. This is because the target should be designed to the characteristics of the produced beam which can differ significantly depending on the type of accelerator used. Additionally the target material can be in either a solid, liquid or gaseous state and thus require very different configurations.

#### 3.1.3.1 Internal Targets

Internal targets have several potential advantages over external targets. The first is that there is no need to extract the beam allowing for the full accelerated beam current to reach the target. This is particularly useful for positive beams where extraction efficiencies can be significantly lower than for negative beams, which can often achieve 100% extraction efficiency. Additionally with the target contained within the cyclotron, self shielding can be used with the shielding applied directly to the outside of the cyclotron. This can significantly reduce the shielding requirements of the cyclotron vault and therefore reduce costs.

The radioisotopes most commonly produced with this method are non-volatile solid elements such as <sup>123</sup>I and <sup>201</sup>Tl. Since solid targets can be exposed to the vacuum inside a cyclotron their design can be made simple and compact as in figure 3.3. Powder, liquid and gas targets are more complicated and difficult to implement in the limited space

### 3. RADIOISOTOPES

---

within a cyclotron. The target is usually placed at an angle to the beam, spreading the particles over a large area. This helps reduce the cooling requirements. By using a curved target that is matched to the curvature of the beam the power can be spread over an even larger area, reducing cooling further and allowing for higher currents to be used.

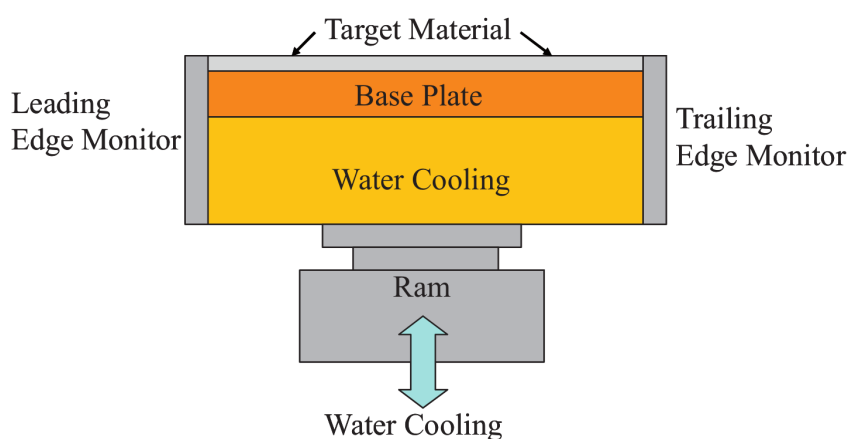


**Figure 3.3:** Diagram of a typical internal target set up. The target would be placed in such a way that the target material is at an angle to the beam, spreading the beam power over a greater area. Taken from [104].

#### 3.1.3.2 External Targets

External targets are more commonly used than internal targets. There are two main advantages that external targets bring compared to internal set ups. With the beam extracted from the cyclotron there are no constraints on the physical size of the target configuration allowing for more complicated set ups. The transfer line that takes the beam from the cyclotron to the target can be used to shape the beam. This allows it to be optimised to the target, for reduced cooling requirements or improved yields.

Solid elements can be in either powder or foil forms. If a foil is used then the target can be directly irradiated by the beam. When in powder form there must be a window that allows the beam through, but stops the powder from being released into the vacuum chamber. The physical properties of the material will affect how the target is set up. If the material is a good thermal conductor then the target can be placed perpendicular to the beam concentrating the power in a relatively small area. If the material is less conductive then the target will need to be at an angle to the beam in

order to spread the beam power over a larger area.

Liquid targets are usually similar to solid target configurations. The main differences are that there must always be a beam window to contain the liquid and the target apparatus can remain attached to the beam line at all times, with the target liquid pumped in and out simplifying operation.

Gases are less dense than solid and liquids, so gas targets tend to be larger as their stopping power is smaller and the beam is degraded over a longer distance. The gas is often pressurised to increase its density and reduce the target size. Gases are also bad thermal conductors so heat removal can be a limiting factor. The targets are usually tapered towards the entrance to account for beam growth from multiple scattering as shown in figure 3.4.

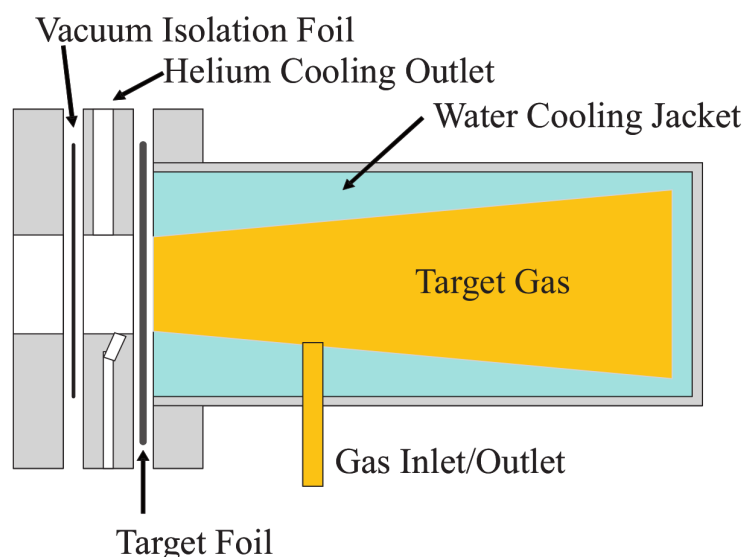


**Figure 3.4:** Diagram of a gas target. The target chamber widens to account for beam growth from scattering. Taken from [104].

### 3.1.3.3 Beam Target Interactions

As well as the nuclear interactions that produces the radioisotopes, there are several other processes that occur between the beam and the target material. Both atomic and nuclear interactions can cause an ion to lose energy in a material. Which mechanisms dominate the energy loss process is dependent on the momentum of the incident ion.

The main processes of energy loss that ions undergo in the energy range of inter-

### 3. RADIOISOTOPES

---

est for radioisotope production (low MeV's) is through the ionisation or excitation of electrons in the target material. As an ion passes through a material it collides with atomic electrons. If the collision is inelastic then energy is transferred from the ion to the electron and the electron either moves to a higher energy state or is ionised. If the energy transferred to the electron is too small to excite it to the next energy level then the collision will be elastic.

Nuclear collisions become more important at lower energies. The magnitude of deflection and energy loss incurred is related to the proximity of the ion to the target nucleus and the charge of both the incident ion and target nuclei.

As these processes are all statistical, the energy loss distribution of a mono-energetic beam after traversing a distance in a material will form a distribution around the mean energy loss. This can affect radioisotope yields as depending on the initial energy, the energy spread of the beam at the cross-section peak will be different. The mean energy loss from these processes is described by the Bethe-Bloch formula:

$$\frac{-dE}{dx} = Kz^2 \frac{Z}{A} \frac{1}{\beta^2} \left[ \frac{1}{2} \ln \frac{2m_e c^2 \beta^2 \gamma^2 T_{max}}{I^2} - \beta^2 \right]. \quad (3.3)$$

where  $K = 4\pi N_A r_e^2 m_e c^2$ ,  $N_A$  is Avogadro's number,  $r_e$  is the classical electron radius,  $m_e$  is the electron mass,  $z$  is the charge of the incident particle,  $Z$  is the atomic number of the target material,  $A$  is the atomic mass of the target material,  $\beta$  is the ratio of the incident particle velocity to the speed of light,  $\gamma$  is the Lorentz factor,  $T_{max}$  is the maximum kinetic energy that can be imparted to an electron in a collision and  $I$  is the mean excitation energy [110].

All the processes that result in energy loss also scatter the beam. The effect of multiple Coulomb scattering on the beam is described by equation 3.4

$$\theta_0 = \frac{13.6 \text{ MeV}}{\beta c p} z \sqrt{x/X_0} [1 + 0.038 \ln x/X_0] \quad (3.4)$$

where  $\theta_0$  is the average scattering angle,  $p$  is the incident particle momentum and  $X_0$  is the radiation length.

## 3.2 Conclusions

Radioisotopes are an extremely useful tool with applications across several different sectors including agriculture and industry. Medicine is perhaps the area where radioisotopes have the biggest impact as a key tool in the diagnosis and treatment of

many conditions, including many cancers.

Many radioisotopes can only be produced with particle accelerators, in particular lighter elements such as the PET isotopes  $^{18}\text{F}$  and  $^{11}\text{C}$ . Other isotopes that are currently produced mainly in research reactors such as  $^{99m}\text{Tc}$  could be produced by particle accelerators in the future, as the sector looks to diversify and decentralise the supply chain. There are also several new radioisotopes of interest to clinicians such as  $^{211}\text{At}$  that can be produced in accelerators.

If accelerators are to expand their role in radioisotope production then their economic potential must be maximised. To do this improvements must be made to the fundamental technologies to improve yield by increasing beam currents and maximising the beam to product conversion efficiency.

### 3. RADIOISOTOPES

---

# 4

## Compact Proton FFAG

### 4.1 Accelerator Design Overview

The starting point for this thesis was a field map created by Carol Johnstone and Rob Edgecock. This field map along with further iterations of the design have been characterised and analysed in this thesis.

In order to decentralise the radioisotope supply chain and create a more robust system, as discussed in chapter 3, local production methods have to be profitable enough to justify the investment. Any new machine will need to run at high currents and maximise yields by optimising the target design to improve the per  $\mu\text{A}$  radioisotope yield. With this in mind a compact accelerator with a non-scaling and non-linear field gradient has been designed for the production of radioisotopes for medical applications.

An initial design energy of 14 MeV was chosen because it coincides with the peak of the cross-section for direct production of  $^{99m}\text{Tc}$  [111], which is the most commonly used medical radioisotope and so the envisaged main product of the machine. The energy was later extended to 28 MeV to allow for the production of a wider range of medical isotopes, such as  $^{211}\text{At}$  [112]. All results presented here are for the 28 MeV version as the 14 MeV version has essentially the same magnetic field but cut off at a smaller radius. The design consists of four separate sector magnets and two radio frequency (RF) cavities as shown in Fig. 4.1. The separate sector magnets have an angular width of  $\approx 40^\circ$  leaving large drifts to ease the addition of RF cavities, injection lines, extraction devices or targets. The accelerator should be small enough to be located in the basement of a hospital without the need of a new bespoke building to house it. This will allow direct on-site production, eliminating the need for distribution infrastructure, whilst keeping costs to a minimum. As such the magnet radius is 1.3

#### 4. COMPACT PROTON FFAG

---

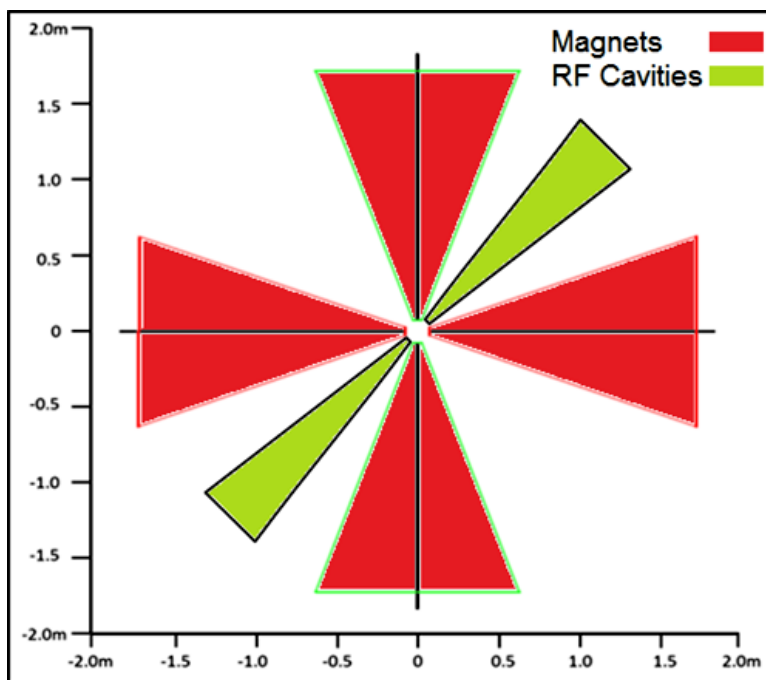


**Figure 4.1:** General layout of the design, with the position of magnets in red and RF cavity position in green. Two sectors are left empty and can be used to locate injection/extraction devices.

m at 14 MeV (for  $^{99m}\text{Tc}$ ) and 1.7 m at 28 MeV (for  $^{211}\text{At}$ ). The injection energy is 75 keV, which is sufficiently low enough to allow injection either directly from an ion source or with a small (electrostatic) intermediary accelerator. By avoiding a large pre-accelerator section, costs will be reduced and the operation made simpler.

Beam focusing within the machine is generated by three different aspects of the magnetic field. Vertical focusing is generated by edge focusing [15]. This occurs at the hill/valley transition where the magnet fringe fields create non-uniform fields away from the mid-plane which focus vertically displaced particles. This effect is focusing as the beam enters the magnet and defocusing as it exits, creating an alternating gradient structure. Radial focusing comes from weak/gradient focusing [15]. A parallel beam entering a uniform magnetic field is naturally focused from the different path lengths that the particles will take depending upon where each particle enters and exits the magnetic field. This effect is enhanced by angling the magnet edges such that the beam no longer enters and exits perpendicular to the magnet edges and by creating a positive field gradient. Both of these have the effect of bending particles at larger radii more than those at lower radii, creating a focusing effect.

The magnetic field gradient in this design does not follow the isochronous condition of equation 1.15 and is instead defined by a polynomial in the form of equation 4.1.

$$B_r = B_0 \left[ 1 + \sum_{i=1}^n b_i (r - r_{ref})^i \right], \quad (4.1)$$

where  $B_r$  is the magnetic field at radius  $r$ ,  $B_0$  is the magnetic field at the reference orbit  $r_{ref}$  and  $b_i$  is the multipole field component. The isochronicity equation assumes that the field geometry is identical at all radii. Therefore so long as deviations from equation 1.15 are compensated for by changes in the field geometry such that the integrated magnetic field stays the same, then isochronicity can be maintained. This is achieved through optimisation of the field gradient with the magnet geometry. As a result a ToF variation of less than  $\pm 0.15\%$  has been achieved, which is sufficient to allow the use of fixed frequency RF.

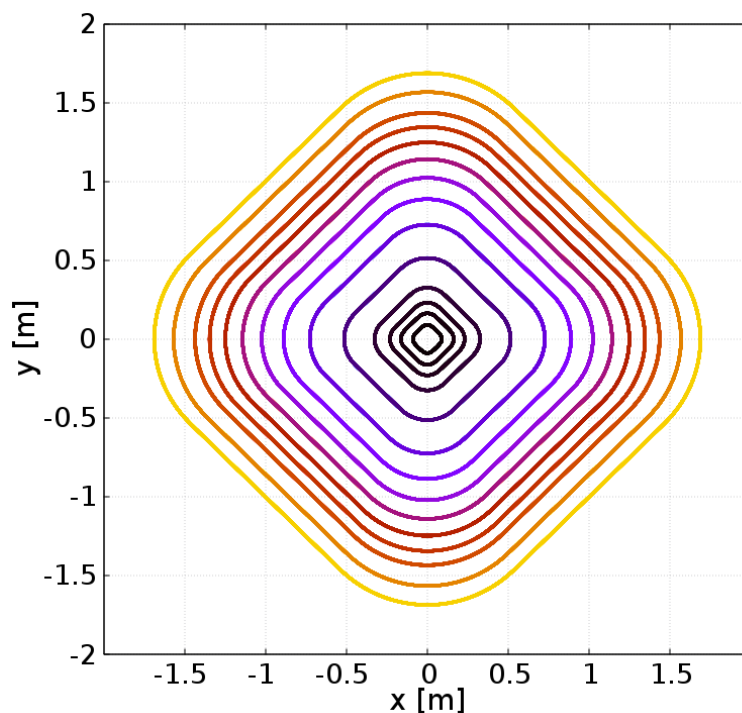


**Figure 4.2:** Closed Orbits for protons from 75 keV (at 89.4 mm) to 28 MeV (at 1686.5 mm).

### 4.2 Computational Investigation of the Design

There are three particle accelerator codes that are of relevance to this thesis. A brief description of each of them and how they contributed to this work is found below.

#### 4.2.1 COSY INFINITY

The starting point for the work contained in this thesis was a field map generated by Rob Edgecock using COSY INFINITY [113] and passed to me for detailed simulation and analysis.

COSY INFINITY uses differential algebraic techniques to compute the Taylor transfer map of the system. This offers several advantages over other types of optics code. It is computationally efficient especially for repetitive systems as only the transfer map for a single cell need be calculated, where in a ray tracing code each particle must be tracked through the entire system. Additionally through the use of differential algebra it can calculate arbitrary fields to any order, allowing the simulation of the complex fields required in FFAG's. This also enables the handling of fringe fields with relative ease.

#### 4.2.2 OPAL

The bulk of the work contained in this thesis was conducted using the OPAL [114] code. Tracking studies were carried out to characterize it, understand its capabilities and demonstrate that it works.

OPAL is a particle in cell code designed for particle accelerator optics and developed at the Paul Scherrer Institute. It includes full 3D spacecharge calculations and was designed to make use of parallel processing and HPC (High Performance Computing). OPAL has two modes it can operate in OPAL-T and OPAL-CYCL. For these studies OPAL-CYCL was used which supports imported field maps and is designed for modelling cyclotrons.

The equation of motion solved for in OPAL is the Lorentz equation as shown in equation 1.1, but where  $E$  and  $B$  vary in both time and space, and consist of both an externally applied field and a self generated spacecharge field. For a bunch consisting of  $M$  particles the evolution of the particle distribution in time is described by a collisionless Vlasov equation:

$$\frac{df}{dt} = \delta f + \sum_{j=1}^M \left[ \frac{\delta f}{\delta x_j} \dot{x}_j + q(E + c\beta \times B)_j \frac{\delta f}{\delta P_j} \right], \quad (4.2)$$

where  $f$  is the distribution function of the bunch,  $E$  and  $B$  are the electric and magnetic fields each consisting of both the external applied field and the self generated internal field [115].

OPAL supports several different types of field map, but the form used in all simulations discussed in this thesis is a median plane type map. In this type of field map the external vertical magnetic field  $B_z$  is defined at points on in the  $xy$  plane with  $z = 0$ . This map is then expanded in the  $z$  direction. Using a cylindrical coordinate system where the points are defined in  $r$ ,  $\theta$  and  $z$ , then the 3rd order expansion of the field can be written as

$$B_{(r,\theta,z)} = \begin{pmatrix} z \frac{\delta B_z}{\delta r} - \frac{1}{6} z^3 C_r \\ \frac{z}{r} \frac{\delta B_z}{\delta r} - \frac{1}{6} \frac{z^3}{R} C_\theta \\ B_z - \frac{1}{2} z^2 C_z \end{pmatrix}, \quad (4.3)$$

where  $C_r$ ,  $C_\theta$  and  $C_z$  are the partial differential coefficients. A limitation of this type of field map is that the field accuracy decreases with displacement from the median plane.

The internal space charge fields are calculated in the bunch frame. In this reference frame, the motion of the particles relative to each other is small. This allows for the magnetic term to be ignored and the electric field to be calculated by solving Poisson's equation:

$$\nabla^2 \phi(x) = -\frac{\rho(x)}{\epsilon_0}, \quad (4.4)$$

where  $\phi$  is the electrostatic potential and  $\rho$  is the space charge density. A Lorentz transformation is then used to covert back to the lab frame, restoring the magnetic component of the space charge field.

### 4.2.3 PyZgoubi

In an effort to improve certain aspects of the machine performance, some reworking of the design was conducted using PyZgoubi [116] which is discussed later in chapter 7.

PyZgoubi is a python wraparound for the particle optics code Zgoubi [117] which greatly improves the user interface by including functions for common operations and plotting scripts. The core Zgoubi code was originally written for the design of beam

#### 4. COMPACT PROTON FFAG

---

lines and magnetic spectrometers, but has been expanded to include most of the main accelerator elements such as dipoles, multipoles and FFAG magnets. It is a ray tracing code which calculates the ray trajectories using numeric integrators. This code was used because it includes elements with analytically defined magnetic fields, unlike OPAL which in OPAL-CYCL mode relies on field maps. The OPAL-T mode does allow analytical magnetic elements, but none that provide arbitrary field gradients defined by a polynomial which is necessary for the type of magnet used in this machine. The main element used for this design work was the DipoleS element, which is a sector bending magnet. The magnetic field gradient of this element could be defined using equation 4.5.

$$B_z(R, \theta) = B_{z_0} F(R, \theta) (1 + b_1(R - RM)/RM + b_2(R - RM)^2/RM^2 + \dots), \quad (4.5)$$

where  $B_{z_0}$  is the dipole field component,  $F(R, \theta)$  is the fringe field coefficient,  $R$  is the radius,  $RM$  is the reference radius, and  $b_1, b_2, \dots$  are the higher order field coefficients where  $b_1$  is for the quadrupole component,  $b_2$  the sextupole etc. The fringe field coefficient  $F(R, \theta)$  applies the fringe fields to the magnet, which are defined by the Enge function described in equations 4.6 and 4.7.

$$F = \frac{1}{1 + \exp P(d)}, \quad (4.6)$$

$$P(d) = C_0 + C_1\left(\frac{d}{g}\right) + C_2\left(\frac{d}{g}\right)^2 + C_3\left(\frac{d}{g}\right)^4 + C_5\left(\frac{d}{g}\right)^5, \quad (4.7)$$

where  $C_i$  are the shape coefficients,  $d$  is the distance from the effective field boundary and  $g$  is the pole gap which can be made to be  $R$  dependent for variable pole gap magnets.

Another feature of this type of element is that it allows the entrance and exit edges of the magnet to be rotated around a reference point independently, and to have up to two regions where the edge is curved following a set radius. The flexibility with the magnetic field gradient, fringe fields and magnet shape and position make it a very useful tool when trying to create a new field map.

One area where PyZgoubi is lacking is that it can not currently perform space charge calculations. It would therefore be useful to be able to design a magnet in PyZgoubi then export a field map into OPAL for space charge studies. Another area in which PyZgoubi is lacking is a way to export the generated field maps. To circumvent this a

script was created to write a field map file. When tracking a particle the magnetic field experienced by the particle at each step can be recorded. By setting the beam rigidity several orders of magnitude higher than normal the beam can be made to travel in a straight line. Combining these two things with a known starting position, angle and step size the magnetic field at any given point can be extracted. The script used this to generate a file in a format that could be read into OPAL.

### 4.2.4 Closed Orbits, ToF, Tunes and Dynamic Aperture

Initial work was carried out with single particle tracking in OPAL, looking to characterise certain properties of the design, to find injection parameters and demonstrate that the machine is capable of acceleration.

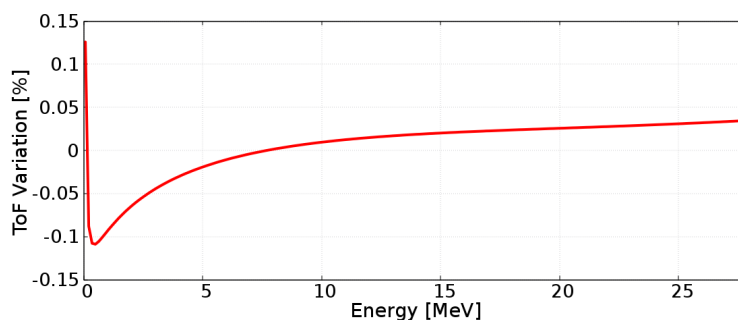


**Figure 4.3:** Time of flight variation as a function of energy. Maximum variation is  $\pm 0.15\%$  and integrated variation is  $0.632\%$ . The spread is small enough to allow CW operation.

In a stable machine for a particle of a given energy there will be an point where its path around the machine will be stable, returning to the same point and trajectory every turn. This is known as the Closed Orbit and is important as it is the reference for calculating the beam dynamics at that energy. To find the closed orbits the angular position for injection was set to  $45^\circ$  i.e. at the midpoint between magnets where the magnetic field is zero and the closed orbits are all perpendicular to the radius. At this point the radial momentum of a particle on a closed orbit is 0 at all energies. This reduces the optimisation to a single variable problem, so only the radius needs to be varied to find the closed orbit at any given energy. The closed orbits are shown in Fig. 4.2 with the injection energy orbit of 75keV occurring at 89.4 mm and extraction energy of 28 MeV at 1686.5 mm.

Having obtained a set of closed orbits the time of flight (ToF) could be calculated. Using the closed orbits positions a single particle was run for 200 turns at each energy.

#### 4. COMPACT PROTON FFAG

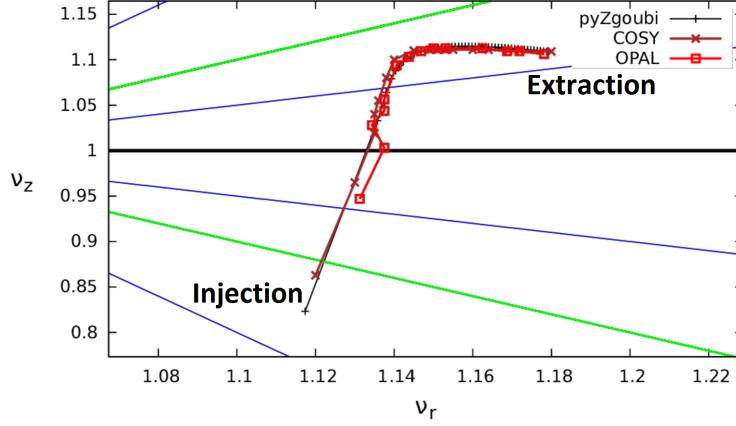


**Figure 4.4:** The betatron tunes calculated as in OPAL, COSY and pyZgoubi. All three show good agreement with each other, showing the same features such as depressed vertical tune at low energy and resonance crossing.

A probe element recorded particle information, including time, at the same point each time the particle crossed it. The time difference between each turn was calculated and averaged to generate a time of flight curve shown in Fig. 4.3. The ToFs calculated with OPAL are in good agreement with those generated by COSY. The maximum ToF deviation is less than  $\pm 0.15\%$  and the integrated percentage deviation from the average is  $0.632\%$  to 28 MeV, which is small enough for CW operation.

The betatron tunes are calculated in OPAL by tracking two particles around the machine, one on the closed orbit and one with a small displacement. A fast fourier transform (FFT) routine is then used to calculate the tunes. The tunes calculated by OPAL are show in Fig. 4.4 along with the tunes calculated in COSY and pyZgoubi, all three showing good agreement with each other. The horizontal tune increases slightly over the energy range due to the contribution from the magnetic field gradient which increases with energy. The vertical tune is stable throughout most of the energy range. At low energy however the magnets are close enough together that the fringe fields become increasingly important. The flutter is reduced as the fringe fields take up a greater proportion of the space in the drifts, eventually completely filling them. The effect of this is a reduction in vertical focusing and a suppression of the vertical tune. As a result the tune passes through several resonances including an integer resonance at  $\nu_z = 1$ . The resonances are however passed very quickly, in around a single turn for 200 kV/turn, restricting the growth of any instabilities. These sort of resonance crossings are regularly encountered in cyclotrons and the fast crossing of resonances in

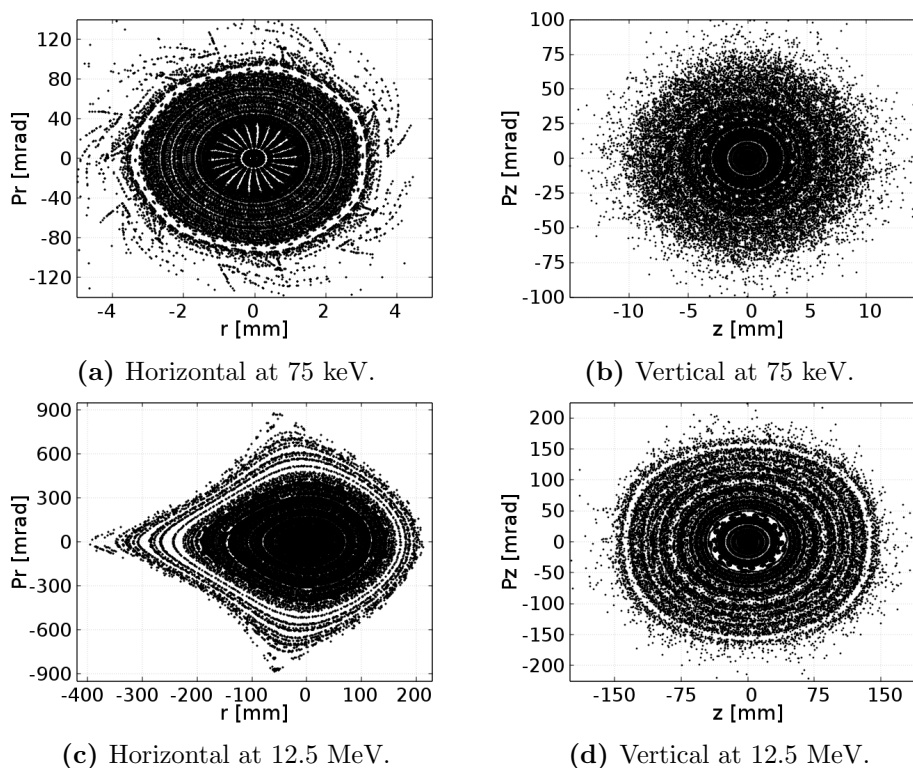


**Figure 4.5:** Dynamic Apertures in both horizontal and vertical planes. The smallest DA's are at injection (75keV) and the largest at 12.5 MeV.

an FFAG has been demonstrated by EMMA [66].

In order to cope with resonance crossings as well as other sources of emittance growth, such as lattice errors and space charge effects, it is important that the design be robust and be able to operate under a wide range of beam conditions. The Dynamic Aperture (DA) tells us the spread in beam width and momentum that the machine can accept. Large DAs will allow for the machine to accept larger emittances, and therefore better cope with high currents and resonance crossing. To investigate the DAs a distribution was set up with particles displaced at 1 mm intervals in either the horizontal or vertical planes. This distribution was then tracked without acceleration for 1000 turns and particle position and momentum recorded at a particular azimuth on each turn. This was repeated for energies up to 28 MeV. Particles were counted as lost if they left the extents of the field map. The surviving particles position and momentum were then plotted, showing the area in phase space within which the beam will be stable. The acceptances are very large peaking at  $150 \pi$  m mrad at 12.5 MeV in the horizontal and  $41.4 \pi$  m mrad at 24 MeV in the vertical planes. The smallest

#### 4. COMPACT PROTON FFAG

acceptances in both horizontal and vertical planes occur at the injection energy (75 keV). The horizontal aperture is restricted by the proximity of the injection orbit to the edge of the magnetic field, leading to a acceptance of  $0.35 \pi$  m mrad. In the vertical plane the reduced focusing from fringe field effects at injection shrink the aperture to  $0.75 \pi$  m mrad. Also worth noting is a distinct restriction in the vertical DA around 0.5 MeV, this is most likely a result of the  $\nu_z = 1$  integer resonance that is crossed around this energy. Figure 4.5 shows the horizontal and vertical dynamic apertures at 75 keV and 12.5 MeV. In the horizontal DA for 12.5 MeV you can see the phase space distortion of large amplitude particles creating a distinctive stingray like shape. This is caused by the sextupole component of the magnetic field gradient. In the vertical DA at the same energy you see a squaring of the DA at larger amplitudes. This is related to the number of sectors in the machine, i.e. three sectors=triangle, four sectors=square.

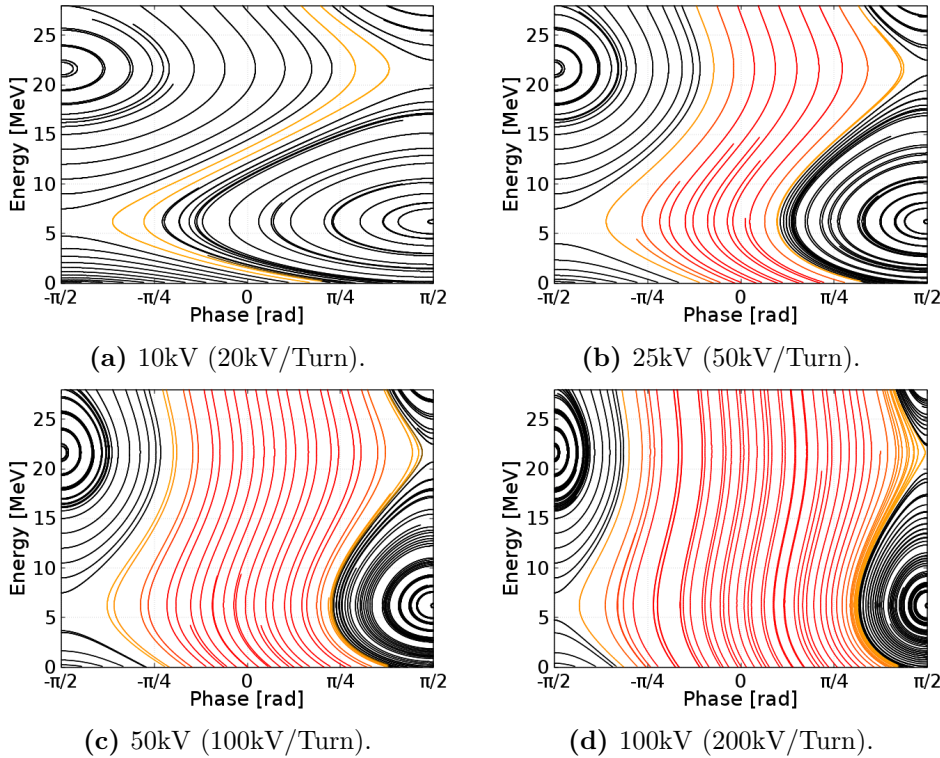


**Figure 4.6:** The RF phase space for various cavity voltages at the first harmonic. At 20kV/turn a acceleration channel to 28 MeV opens up but with very limited phase acceptance. For greater phase acceptance and reduced energy spread a voltage of  $>100$ kV/turn or more is needed.

### 4.2.5 Acceleration

With the lattice well characterised and understood, the study moves on to examining the behaviour of the machine when accelerating particles.

First the basic conditions under which acceleration can be achieved to the desired energy were found. An initial starting position and trajectory was found that would put the beam onto an accelerated orbit. Two single gap RF cavity elements were placed in opposite valley sectors. The radial voltage profile of the cavities was set to be constant across the width of the cavity and initial phases set such that an ideal reference particle will arrive at the first cavity on the first turn when the phase is  $0^\circ$  (where  $0^\circ$  is the peak of the RF wave). The voltage on the RF cavities was then varied to find the minimum necessary to accelerate to 28 MeV.

It was found that an acceleration channel that reaches the design energy opens up at a voltage of around 20 kV/turn. The phase acceptance ( $\Delta\phi$ ) at this voltage is very small, so a minimum of around 50 kV/turn would be needed in order to have a reasonable phase acceptance. This would give a phase acceptance of  $\Delta\phi = 65^\circ$ . Figure 4.6, shows the RF phase-space for voltages from 20-400 kV/turn at the first harmonic. A cross crest acceleration regime is used where the phase slip takes the particle phase across the crest twice before reaching the design energy. By optimising the traversing of the crest like this, the energy spread of the beam can be reduced. Depending on which side of the RF crest the beam is on, either the head or the tail particles will be nearer the crest. By crossing the crest you expose both leading and trailing particles to equivalent areas of the phase space, but on opposite sides of the crest. The effect of increasing the voltage is to reduce the total phase slip, which in turn increases the phase acceptance. This also reduces the energy spread at extraction (for the same initial phase spread).

The first harmonic however is not ideal from an engineering perspective as a 7.5 MHz,  $\lambda/2$ , first harmonic RF cavity would have a long dimension of around 20 m. By using a higher harmonic the size of the cavity can be reduced as higher frequencies have shorter wavelengths. A sixth harmonic cavity would have a long dimension of around 3 m. The phase slip however increases with harmonic number as the RF phase is changing more quickly. A balance must therefore be made between cavity size and acceleration efficiency. Figure 4.7 shows the affect that the harmonic number has on the RF phase space if the accelerating voltage is kept the same. The accelerating channel becomes restricted as the harmonic number is increased and will eventually close. At 100 kV/turn the highest usable harmonic is the 5th beyond which the beam can no

#### 4. COMPACT PROTON FFAG

---

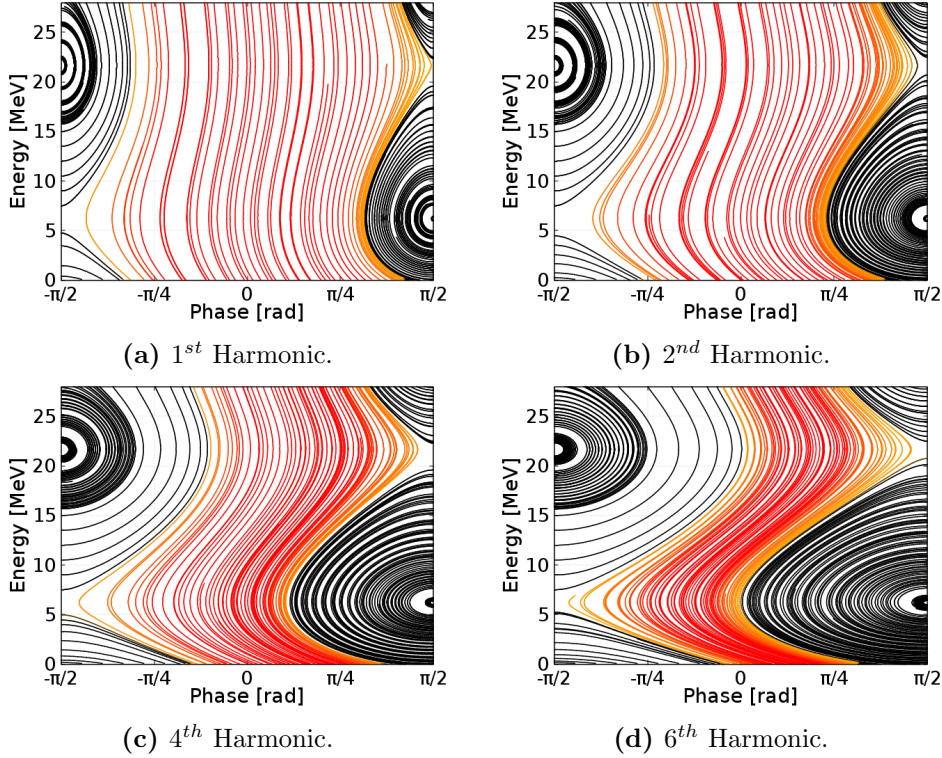


**Figure 4.7:** The RF phase space for different harmonics at 200kV/Turn. As the harmonic number increases so does the phase slip, so a compromise must be made between the harmonic number and the accelerating efficiency. Otherwise increasing the accelerating voltage can compensate for the increased phase slip.

longer reach 28 MeV.

Having accelerated the beam to the required energy you must extract it from the machine. In order to do so successfully whilst incurring low losses, you must have good separation between the turns at the extraction energy. A key factor in this is the accelerating voltage as it defines the energy difference between the orbits. To investigate, a single particle was accelerated and tracked to the extraction energy for accelerating voltages of 50-200 kV/turn, with a probe placed in one sector to record the position each turn. The turn separation was then calculated by simply subtracting the previous turn position from the current turn. Figure 4.8 shows the turn separation as a function of energy for the different voltages. Increasing the voltage leads to greater turn separation. The relationship is linear and the factors affecting this ratio are the radius, energy and voltage as shown in equation 4.8[118]:

## 4.2 Computational Investigation of the Design

$$\frac{dR}{dn_t} = \frac{\gamma}{\gamma^2 - 1} \times \frac{R}{\zeta + 1} \times \frac{V_t}{m_0 c^2}, \quad (4.8)$$

where  $\gamma$  is the Lorentz factor of the particle,  $\zeta$  is the field index and  $V_t$  is the accelerating voltage [V/turn]. For 200 kV/turn the turn separation is 3.5 mm at 28 MeV, too small to extract a high current beam by an electrostatic deflector. There are various techniques that can be used to increase the turn separation such as using off-centred orbits to induce a coherent oscillation around the reference orbit, which can be optimised to create larger separation at a particular point in the machine.

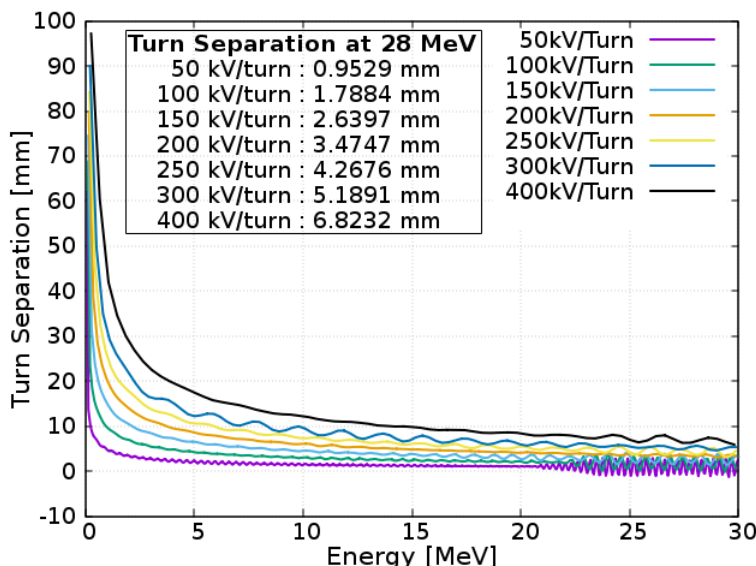


**Figure 4.8:** Turn Separation for voltages from 50-400 kV/Turn. The separation reduces with increased energy making extraction difficult. Increasing the accelerating voltage increases the separation linearly.

With an understanding of the basic characteristics of the design from single particle tracking the investigation moved on to looking at the behaviour of a bunch in the machine. Multi-particle simulations of a bunch were conducted, initially without space charge, to investigate the effects of various parameters on the beam emittances, in particular the final emittances at extraction. The emittances produced from the OPAL simulations referred to in this section and in later chapters are normalised statistical emittances. They are calculated from the RMS position and momentum relative to the bunch centroid.

Coupling between the different planes can have a big effect on the beam dynamics.

#### 4. COMPACT PROTON FFAG

---

To investigate these effects within this design an initial bunch of 1/1/1 mm sigma was injected and accelerated using 200kV/Turn at the 4th harmonic. The bunch size in each dimension was then increased incrementally whilst keeping the others at 1 mm, and the effect on the final beam emittances recorded, plotted and fitted. The strongest coupling comes from the longitudinal dimension. The coupling from longitudinal to radial dimension results in the emittance being proportional to  $\tan(\sigma_y)$  as seen in Fig. 4.9. The coupling arises predominately from the increased energy spread in the beam as the bunch fills up more of the available RF phase space causing different parts of the beam to see different accelerating voltages. A similar but weaker effect is also seen in the longitudinal to vertical coupling. Weak coupling from radial to vertical was observed whilst coupling from radial to longitudinal and from vertical to radial/longitudinal was negligible.

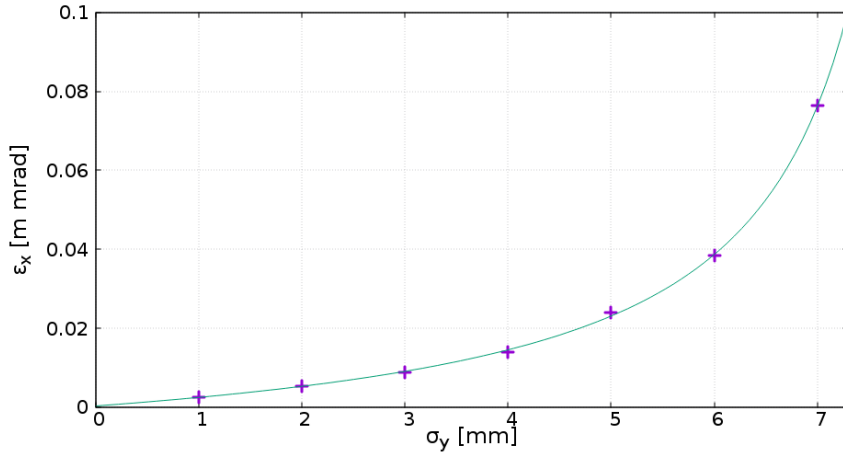


**Figure 4.9:** Effect of increasing the longitudinal length of the beam on the final radial emittance of the beam. Crosses are simulation result, line is a  $y \propto \tan(x)$  fit.

The accelerating voltage can have a significant effect on emittances. One way in which it can do so is in its effect on the rate of resonance crossing. Higher accelerating voltages will result in resonances being crossed quickly, reducing the window in which instabilities can grow. Conversely a low acceleration voltage will cause slow crossings that will allow time for instabilities to become destructive. Another effect is on the energy spread of the beam, which reduces with increased voltage. Lower voltages mean more turns are needed to reach the desired energy. Given that at any particular energy the phase slip/turn is constant, more turns will result in an increased total phase slip. Additionally, since the beam is not well confined longitudinally in this type of

## 4.2 Computational Investigation of the Design

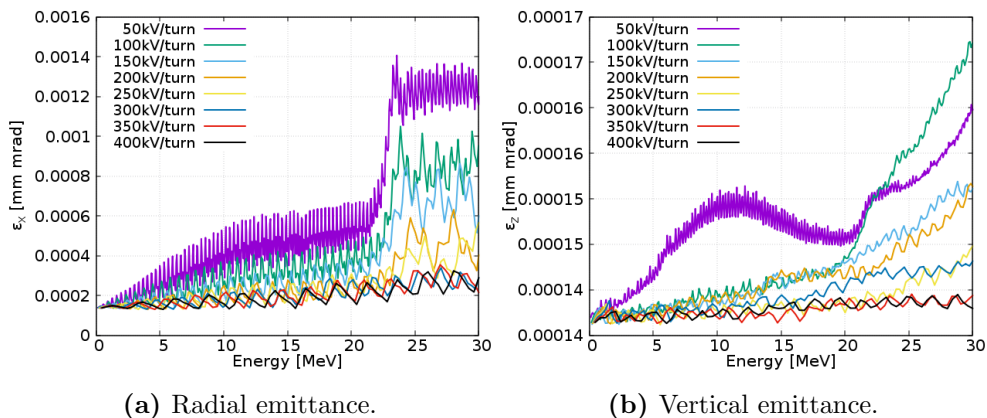


**Figure 4.10:** Emittances as a function of accelerating voltage. Lower voltages result in higher emittances. At around 22 MeV there is a artefact that is causing significant growth for voltages less than 250 kV/turn.

accelerator, lower voltages will allow more time for the beam to spread out longitudinally. Figure 4.10 shows how lower accelerating voltages result in larger emittances. Fig. 4.10a shows increased radial emittance growth with lower accelerating voltages due to a combination of the reasons given above. Interestingly there is a marked increase in emittance around  $\approx 22\text{MeV}$  for voltages of 250 kV/turn or less, especially at lower voltages. This behaviour is typical of a resonance crossing, however there are no major resonances (up to 3rd order) around this energy. Figure 4.10b shows the vertical emittance increasing with lower voltages, although the pattern is less consistent than for the radial direction. There is also an increase in the emittance growth rate at around  $\approx 22\text{MeV}$ , but somewhat less pronounced than seen in the radial emittance.

### 4.2.6 Helium Acceleration

Whilst radioisotopes such as  $^{99m}\text{Tc}$  can be created with protons, there are many that require alternative particles for production. Expanding the range of particles that can be run in the machine will make it more versatile and potentially more productive. The obvious particle to try to run in the machine is  $\text{He}^{2+}$ , as it is the next ion up from protons in terms of its mass and charge. The charge to mass ratio of  $\text{He}^{2+}$  is  $\approx 1/2$  (compared to 1 for protons) and its velocity for the same total kinetic energy is half that of protons (at non relativistic energies). Using equation 4.9 you can show that the beam rigidity therefore is approximately the same for  $\text{He}^{2+}$  and protons apart for relativistic effects. In the energy range of interest, neither protons or  $\text{He}^{2+}$  are very relativistic and so their rigidities vary very little, around 0.9% at 28 MeV, as you can see

#### 4. COMPACT PROTON FFAG

---

in fig 4.11. This variation leads to a ToF curve that is linearly decreasing with energy and has a spread of approximately  $\pm 1.5\%$ . This translates to an operating frequency of 3.634 MHz, approximately half that of protons. This opens up the possibility of running the same RF frequency for both protons and  $\text{He}^{2+}$ , with protons operating at the 1<sup>st</sup> harmonic and  $\text{He}^{2+}$  at the second. Whilst the ToF spread is approximately  $\times 10$  that of protons, having a 2+ charge state means that it gains twice as much energy per turn than protons for the same RF voltage.

$$BR = \frac{p}{e} = \beta\gamma \frac{m_0 c}{e}. \quad (4.9)$$

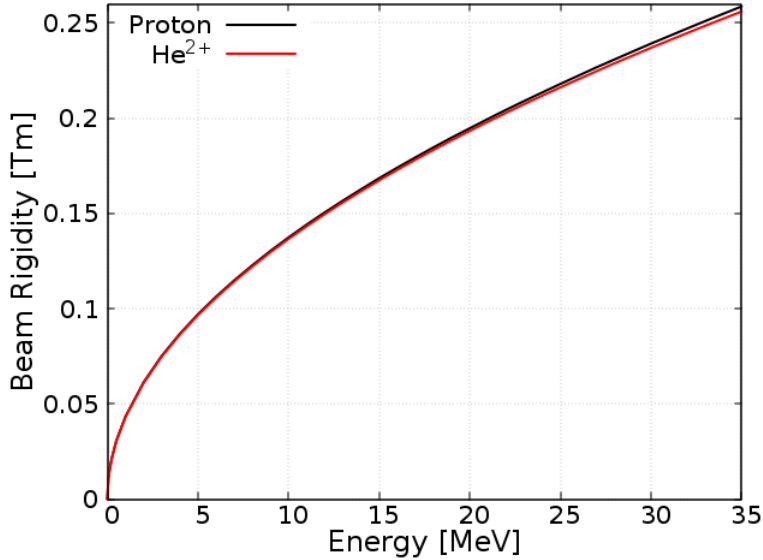


**Figure 4.11:** Beam rigidity of protons and  $\text{He}^{2+}$  in the energy range up to 35 MeV. At 28 MeV the rigidities vary by less than 0.9 %.

As the beam rigidities are almost identical for protons and alphas, the trajectories that they follow in the machine are as well. This leads to very similar transverse beam dynamics. The tunes shown in fig 4.12a, match very closely with only a small amount of deviation at higher energies as the rigidities begin to diverge due to relativistic effects. As with protons several resonances are crossed at low energy however the 2+ charge state of  $\text{He}^{2+}$  means that the resonances are crossed twice as quickly for the same accelerating voltage as protons. This should make  $\text{He}^{2+}$  more resilient to resonance crossings and therefore less sensitive to field errors. The dynamic apertures are also very similar as shown in fig 4.12b, with both horizontal and vertical DAs following the

## 4.2 Computational Investigation of the Design

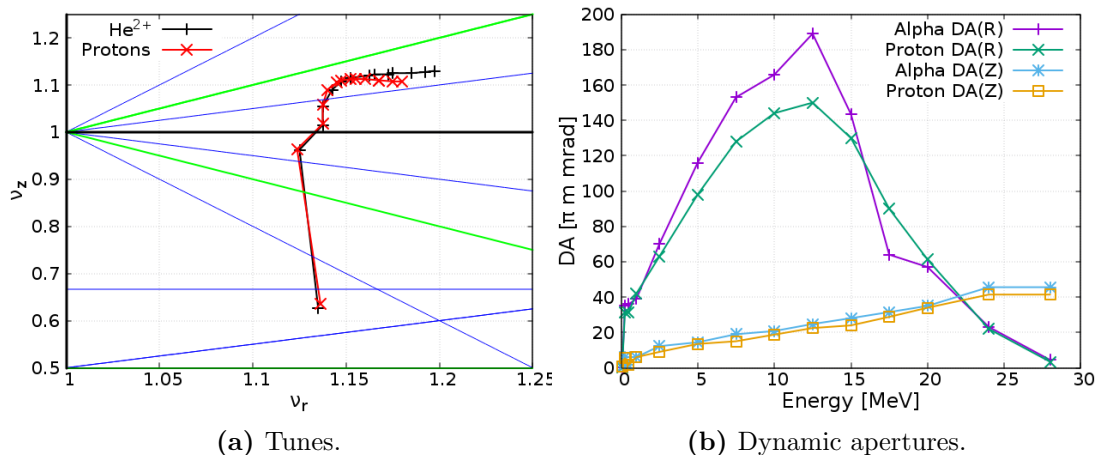


**Figure 4.12:** Comparison of betatron tunes and dynamic apertures for protons and  $\text{He}^{2+}$ .

same pattern as for protons across the energy range, but with the  $\text{He}^{2+}$  DAs being slightly larger.

Although the increase in acceleration from the 2+ charge state of  $\text{He}^{2+}$  does help compensate for the larger ToF spread, the phase slip is still increased. With a ToF spread of almost  $\times 10$  that of protons but double the acceleration, the phase slip is approximately  $\times 5$  what it was for protons as can be seen in fig 4.13. For the first harmonic at 200kV/Turn the phase acceptance is significantly lower than that of protons at  $\approx 35^\circ$  for  $\text{He}^{2+}$  compared to  $\approx 130^\circ$  for protons. This becomes even more problematic if trying to go to higher harmonics. Even at the second harmonic 200kV/Turn is not enough to open a channel all the way to the desired energy. By 300kV/Turn a narrow channel is created but a much higher accelerating gradient is needed to achieve a decent phase acceptance. Harmonics higher than the 2<sup>nd</sup> would require gradients that are not practically possible and therefore are not an option.

Since running at higher harmonics is not practical with  $\text{He}^{2+}$  further simulations of bunch behaviour concentrate on the dynamics when running on the 1<sup>st</sup> and 2<sup>nd</sup> harmonics. Although the tunes and dynamic apertures are very similar for protons and  $\text{He}^{2+}$ , there are significant differences in the longitudinal dynamics due to the increased phase slip. A simulated 1/1/1 mm sigma bunch was injected and accelerated using the 1<sup>st</sup> harmonic and 300 kV/Turn to 28 MeV. Despite the lattice being identical and the beam rigidities very similar, the emittances shown in fig 4.14 are significantly different from those of protons. The coupling from the longitudinal to the radial and vertical planes is discussed in section 4.2.5 and is evidenced again here in the emittances. The radial emittance (fig 4.14a) correlates strongly with the energy spread of the beam(fig 4.14d),

## 4. COMPACT PROTON FFAG

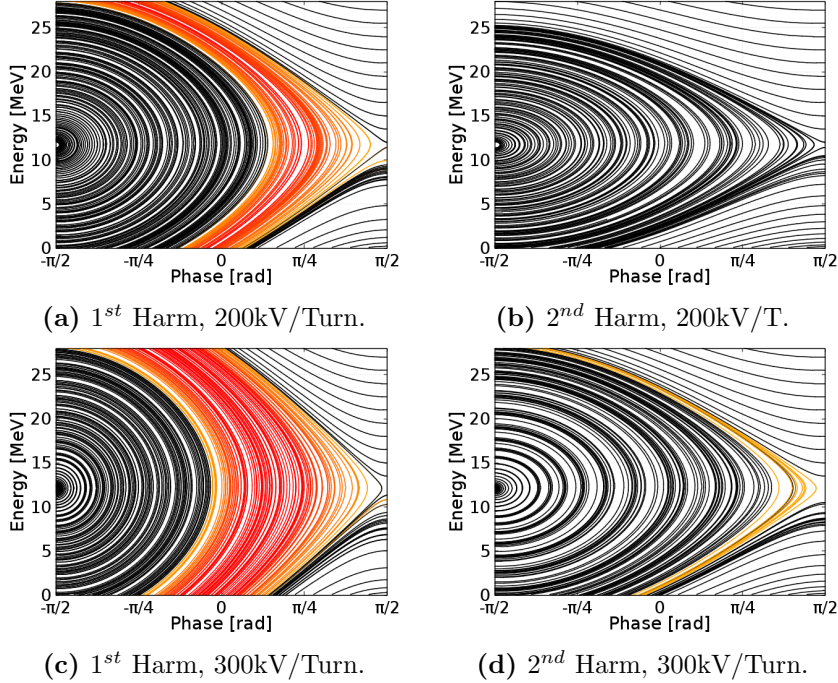


**Figure 4.13:** RF phase space for  $\text{He}^{2+}$  ions at different harmonics and voltages. By the second harmonic an accelerating gradient of at least 300kV/Turn is required.

which is much larger in this case than for protons. The simulation was repeated but operating at the 2<sup>nd</sup> harmonic and the emittances are also shown in fig 4.14. The larger phase slip at the 2<sup>nd</sup> harmonic results in larger emittances, as the acceleration is less efficient and the energy spread greater. This is evident in the longitudinal and vertical emittances which are significantly larger than when using the 1<sup>st</sup> harmonic, both throughout acceleration and at the final energy. In the radial emittance and energy spread you can see significantly larger values at points during the acceleration, but at the final energy there is little difference between the 1<sup>st</sup> and 2<sup>nd</sup> harmonics. This is because as the bunch crosses the crest twice on the way to the final energy, the net deceleration at either end of the bunch gets evened out as discussed in section 4.2.5.

### 4.2.7 Field Errors

Whilst it is possible to demonstrate the properties and performance of the machine through the simulations detailed in this section, the reality is often not quite as simple. The simulations conducted so far have used a field map that fits perfectly with the designed magnet geometry and field gradient apart from some interpolation between

## 4.2 Computational Investigation of the Design

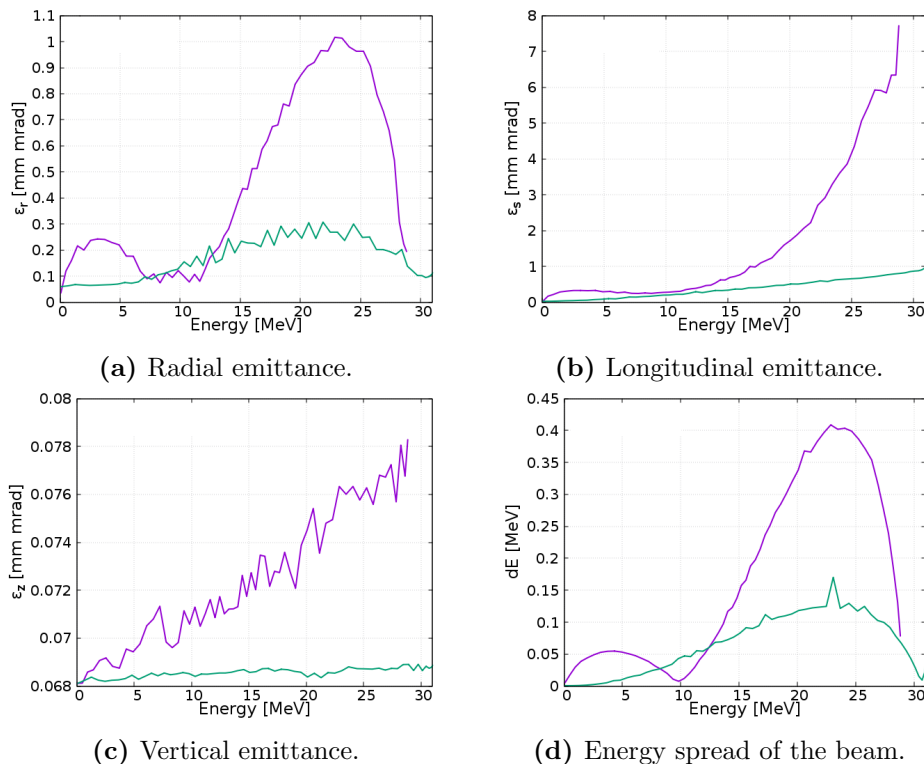
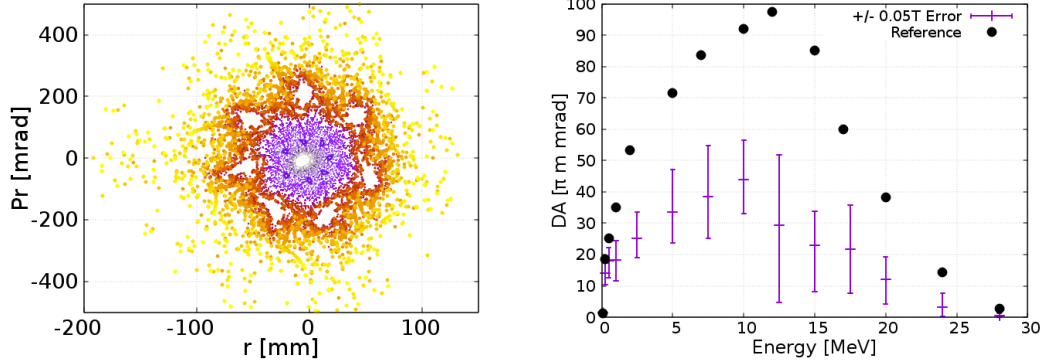


**Figure 4.14:** Emittances and energy spread for Alphas at 1<sup>st</sup> (Blue Line) and 2<sup>nd</sup> (Purple Line) harmonics for 300 kv/Turn.

defined field points. Once constructed and operated in a real environment the field will diverge from the designed parameters. Tolerances in manufacturing of the magnets will result in small errors in the field at any given point. Construction errors could result in misalignments between different components of the machine. There can also be operational errors induced from sources such as temperature changes, fluctuations in the power supply and human error. To help us understand how the the design will operate under such conditions, errors can be introduced to the field map and simulations run to determine their effect on machine performance.

One possible type of error is a random field error due to manufacturing tolerances. To simulate this the magnetic field map was modified by adding a random number ( $n_i$ ) to each field point. This number was generated randomly for each grid point in the range of  $\pm N$ , such that the average value of  $n_i$  was 0 and the average value of  $|n_i|$  was  $N/2$ . Simulations were then run for incrementally increasing values of  $N$ , assessing the changes to the dynamic aperture with the modified field map. For each value of  $N$ , 10 field maps were generated and simulated and the dynamic apertures at each

#### 4. COMPACT PROTON FFAG



(a) Distortion of the dynamic aperture at 5 MeV for a  $\pm 0.05T$  field error. Colour indicates the initial displacement of the particle. The lighter the colour the greater its initial displacement.

(b) Dynamic apertures for a random field error of up to  $\pm 0.05T$ .

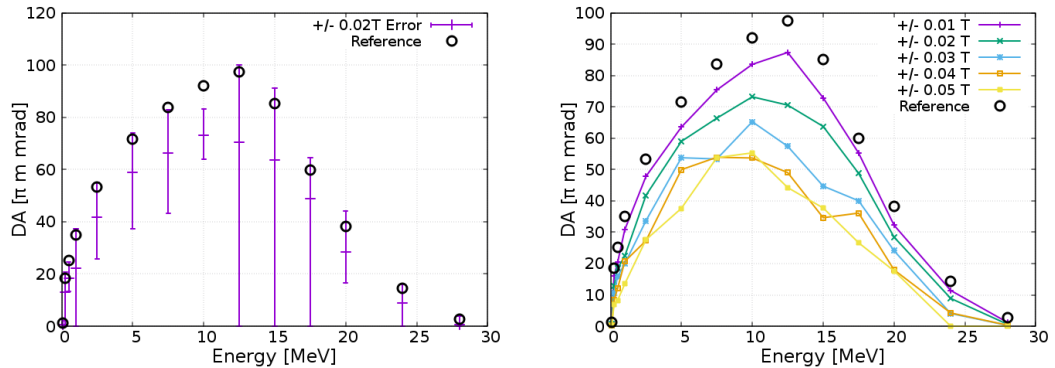
**Figure 4.15:** Dynamic aperture distortion and restriction for a random field error

energy averaged. Figure 4.15 the effect of this type of error on the dynamic apertures. The shape of the DAs become distorted as shown in fig 4.15a and the motion of large amplitude particles start to become chaotic. This has the effect of shrinking the DAs. In fig 4.15b the restriction of the radial DA for a  $\pm 0.05$  T random error can be seen. The DAs are restricted by up to 70% but remain reasonable as the starting DAs are very large. An error of  $\pm 0.05$  T is approximately 5% of the field and much larger than would be expected in a real machine.

Rather than a random error at each field point, the error could alternatively be a systematic error across the whole of a particular magnet. This could cause an error whereby the dipole component of the field gradient is shifted by the same amount across the whole of a particular magnet. Field maps were generated to simulate this using the method mentioned above, but rather than applying a random error to each field point the same random error is applied to all field points in a sector magnet. This results in varying dipole field components in each of the four sector magnets. Figure 4.16 shows how the dipole error affects the dynamic apertures across the energy range. Due to the smaller number of individual errors applied in this situation (1 per sector magnet), there is a greater chance of the errors being grouped together, ie. all very large or all very small. Consequently the range of dynamic apertures observed is much larger than for the same equivalent error when applied to every field point.

Alignment errors are another source of errors in real machines. This design with separate sector magnets makes alignment errors more likely than cyclotrons made out

## 4.2 Computational Investigation of the Design



(a) Dynamic apertures for a dipole component field error of up to  $\pm 0.02T$ .

(b) Average dynamic apertures for a dipole component various degrees of field error.

**Figure 4.16:** Average dynamic apertures for a dipole component field error

of a single ion block as each magnet will need to be positioned precisely relative to each other. Unfortunately there is no easy way to replicate alignment errors in OPAL. The alignment errors would have to be calculated by hand or by a bespoke algorithm before being entered into COSY. The field maps generated by COSY then need to be converted to a form readable by OPAL and then simulations run to calculate the dynamic apertures. Unfortunately there was not enough time to undertake this analysis.

The error analysis shows that the design is reasonably resilient to field errors. There is only a 15% average drop in DA for a 0.01T dipole error, which is a larger error than would be expected for a real machine installation. Although simulations were not run to test alignment errors, the resistance to random field errors and dipole field errors suggests that it will likely be resistant to this type of error as well.

#### 4. COMPACT PROTON FFAG

---

# 5

## Space Charge Studies

### 5.1 Proton Dynamics Under Space Charge

The yield of cyclotron produced radioisotopes is proportional to the current delivered to the target as defined in equation 3.2 [104], which is discussed in more detail in chapter 3. As such the commercial viability of cyclotron based radioisotope production is reliant on being able to deliver medium to high currents, with higher currents potentially increasing the profitability of the operation. Typical beam currents for commercially operating radioisotope cyclotrons are in the hundreds of  $\mu\text{A}$  for small PET cyclotrons (10-20 MeV). The Advanced Cyclotron Systems (ACS) TR-13, that operates at TRIUMF, is an example of this type of cyclotron. It can deliver a  $>100 \mu\text{A}$  beam current [119]. Larger higher energy (20-70 MeV) cyclotrons, such as the IBA Cyclone70 [120], can operate at higher currents, typically from around  $500 \mu\text{A}$  to the low mA range.

When running at high beam currents, space charge effects within the bunch are the dominant cause of emittance growth and hence beam losses. The emittance growth comes from the Coulomb repulsion that occurs between particles of the same charge sign. Coulomb's law describes the magnitude of the force between two charged particles and is given in equation 5.1.

$$F = k_e \frac{q_1 q_2}{r^2}, \quad (5.1)$$

where  $F$  is the force between the two particles,  $k_e = 1/4\pi\epsilon_0$ ,  $q_1$  and  $q_2$  are the two charges and  $r$  is the distance between them. Since electric fields superpose, the force from a group of charges on a charged particle at its edge is simply given by the sum of the force from each particle. Every particle sees the field from every other particle in

## 5. SPACE CHARGE STUDIES

---

the bunch and so for a spherically uniform charge distribution the field in the centre is 0 and increases linearly to the edge of the distribution. As such, particles away from the centre of a bunch are forced outward.

So far we have only considered the static forces between particles. If these were the only forces within the bunch then at high currents the outer particles would be ejected from the beam very quickly. In an accelerator however the charges are moving and so we must consider the electrodynamic effects, i.e. the magnetic side of the electromagnetic force. The magnetic field from a continuous line current is given by equation 5.2.

$$B = \frac{\mu_0 I}{2\pi r}, \quad (5.2)$$

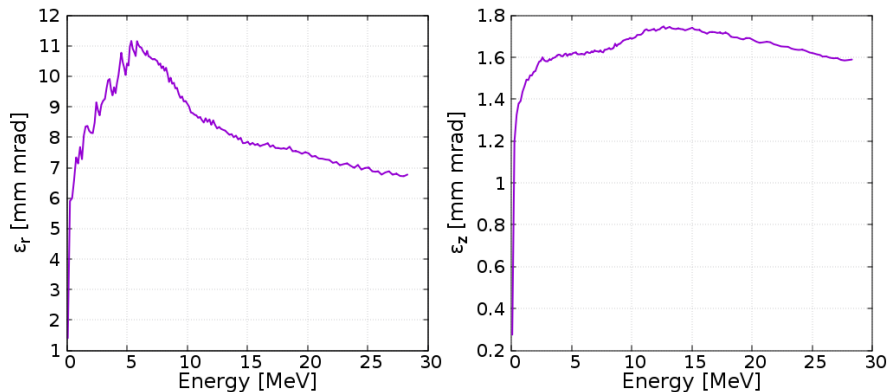
where  $B$  is the magnetic field,  $\mu_0$  is the permeability of free space,  $I$  is the current and  $r$  is the distance from the line current. By the right hand rule, a second parallel current will experience a force towards the first and vice versa. Since the current density is largest at the centre of a bunch this has the effect of attracting particles at the edges towards the centre of the bunch.

Beam growth from space charge effects is most prevalent at low energies when particles are not very relativistic[121]. The forces from the magnetic and electric fields have opposite signs and are in a ratio of  $(v/c)^2$ , so that as the beam becomes relativist and  $v$  approaches  $c$  the forces balance. One way of thinking of this is to imagine a relativistic particle within a moving bunch. In the reference frame of this particle, time dilation causes the repulsive forces from other particles to be applied over a shorter time period than elapses in the lab frame. Thus as a beam becomes more relativistic, the rate of emittance growth from space charge is reduced, as observed in the lab frame. Unfortunately in the energy range that this machine was designed to operate in (75keV to 28 MeV), relativistic effects are quite small and so space charge driven emittance growth is a major concern.

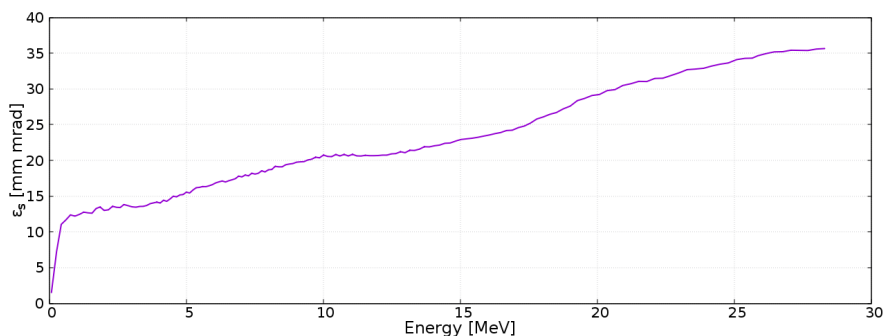
Another way in which machine performance is affected at high currents is the space charge induced tune shift. As a displaced particle undergoes betatron oscillations it will experience a repulsive force from the charge density at the centre of the bunch. This has the effect of slowing the transit of the particle across the bunch centroid and so suppressing the tune. The theoretical space charge limit for a circular accelerator is the condition whereby space charge induced tune shift reduces the effective beam focusing until either  $\nu_z$  or  $\nu_r$  is equal to 0 [122]. This is can be particularly problematic in and near the central region of cyclotrons as the machine flutter is greatly reduced due to overlapping fringe fields [123]. As a result the vertical tune is already suppressed

## 5.1 Proton Dynamics Under Space Charge

and so the beam current required to reduce it to  $\nu_z = 0$  is smaller.



(a) Radial and Vertical normalised emittances for a 20 mA beam current. Whilst there is significant growth at low energies the emittances stabilise once past  $\approx 5$  MeV.



(b) Longitudinal emittance for a 20 mA beam current.

**Figure 5.1:** Emittances for a 20 mA beam current.

Simulations were run to investigate these effects and determine the maximum current that the design can handle. Bunches of up to  $10^6$  macro particles were run, however most simulations including the results show here were run with  $10^5$  particles to keep the computational time reasonable. This should still be enough particles to see realistic effects within the bunch. Most of these simulations were run on a laptop and made use of OPAL's parallel processing capabilities by running with 8 threads on 4 cores. Simulations could take up to 24 hours to compute depending on the number of macro particles, the step size used and the length of the simulation.

The beam current was incrementally increased starting from 0.01 mA until the space charge forces became so strong as to break the beam up before reaching 28 MeV. The simulations showed the acceleration to the design energy was possible with currents of up to 20 mA. Beyond 20 mA the internal forces start to break the beam up before it can reach 28 MeV and large losses are observed.

## 5. SPACE CHARGE STUDIES

---

At 20 mA the emittances undergo large growth in the first few turns before levelling off in the horizontal and vertical as shown in fig 5.1a. This initial growth is a result of the lack of relativistic effects to dampen the space charge forces at low energy and the reduced focusing in the central region.

Another factor is the interaction between space charge and the machine tunes. Nominally the beam passes through several resonances at low energy including the  $\nu_z = 1$  at approximately 0.3 MeV and  $\nu_r - 2 \times \nu_r = -1$  at around 1.3 MeV. The space charge effects could be exciting these resonances causing growth in the amplitude of betatron oscillations. Additionally, the space charge induced tune shift could lead to the crossing of further resonances or slowing the crossing rate of current ones. These effects cause rapid growth until the beam becomes large enough to start to reduce the space charge forces. Simultaneously the vertical focusing is increased by the greater flutter at larger radii and the radial by the increasing field gradient. As this occurs the emittance growth slows down until eventually it reaches a stable state. Peak emittances are 11 mm mrad in the radial and 1.7 mm mrad in the the vertical. The reduction in emittance observed after the initial growth is caused by the loss of higher amplitude particles and a reduction in the energy spread from the cross crest acceleration regime, as discussed in section 4.2.5. The final emittances are approximately  $\times 5$  and  $\times 6$  the initial emittances for the radial and vertical planes respectively.

After this initial stage the longitudinal emittance continues to experience significant growth as seen in figure 5.1b, whilst the radial and vertical emittances are more stable to 28 MeV. This longitudinal emittance growth is due to the lack of RF focusing from synchrotron motion [124]. In an idealised isochronous cyclotron the revolution frequency is the same for all energies. The beam therefore is always operating at transition, and the particle phase is constant. Consequently if a collective effect such as Coulomb repulsion causes a particle to move relative to the bunch there is no restoring force to compensate. As such the repulsive forces cause the beam to lengthen longitudinally as well as increasing the energy spread of the beam. The peak longitudinal emittance of 35 mm mrad occurs at the final energy and is approximately  $\times 35$  its initial value.

Having established the dynamic limitations of the machine under space charge conditions, the potential losses with realistic physical restrictions were studied. In order to investigate this, apertures to simulate the beam pipe were applied. In the horizontal plane the only apertures are dynamic and occur at the inner and outer radii of the magnets where the fields drops off. The vertical plane however is restricted by the beam pipe, which in turn is limited by the magnet pole gap. Currently there aren't

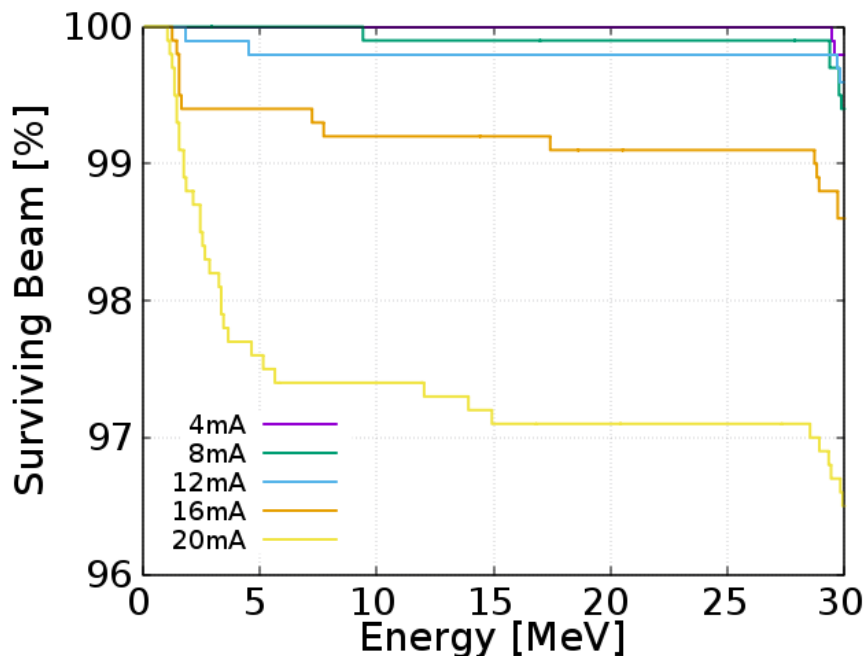


**Figure 5.2:** Beam losses on a  $\pm 20$ mm aperture. Losses are first observed at 8 mA and continue to grow, reaching 2.9% by 20mA.

any detailed designs for the magnets so an aperture size of  $\pm 2$  cm was selected based on gap sizes of currently operating cyclotrons [125]. Any particles hitting the aperture are deleted from the simulation and their position and momentum saved in a *.loss* file. With this aperture applied simulations were run recording the losses. At 20 mA approximately 2.9% of the simulated particles are lost before reaching 28 MeV, with the most severe losses recorded at low energies. This represents a total loss of  $580 \mu\text{A}$  over the whole acceleration range. These levels of losses could cause activation issues, however the low energies at which the majority of the losses occur should reduce the activation risk. Lowering the current to 12 mA these losses are reduced to 0.2 % ( $240 \mu\text{A}$ ), and the losses drop to 0 at 4 mA and below.

The strength of space charge effects is not only a function of the beam current but also of the bunch size and shape. The larger the bunch the more spread out the charge and so the space charge effects are reduced. There are however various limitations on how large the bunch can be in the machine. The magnet pole face creates a physical aperture that puts an upper limit to the size of the beam vertically. The need to extract cleanly necessitates that the orbits do not overlap, thus limiting the radial size of the beam. Longitudinally the beam size is limited by the RF phase space, use too much of

## 5. SPACE CHARGE STUDIES

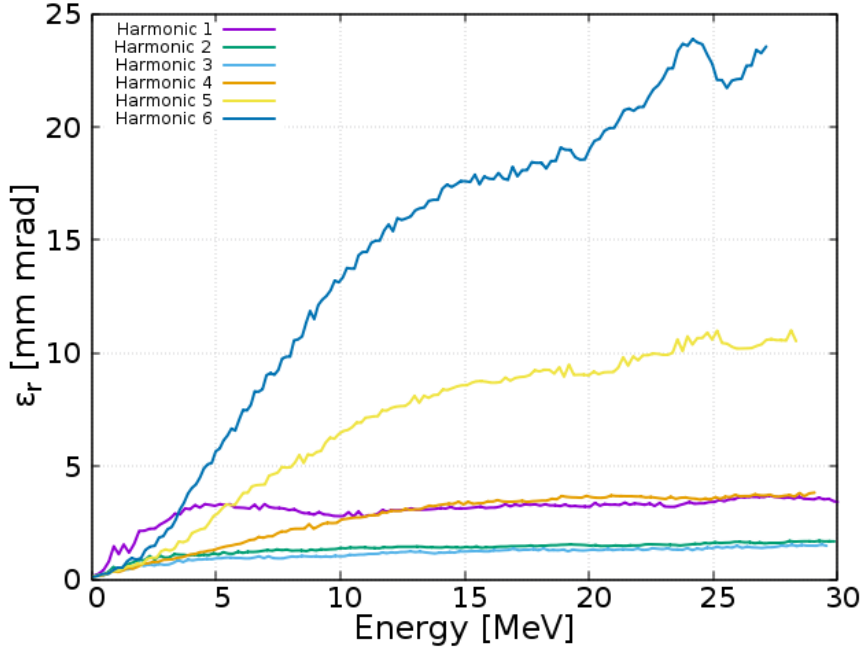


**Figure 5.3:** Radial emittances for a 5mA, 2mm spherical bunch at varying harmonics. The 2nd and 3rd harmonics produce the lowest final emittances.

it and the energy spread starts to grow, go beyond it and particles will start to fall out of the accelerating phase and be lost. The 1st harmonic is in theory the best harmonic to run at for space charge considerations as it allows for the longest bunch to be used. The fundamental frequency of this design is 7.152 MHz. At the 1st harmonic a half wavelength will occupy half the revolution time, and therefore theoretically results in a maximum beam length at injection of approx 31cm. Ideally you would use a maximum of  $20^\circ$  of RF phase space to reduce energy spread, leaving 3.5cm maximum injected beam length. At higher harmonics the bunches are restricted to shorter lengths (1.5cm at the 2nd, 1.17cm at the 3rd) but you can have multiple bunches on a single orbit as there will be  $h$  RF buckets per orbit, where  $h$  is the harmonic number. So for a 1mA beam you will have  $2 \times 500 \mu\text{A}$  bunches at the 2nd harmonic,  $3 \times 333 \mu\text{A}$  at the 3rd harmonic and so on. The larger phase slip at higher harmonics however results in an overall decrease in the usable RF phase space as the harmonic number is increased.

Although the harmonic number only directly affects the longitudinal dynamics, coupling from the longitudinal to the transverse planes means that it affects the horizontal and vertical as well. The main coupling effects come from the energy spread of the beam. The dispersion and chromaticity means that increases in energy spread feeds

into the horizontal plane causing emittance growth. Although this also occurs in the vertical plane, the dispersion and chromaticity are smaller and so the coupling from the longitudinal is much reduced.

For a given bunch size and accelerating gradient there will be an ideal harmonic to run at. Figure 5.3 shows the radial emittance for a 5 mA, 2mm  $\sigma$  spherical bunch running at different harmonics. It shows that the best harmonic to run at for such a configuration is 2nd (14.304 MHz) or 3rd (21.456 MHz), where the current per bunch is 2.5 mA or 1.66 mA respectively. This becomes increasingly important at very high currents as shearing forces in long beams start to break the bunch up, creating spherical micro bunches which is discussed further in section 5.2. To avoid this, using multiple smaller spherical bunches at harmonics  $> 1$  may be a better configuration under strong space charge effects.

An interesting effect that is observable at higher beam currents is the breaking up of an elongated bunch into smaller micro bunches as mentioned above. In figure 5.4 you can see the longitudinal beam profile on turn 150 (of 153) as the beam current is increased. As the current increases filamentation begins to develop and eventually the beam starts to fragment as it tries to form micro bunches. This occurs because of shearing effects found within the beams of isochronous circular accelerators that develop into vortices [126]. Since vortices are necessarily circularly symmetric, long beams will have multiple vortices that will ultimately evolve into micro bunches [122]. These vortices form as particles at the head of the beam gain energy, and drift adiabatically to a slightly larger radius. Simultaneously particles towards the tail of the bunch lose energy and drift to a lower radius. Over time this sets up a motion where the inner edge of the bunch is moving backward relative to the bunch centre and the outer edge is moving forward. This causes filamentation which forces the beam to become spherical [124]. If the bunch is a lot longer than its width then the motion cannot be maintained over the whole bunch length and the shearing forces induced will break the beam up and form several individual vortices.

## 5.2 Space Charge Effect in He<sup>2+</sup> Beams

The space charge effects in He<sup>2+</sup> ion beams are related to its charge and mass. Its 2+ charge state is double that of a proton, whilst its mass is approximately  $\times 4$  the mass of a proton. This has two competing effects. Consider the space charge induced tune shift in equation 5.3:

## 5. SPACE CHARGE STUDIES

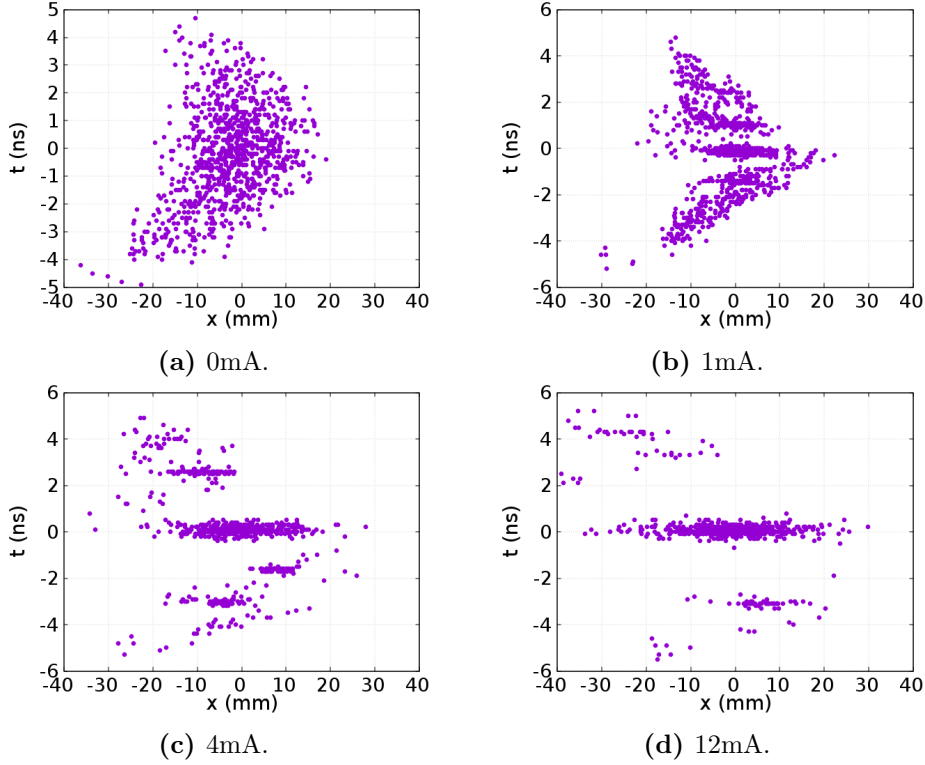


**Figure 5.4:** Longitudinal shape of a proton bunch on the 150th turn at increasing beam currents. The development of filamentation and micro bunching under strong longitudinal space charge forces is observed.

$$\Delta Q = \frac{Nq^2}{m_0\epsilon\beta^2\gamma^3}, \quad (5.3)$$

where  $\Delta Q$  is the tune shift,  $N$  the number of particles,  $q$  the particle charge,  $m_0$  the particle rest mass,  $\epsilon$  the beam emittance and  $\beta$  and  $\gamma$  are the relativistic terms. The 2+ charge state increases the magnitude of the forces between individual particles, whilst the increased mass reduces the acceleration of the particles under the space charge forces, lessening their effects. These effects compete and in this case the increase in charge is canceled out by the increased mass. The mass also means that for the same total kinetic energy, the particles are traveling at half the speed of protons, resulting in lower  $\gamma$  and  $\beta$  values. Consequently the particles are less relativistic than protons, which enhances the space charge effects relative to a proton. Also worth noting is that because of the 2+ charge state there are half the number of  $\text{He}^{2+}$  ions per unit of beam current than for protons.

To investigate how these effects play out, simulations were set up to accelerate

## 5.2 Space Charge Effect in $\text{He}^{2+}$ Beams

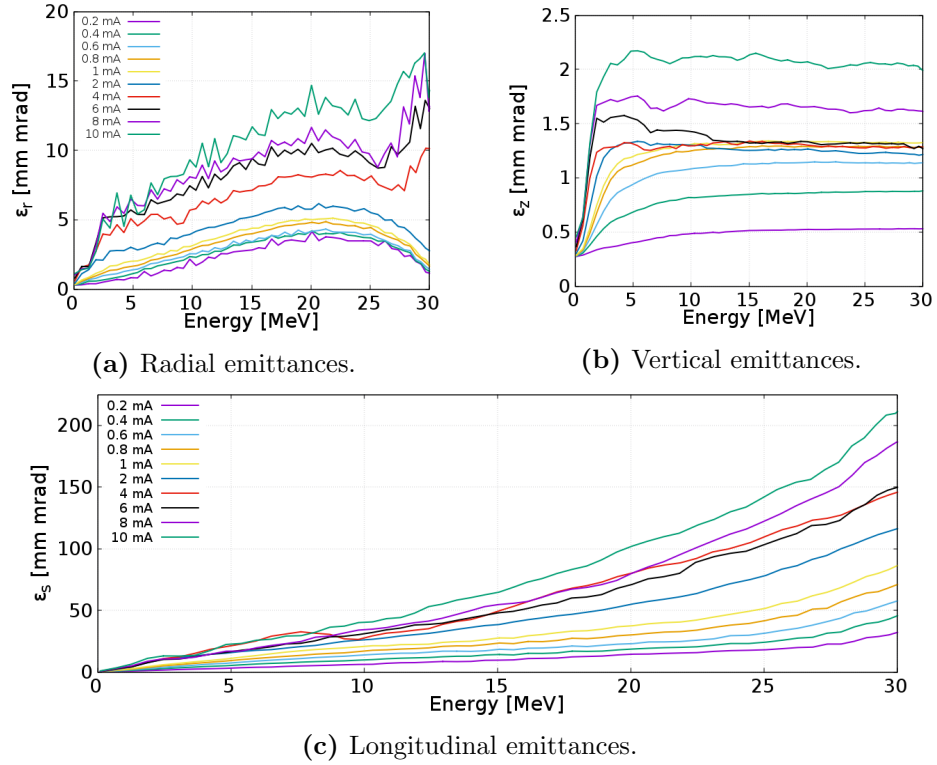


**Figure 5.5:** Radial and vertical emittances for a  $\text{He}^{2+}$  beam at various beam currents.

$\text{He}^{2+}$  with space charge. The beam current was incrementally increased to find the limit at which the space charge forces become destructive. Figure 5.5a shows the radial emittance for varying beam currents. With increasing current the beam experiences greater emittance growth, however there are a couple of points where the emittance growth is more severe. At around 1 MeV and again at 25-28 MeV there are sudden increases in the emittance growth rate. These areas of emittance growth are only apparent at beam currents of greater than 2mA.

One possible explanation for this could be that at higher currents the space charge induced tune shift is causing the beam to cross a resonance that it would not otherwise have encountered. The second period of emittance growth could have another explanation, the breaking up of the beam into micro bunches under space charge forces which is discussed below. In the vertical plane there are none of the resonance like regions of emittance growth. Instead there is a smoother more predictable pattern of growth. As with the radial plane there is an effect that is visible above 2mA, the emittances at these beam currents are suppressed from what is expected. This is in fact a result of the larger amplitude particles being lost, thus reducing the apparent emittance.

## 5. SPACE CHARGE STUDIES

---

The rate of losses on the vertical aperture are shown in figure 5.6. As with the proton studies discussed in chapter 5.1, a  $\pm 20$  mm aperture was applied. Losses are first observed at  $800\mu\text{A}$  and increase with the beam current reaching  $\approx 33\%$  at  $10\text{mA}$ . As expected the majority of the losses occur at low energy ( $>5\text{MeV}$ ) where the vertical tune is suppressed and the relativistic effects are minimal. The rate of losses at beam currents above  $1\text{mA}$  are high enough that activation of the machine and its surroundings would be a major concern and so it would not be possible to run at these currents without reducing the losses (eg. by having a larger pole gap/accelerating gradient), or mitigating/controlling them (eg. by careful collimation of the beam at low energy).

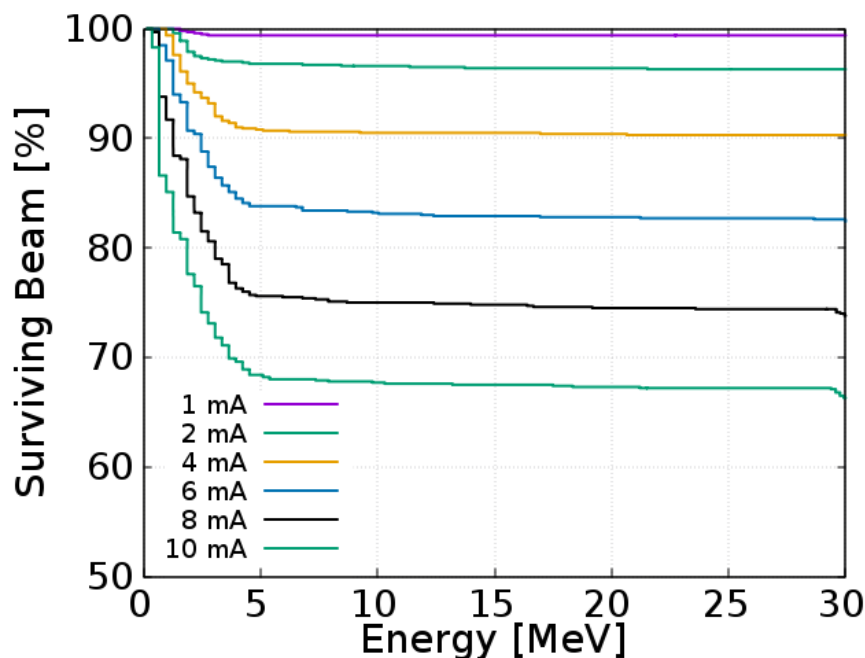


**Figure 5.6:** Beam losses on a  $\pm 20\text{mm}$  aperture. Losses are first observed at  $800\mu\text{A}$  and continue to grow, reaching  $33\%$  by  $10\text{mA}$ .

In the longitudinal plane the emittance increases with beam current as expected and as there is no longitudinal confinement, the emittance grows over the entire length of acceleration. As with protons there is break up of the beam into micro bunches at high current. Fig 5.7 shows the longitudinal beam profile near the end of acceleration under increasing beam currents. You can see the development of first filamentation of the beam developing into complete micro bunches. During this process there is significant growth in the energy spread of the beam and losses are observed.

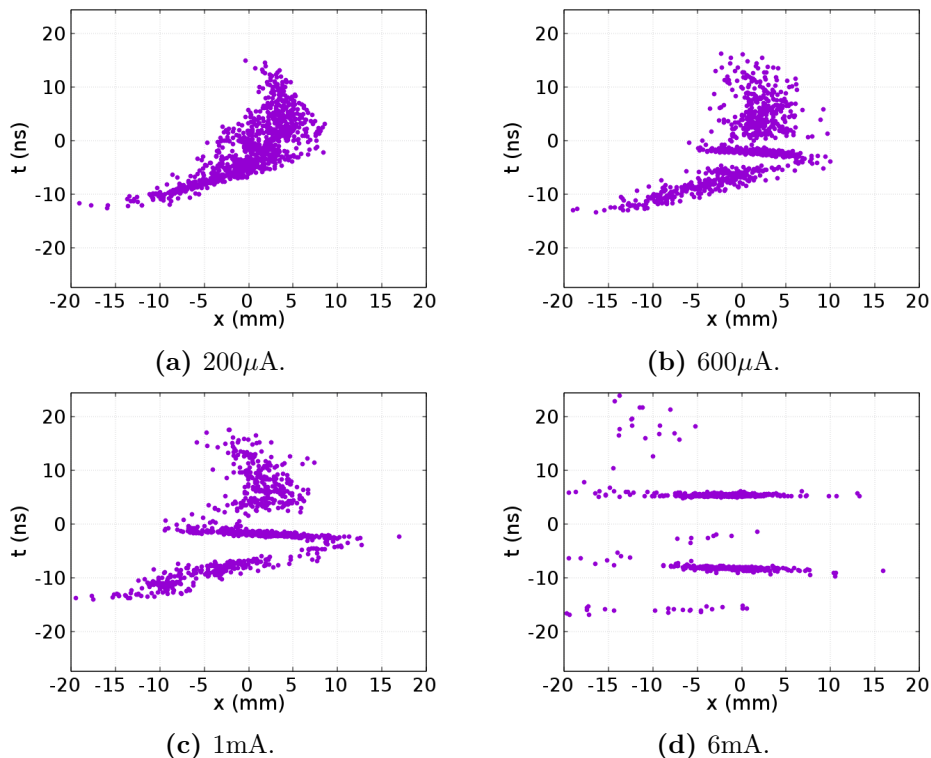


**Figure 5.7:** Longitudinal shape of a  $\text{He}^{2+}$  bunch on the 60th turn at increasing beam currents. The development of filamentation and micro bunching under strong longitudinal space charge forces is observed.

## 5.3 Conclusions

The simulations undertaken here show that the design is capable of handling high beam currents of both protons and  $\text{He}^{2+}$  ions. Protons can handle more current than  $\text{He}^{2+}$ , capable of up to 4mA with no losses and 20mA with 2.3 % beam losses.  $\text{He}^{2+}$  ions could be taken to 800 $\mu\text{A}$  with minimal beam losses. The majority of the losses for both protons and  $\text{He}^{2+}$  occur at low energy, so a good collimation system could be effective at mitigating losses and reducing the likelihood of problematic activation of materials. Using higher harmonics reduces the amount of charge in each bunch, but the larger phase slip reduces the usable RF space. Consequently there is an ideal harmonic for best coping with space charge, in this case the 2nd or 3rd for protons. Only the first harmonic is usable for  $\text{He}^{2+}$  as its phase slip is too large and RF phase space constricted. Using longer bunches could help reduce the space charge forces within the beam, but at high currents the formation of micro bunches must be considered to avoid

## 5. SPACE CHARGE STUDIES

---

emittance growth and losses.

It is useful to consider this performance in relation to other commercially available cyclotrons. The main producers of cyclotrons for radioisotope production are IBA, Best and ACS. All these manufacturers make 30 MeV cyclotrons and it would be trivial to extend this design from 28 MeV to 30 MeV with minimal changes in performance, so these machines are appropriate for comparison purposes.

Best produce the “30P” which can provide two  $400\mu\text{A}$  proton beams [127]. ACS make the “TR-30” which will produce a 1.2 mA proton beam and can also be configured to accelerate deuterons to 15 MeV [128]. IBA produce 4 variants of Cyclone 30 (all 30 MeV maximum energy), two of which are comparable to this design. The high current “Cyclone 30 HC” is capable of delivering up to a 1.2 mA proton beam. The “Cyclone 30 XP” is a multi-particle machine capable of supplying 30 MeV protons ( $400\mu\text{A}$ ), 15 MeV deuterons ( $50\mu\text{A}$ ) and 30 MeV alphas ( $50\mu\text{Ae}$ ) [129].

This design compares favorably being able to reach higher proton currents than any of these machines. Additionally it can reach higher alpha currents without compromising the proton performance. The acceleration of deuterons has not yet been investigated for this design, however deuterons are rarely used due to concerns over activation.

## 6

# Internal Target Studies

Generating a high current beam and getting it up to the right energy will allow the generation of radioisotopes. But if a large number of these accelerated particles can't be converted into the desired substance then all that effort was for nothing. Consequently optimising the target design is critical.

The reaction cross sections for the production of radioisotopes are often highly energy dependent and consequently there is a particular energy where yields will be maximized. When a beam of particles hits a thick target they are scattered and lose energy. As a result of this energy loss ( $dE/dx$ ), many particles will have moved off the cross-section peak before reacting. To compensate for the energy loss, the beam is often accelerated beyond the ideal energy so that its energy can degrade through the cross section peak. This can improve the yield but many particles still will not react and the technique is most effective when the cross section peak is quite broad.

A thin internal target and recycled beam could potentially take advantage of the cross section peak to increase yields. In a thin internal target the beam is accelerated to the perfect energy at the peak of reaction cross section. When the beam hits the target none of the particles are stopped in the target other than those that undergo a reaction. Instead they pass through the target after losing some energy and being scattered. The particles that haven't reacted on the first pass through the target are now slightly below the ideal energy of the cross section peak. They continue around the machine and are re-accelerated in the process. Now back at the ideal energy, they return to hit the target a second time. This can be repeated over multiple turns keeping the energy at cross section peak each time. By controlling the interaction energy in this way peaks of other unwanted reactions that might lower the yield can be avoided, and the purity of the product improved. The key to making this technique work is ensuring

## 6. INTERNAL TARGET STUDIES

---

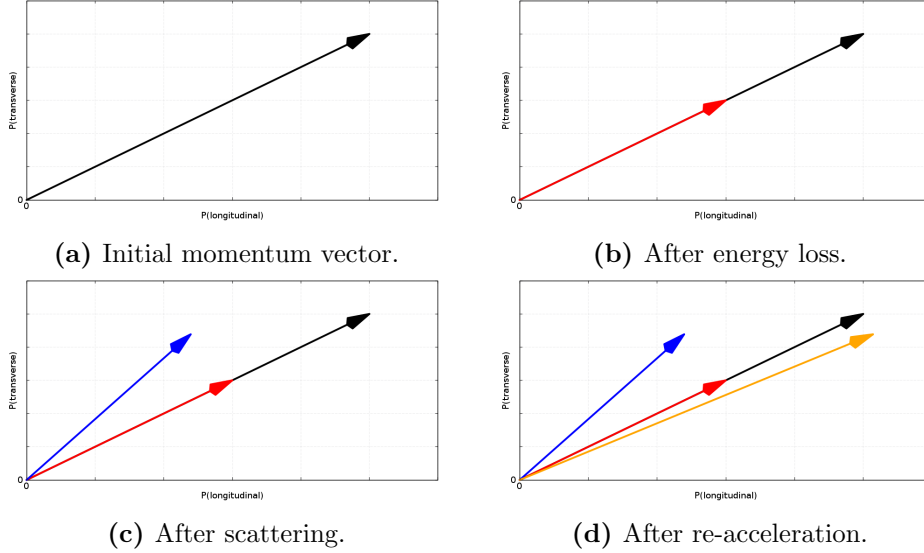


**Figure 6.1:** Visualisation of how Ionisation cooling works to reduce the angle of the momentum vector through energy loss and re-acceleration

that beam survives for a sufficient number of turns so that all the particles have an opportunity to react, and ensuring that the correct amount of energy is given to the particles each turn to keep them at the cross section peak. To maximise the beam survival, understanding and controlling the scattering through the target is essential. Ensuring that the beam continues to sit at the cross section peak each turn requires careful matching of the RF to the energy lost in the target each turn.

This technique has been demonstrated on the ERIT storage ring at the Kyoto University Research Reactor Institute (KURRI) [130] as described in chapter 2. Designed for Boron Neutron Capture Therapy (BNCT),  $H^-$  ions are accelerated to 11 MeV by a linac before being injected into the ERIT storage ring via charge exchange. The ring is a scaling FFAG design with mean radius of 2.35 m and consists of 8 DFD triplet sectors. The magnetic field at the mean radius is 0.825 T and 0.723 T for the F and D magnets respectively and the full pole gap is 15 cm [62]. With this set up they were able to achieve between 500-1000 turns through the target and achieve a neutron yield of greater than  $5 \times 10^8 \text{ n cm}^{-2}\text{sec}^{-1}$ .

### 6.1 Ionisation Cooling

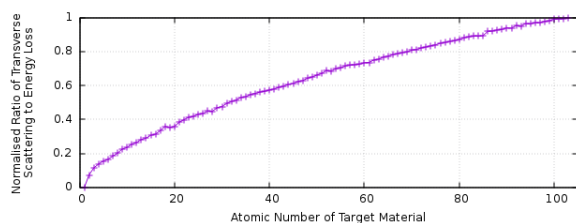
Ionisation cooling [65] is a technique whereby reaccelerating a beam after it has undergone energy loss and scattering through a material, the transverse emittance can

be effectively reduced. It was first proposed as a method of cooling muon beams by Budker and Skrinsky [131] and is still being pursued for that purpose with the Muon Ionization Cooling Experiment (MICE) at the Rutherford Appleton Laboratory (RAL) [132]. It has also been considered for cooling light ion beams such as protons and deuterons [133][134]. It works by using the longitudinal acceleration to reduce the transverse angles to the reference trajectory. A particle's trajectory will be at an angle  $\theta$  to the longitudinal axis (fig 6.1a). When the beam interacts with a material it undergoes energy loss and scattering. The energy loss reduces the magnitude of the particle's momentum vector (fig 6.1b), and the scattering rotates it (fig 6.1c). When it then undergoes reacceleration, the additional momentum is added only to the longitudinal component of the vector (fig 6.1d). After this process the resultant momentum vector has the same magnitude as the starting vector but an angle  $\phi$  that is smaller than the original angle  $\theta$ . The net result is an overall reduction of the emittance. For this technique to be effective the ratio of scattering angle to energy loss must be small.

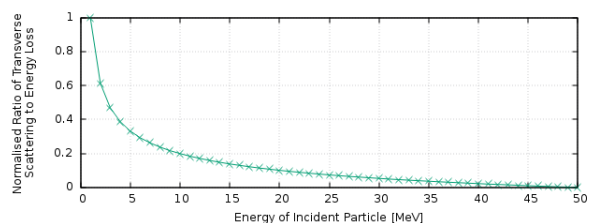
The energy loss in a material is given by the Bethe-Bloch equation defined in equation 3.3 and the multiple Coulomb scattering is given in equation 3.4. From these equations the relationship between particular variables and the scattering/energy loss ratio can be examined. Figures 6.2 show the effect of various factors on the scattering/energy loss ratio. They are derived directly from equations 3.3 and 3.4, and are normalised between 0:1 over the ranges examined. The atomic number of the target material has a significant effect, with low  $Z$  materials being highly preferred. Higher energy incident particles also produce a lower scattering/energy loss ratio, whilst increasing their atomic number reduces it. Its worth noting that for particles with the same velocities (i.e. the same MeV/u, ignoring relativistic effects) a higher atomic number reduces this ratio. The lower velocities of higher  $Z$  particles with the same total energy negates any benefits of the higher mass. [135]

To demonstrate the effect of ionisation cooling in this particular setup with a Molybdenum target, a comparison was conducted in OPAL. A simulation was run with a 0.005 mm thick target placed half way between two of the sector magnets. Scattering through the target was simulated, but energy loss was not, and no RF cavities were used. This setup allows the emittance growth from the scattering without any ionisation cooling effects to be observed. Another simulation was run with the same setup but with energy loss and RF cavities turned on to simulate ionisation cooling. Figure 6.3 shows the emittance growth with and without ionisation cooling, demonstrating that the beam is cooled, with the ionisation and re-acceleration countering the emittance growth from the multiple Coulomb scattering.

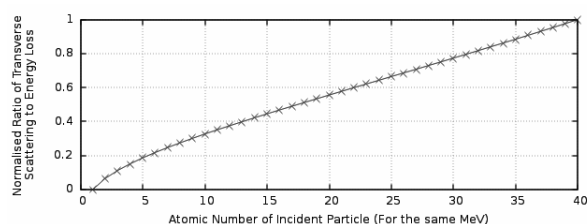
## 6. INTERNAL TARGET STUDIES



(a) Dependence of the ratio of scattering/energy loss on atomic number of the target material.



(b) Dependence of the ratio of scattering/energy loss on total kinetic energy of incident particle.



(c) Dependence of the ratio of scattering/energy loss on the atomic number of the incident particle.

**Figure 6.2:** How different factor affect the efficiency of Ionisation cooling.

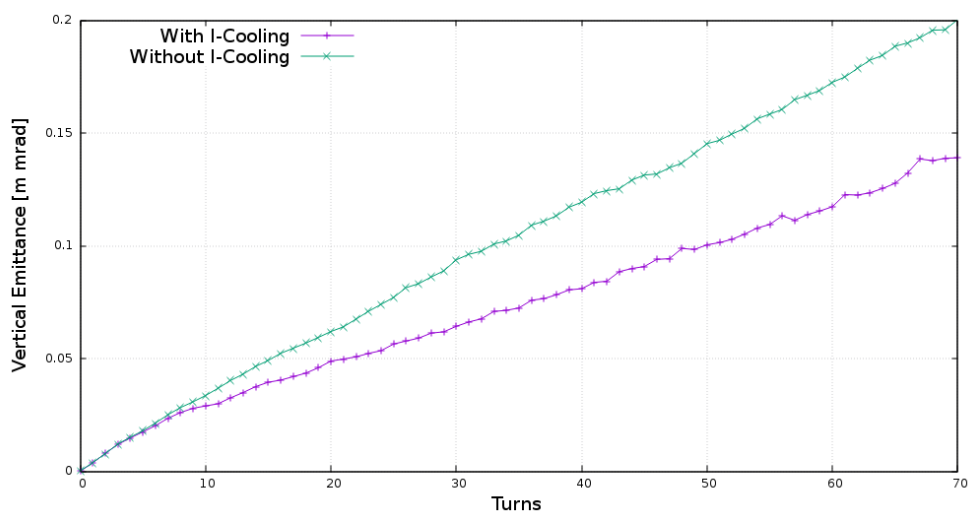


**Figure 6.3:** Emittance growth with and without ionisation cooling showing the emittance suppression effect.

### 6.2 Computational Investigation of an Internal Target

Simulations were performed to investigate whether an internal target and ionisation cooling could be used to improve yields of  $^{99m}\text{Tc}$ . A simulated target was placed at the

## 6.2 Computational Investigation of an Internal Target

radius corresponding to the peak of the production cross section of  $^{99m}\text{Tc}$  which is at approximately 14 MeV. The beam was then injected at 75 keV and accelerated to the target. A  $\pm 20\text{mm}$  vertical aperture was applied to simulate the beam pipe, and losses observed. Simulations with different target thickness were conducted to investigate how the thickness might affect yields. The RF voltage was matched to replace the approximate energy lost through the target in a single pass, thus attempting to ensure a stable energy is achieved. Figure 6.4 shows the increased beam survival with decreased thickness, as would be expected. This works out such that the total average thickness of material traversed by the beam over all turns is approximately the same, ie. the yield is independent of target thickness. This is to be expected as the emittance around the machine should be constant, so the distance travelled around the machine between turns is effectively invisible as far as the scattering is concerned. The differences in total average thickness observed in these simulations can likely be attributed to differences in how well the beam, target and RF have been optimised together in each case.

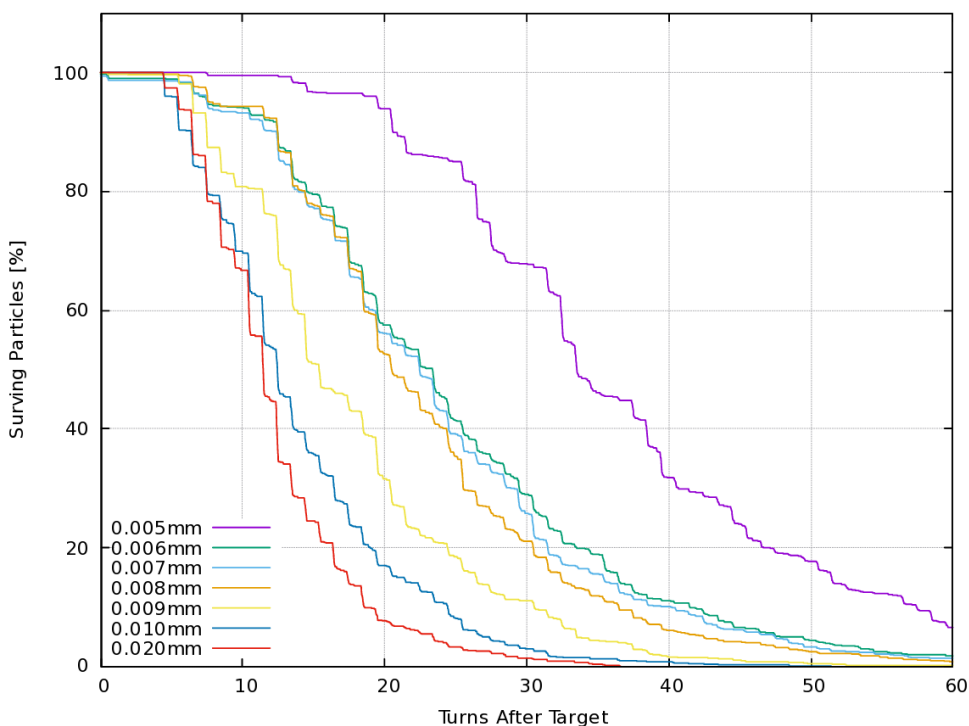


**Figure 6.4:** Effect of thickness on beam survival. Total distance traversed through target over all turns is independent of target thickness.

One area that would be expected to make a difference to beam survival is aperture

## 6. INTERNAL TARGET STUDIES

---

size. Figure 6.5 shows how the vertical aperture affects beam survival. The simulations were performed with a 0.005 mm target and various aperture sizes applied. Larger apertures result in longer beam survival, as expected. This shows that the dynamic aperture is large enough to allow for long beam survival, confirming that the physical aperture as opposed to the dynamic aperture is the limiting factor. In theory there is an equilibrium emittance where the ionisation cooling and the beam heating from scattering are balanced. When this emittance is reached the emittance growth will plateau. In this case however the physical aperture is much smaller than the equilibrium emittance and so the ionisation cooling effectiveness is limited.

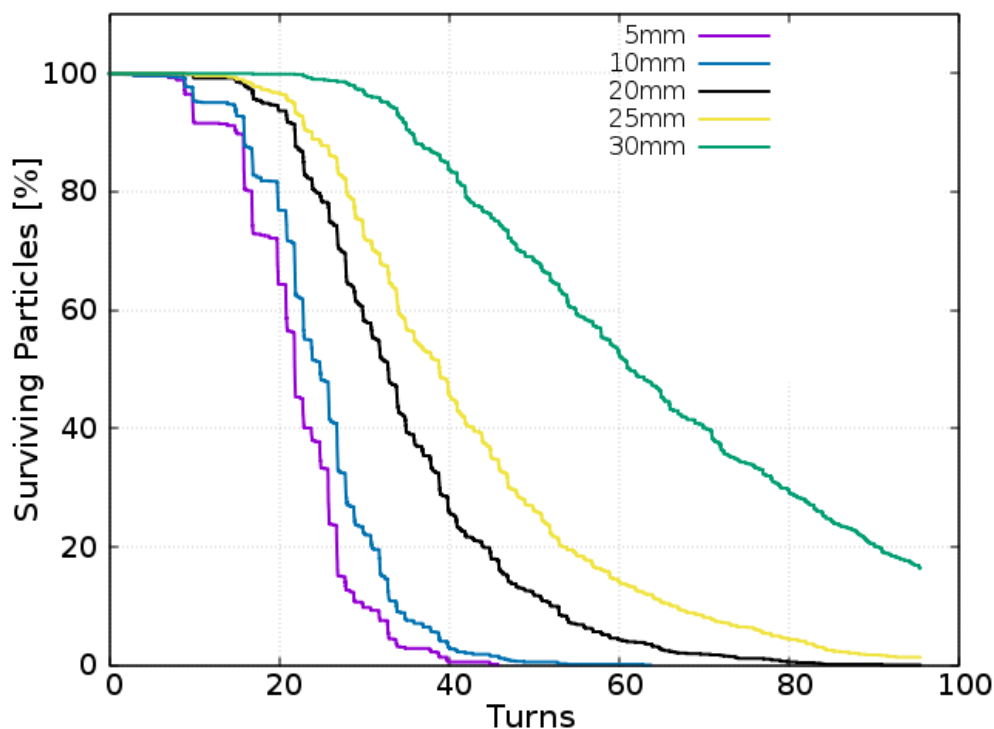


**Figure 6.5:** Effect of vertical aperture on beam survival. Increasing the aperture leads to significantly improved survival.

When observing the location of losses in these simulations a clear pattern emerges. For thicker targets such as 0.01 mm shown in fig. 6.6b the majority of the losses are in the sector immediately after the target. The particles are scattered through the target and their amplitudes rapidly become much larger than the physical aperture of the machine. As the target thickness is reduced the losses become more spread out around the machine as shown in fig 6.6a. This is because unlike for thicker targets the

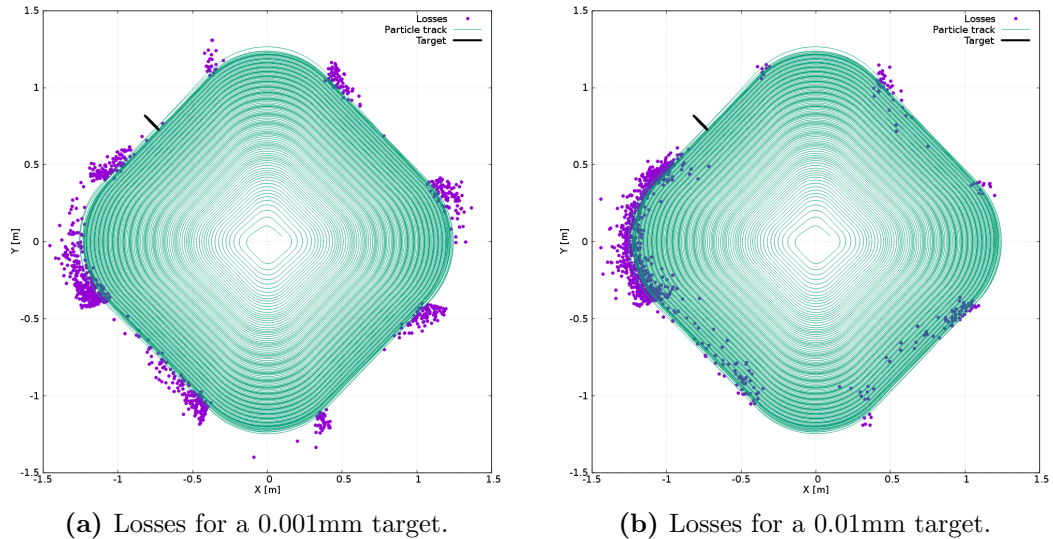


**Figure 6.6:** Location of losses in the machine from scattering through the target. Losses are concentrated in areas where the vertical beta function is large.

scattered particles' betatron amplitudes are only slightly larger than can be accepted and so the particles are not lost until they reach the peak of their betatron oscillations. Also noticeable is that the losses tend to occur at the magnet edges. This is because this is where the vertical beta function is at its highest and where particles will have their maximum vertical displacements. Consequently reducing the peak vertical beta function in future designs may help improve beam survival with an internal target.

In terms of managing beam loss the target thickness will affect the collimation design. With a thick target losses are concentrated in the sector after the target, and so a simple set up could be used with just a few collimators in this sector. Using a thinner target spreads the losses out around the machine more necessitating a more complicated set up with more individual collimators all the way around the machine. However each of these collimators will receive fewer particles, therefore reducing activation and cooling requirements.

### 6.3 Longitudinal Cooling

Although ionisation cooling helps dampen the emittance growth from scattering, the energy loss through the target is not uniform for all particles forming a distribution around the average. The RF cannot match exactly the energy loss for all particles and so there is an inevitable increase of the energy spread and hence an increase in the

## 6. INTERNAL TARGET STUDIES

---

longitudinal emittance. This contributes to losses either directly by particles falling out of the RF bucket, or indirectly through coupling from the longitudinal to the horizontal and vertical. A form of longitudinal cooling therefore could be of great benefit.

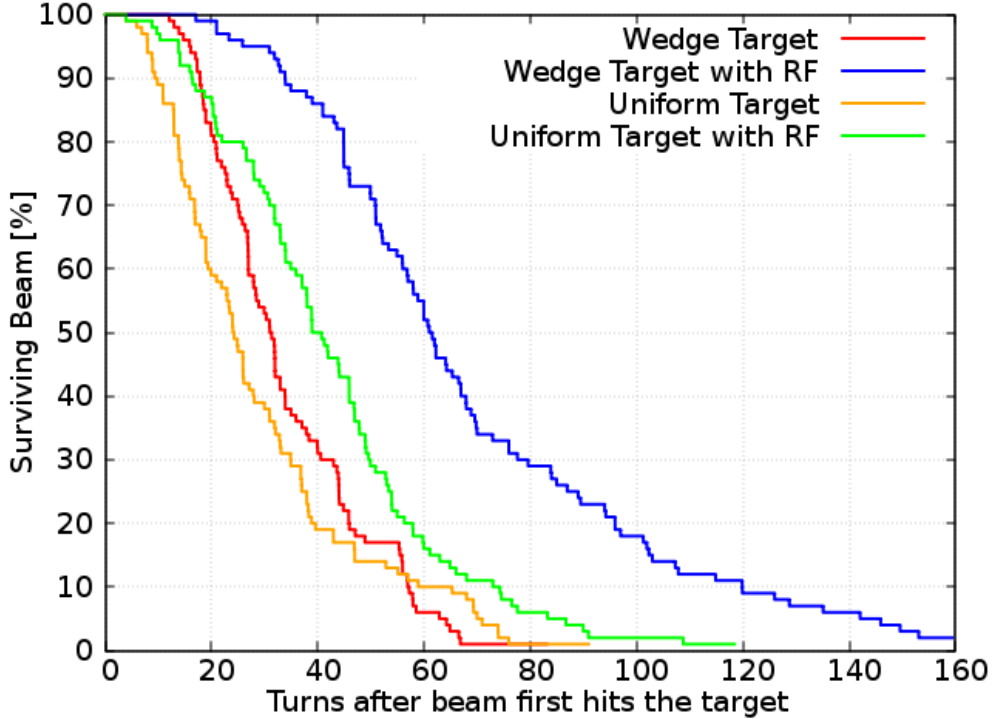
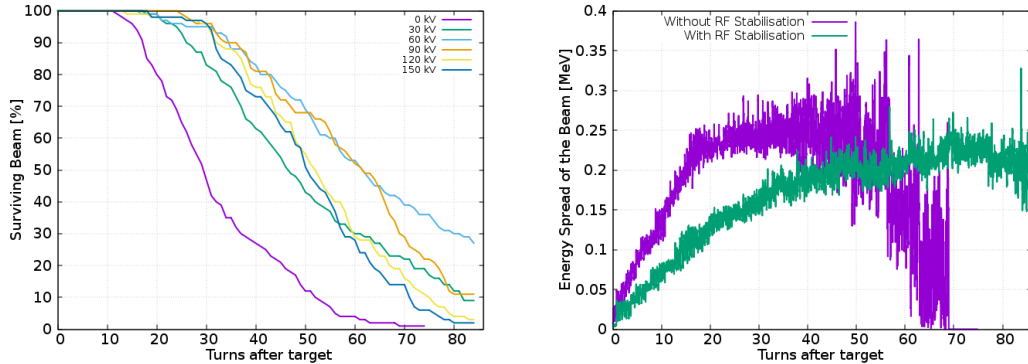


**Figure 6.7:** Comparison of loss control effectiveness between wedge target and RF stabilisation. The combined use of a wedge target and RF stabilisation gives a significant improvement over either one used on its own.

One way to introduce longitudinal cooling would be to use a wedge shaped target that gets thicker towards larger radii. In this way higher energy particles will travel through more material and lose more energy, while lower energy particles will lose less. This will have a cooling effect longitudinally. To simulate a wedge shaped target several thin targets were placed adjacent to each other in a staggered formation. Given that the target will need to be very thin and therefore likely made from foil this may also be a practical way of producing the wedge shape in a real machine.

Another way to control the longitudinal effects is to use an RF cavity, placed in the sector opposite the target and operating only at radii around that of the target. The phase should be set such that a particle that is at the perfect energy (i.e. 14 MeV) will arrive when the field is at 0, with higher energy particles arriving at negative



(a) Beam survival for differing RF voltages. (b) Effect of RF on energy spread of the beam.

**Figure 6.8:** Effect of RF stabilisation on beam survival and the energy spread of the beam. Maximum beam survival is found at 60kV and a significant reduction in the energy spread of the beam is observed.

voltages and lower energy particles at positive voltages. With the energy loss through the target and the energy gain from the main RF keeping the average energy constant, this additional RF acts to reduce the energy spread of the beam.

Figure 6.7 shows the effectiveness of these techniques at reducing the rate of beam loss. The use of a wedge shaped target gives a moderate increase in the integrated current on target, increasing it by  $\approx 20\%$  over a uniform thickness target. Using an RF cavity to stabilise the energy spread is more effective increasing integrated current  $\approx 50\%$ . The most effective result however came when using the RF cavity and wedge shaped cavity combined. With the RF and wedge combined an increase of up to  $140\%$  can be achieved. Figure 6.8b shows the energy spread of the beam for a wedge shaped target and a wedge target with RF energy stabilisation. The RF stabilisation results in a significantly reduced energy spread in comparison to the wedge alone. The apparent reduction in energy spread from the wedge target after approximately 50 turns through the target is driven by the loss of highly energy divergent particles, rather than a physical effect on the energy spread.

If the RF imparts or removes too much energy from the particles, i.e. more than is needed to bring them back to the average energy, then rather than reducing the energy spread it could increase it instead. As such there will be an ideal RF voltage where beam survival is maximized. Figure 6.8a shows the beam survival at different voltages. The ideal voltage in this case is around 60 kV, as if the voltage is increased higher than this the beam survival worsens.

In order to find the optimum settings in terms of phase and voltage for the RF cavity

## 6. INTERNAL TARGET STUDIES

---

a parameter sweep was performed calculating the integrated current on the target over the lifetime of the beam. The results of this sweep shown in fig 6.9 do not follow a perfect sinusoidal pattern as would be expected, given that the RF voltage varies sinusoidally. Instead whilst parts appear sinusoidal the areas around where the peak of a sine wave would occur are depressed. This effect is voltage dependent becoming more pronounced at higher voltages and may be caused by the interacting of the RF and the wedge target effect.

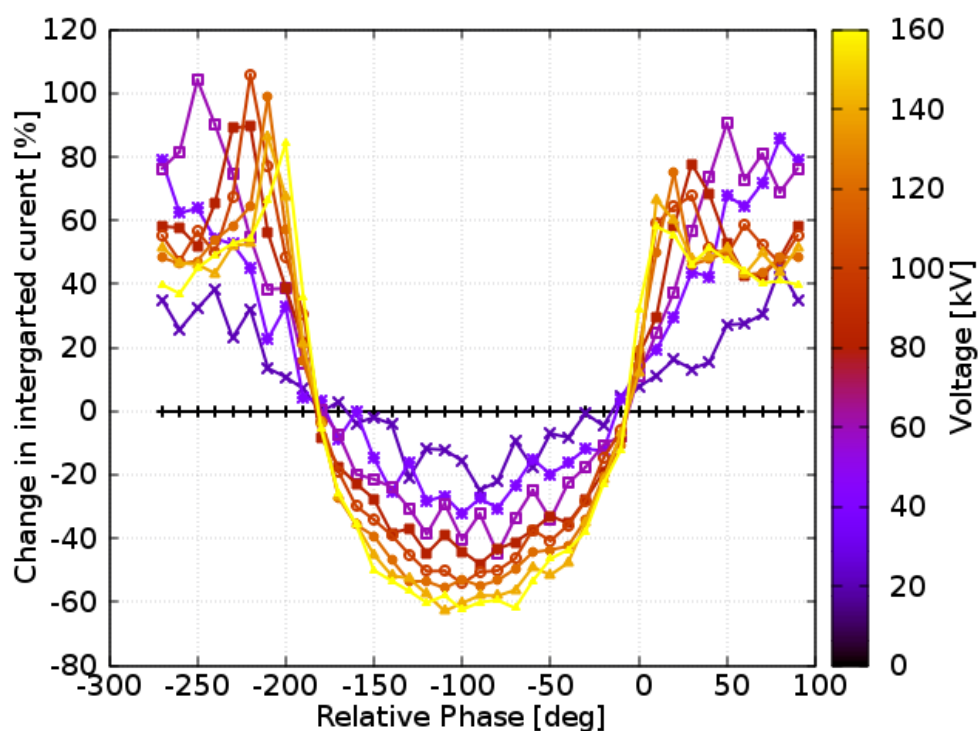


**Figure 6.9:** Effect on integrated beam current on target for different phases and voltages. The phase is relative to the phase of the main (accelerating) RF cavities.

### 6.4 Conclusions

The use of an internal target and recycled beam has already been demonstrated to be an effective way of increasing yields when used with a Beryllium target for neutron production. This is facilitated by ionisation cooling which helps counteract the emittance growth from scattering through the target. Ionisation cooling is most effective when using low Z target materials, hence the choice of a Beryllium target for neutrons. With

the production of  $^{99m}\text{Tc}$  in mind the challenge was to demonstrate that the ionisation cooling with a high  $Z$  material such as Molybdenum would be sufficiently effective to allow for long beam survival times.

The simulations undertaken show that ionisation cooling does have an effect, with a Molybdenum target allowing for around 35 turns before 50 % of the beam is lost (for a 0.005 mm target). This could produce a saturated yield of  $^{99m}\text{Tc}$  of up to 8 GBq/ $\mu\text{A}$ . This is comparable to what current commercial cyclotrons can achieve with thick targets, Andersson et. al. were able to use a ACS TR-24 to produce saturated yields of up to 5 GBq/ $\mu\text{A}$  of  $^{99m}\text{TcO}_4^-$  [136]. Although this is less than the internal target yield, the calculation for the internal target is theoretical and real world yields may be lower. As such further improvements are needed to prove that the system can outperform systems presently available and is worth pursuing further.

One key factor is the vertical aperture of the machine. Widening the aperture from  $\pm 2$  cm to  $\pm 3$  cm increases the beam survival from 35 to 60 turns, and so large apertures should be built into any future designs. The ERIT storage ring has a  $\pm 7.5$  cm pole gap, which is a major part of how it achieves up to 1000 turns through the target [62]. Another significant factor is control of the longitudinal dynamics of the beam. Ionisation cooling only cools in the transverse planes, but energy straggling causes emittance growth longitudinally. Two methods were investigated to introduce some degree of longitudinal cooling, a wedge shaped target and RF energy stabilisation. The wedge shaped target and RF stabilisation both gave moderate improvements to survival (20 % and 50 % respectively) but it was the combination of both together that had the most significant effect increasing the survival by 140 %. This translates into a theoretical saturated yield of  $^{99m}\text{Tc}$  of up to 18 GBq/ $\mu\text{A}$  which is significantly greater than the  $< 5$  GBq/ $\mu\text{A}$  that has so far been achieved with thick targets.

With the use of an internal target and recycled beam along with longitudinal cooling from a combination of wedge shaped target and RF stabilisation, a significant improvement can be made on present systems. This, with the high current capabilities of our design discussed in chapter 5, could make the performance of this machine extremely competitive in the cyclotron-produced radioisotopes market. Reworking the design to include large vertical apertures would lead to further improvements in beam survival and yields.

## 6. INTERNAL TARGET STUDIES

---

# 7

## Further Design Iterations

Simulations so far have shown that the machine is versatile (can accelerate both protons and  $\text{He}^{2+}$  ions), can deliver high current (up to 20 mA) and can work effectively with an internal target for the production of  $^{99m}\text{Tc}$ . Having established this performance potential, the focus moved toward possible improvements. Several areas were identified where improvements could be made to the design:

- The design is not zero chromatic with the tunes passing through several resonances at low energy.
- Although both protons and  $\text{He}^{2+}$  ions can be accelerated the field is not fully optimised to maximise dual particle performance.
- The design is larger than currently available commercial cyclotrons.

With these improvements in mind several new versions of the field map were created and investigated. The designs created are a Tune Adjusted Design, a Dual Proton/Alpha Design, a dedicated Alpha Design and a Compact 35 MeV Design.

For this design work the PyZgoubi [116] code was used, a brief description of which can be found in chapter 4.

### 7.1 Introducing an Effective Spiral Angle to Avoid Resonance Crossings

One of the limiting factors of the standard design discussed in chapters 4 through 6, are the machine tunes at low energy. They are suppressed by the magnet fringe fields, which at small radii fill the drift sectors reducing the flutter of the machine. To stabilise

## 7. FURTHER DESIGN ITERATIONS

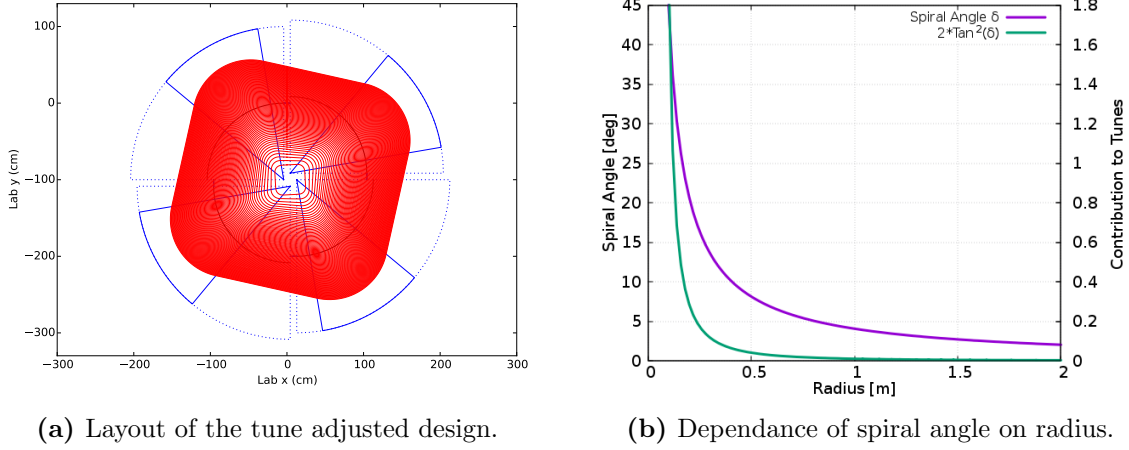


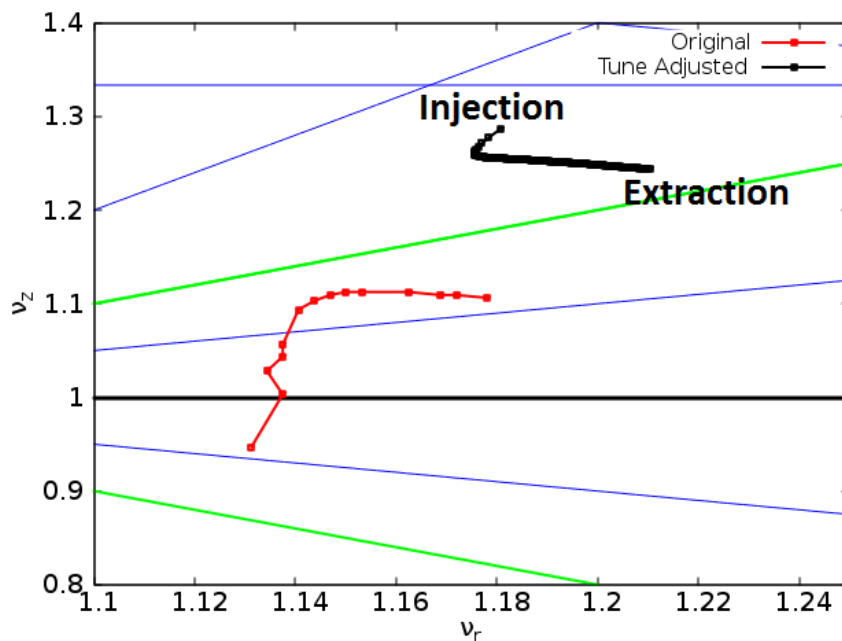
**Figure 7.1:** The new magnet configuration introduces a spiral angle ( $\delta$ ) into the design. The spiral angle is radius dependent and its contribution to the tunes go by  $2 \times \tan^2(\delta)$  creating an even steeper drop off in its effect with radius.

the tunes an additional form of focusing needs to be introduced. One focusing method not used so far in the design is a magnet spiral angle  $\delta$ , which is discussed in more detail in section 1.3.4. The angle at which the beam passes through the magnet edge has an effect on the focusing and by having a larger angle at the magnet entrance than at the exit an alternating gradient structure can be created[137]. Introducing a spiral angle at small radii therefore could stabilise the tunes at low energy. So far in this design however spiral sectors have not been used in order to keep the magnet design and construction as simple as possible. The challenge therefore was to introduce a spiral angle at small radii without spiraling the magnets.

The approach taken to achieving this was to shift the magnet positions such that the magnet centre line no longer points towards the centre of the machine but just passed it, instead pointing at the bottom of the next sector magnet as shown in fig 7.1a. Since the magnet centre line and the machine radius are no longer the same, an angle now exists between them, this is the spiral angle. This angle is dependent on the radius, rapidly reducing as it moves towards larger radii. The dependence of the spiral angle on radius is shown in fig 7.1b. The angle at a 10 cm radius (where the magnet starts) is  $45^\circ$  but drops to  $10^\circ$  by 40 cm. Furthermore equations 1.21 and 1.22 show that the contribution from the spiral angle to the machine tunes goes by  $2 \times \tan^2(\delta)$ , resulting in an even quicker drop in its effect with radius. This means that the additional focusing is only effective at low energy leaving the dynamics at larger radii and higher energies relatively unchanged. This is perfect for this machine as the biggest tune variation and

## 7.1 Introducing an Effective Spiral Angle to Avoid Resonance Crossings

resonance crossings occur only at low energy.



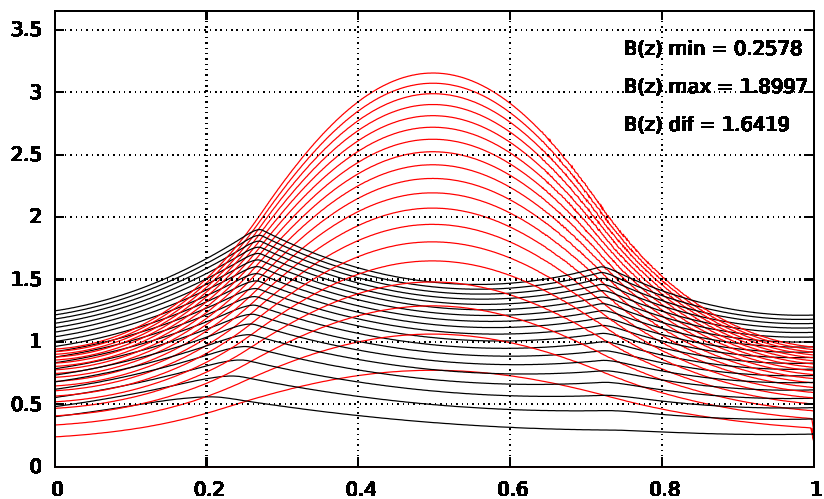
**Figure 7.2:** Comparison of tune maps for the original and tune modified designs. The modified tunes are higher and no longer pass through any resonances.

Figure 7.2 shows a comparison of the original and modified tunes. The new tune map now does not pass through any resonances (up to 3rd order) and shows significantly smaller variation in the vertical tune at low energies. At higher energies the pattern is similar to before, with a gradual increase in the horizontal tune with the field gradient. This was achieved by controlling the machine tunes using the technique of magnet displacement, and optimising it along with changes to the magnetic field gradient and magnet edge shape. This involved incrementally increasing the shift applied to the magnets until the vertical tune at low energy was raised to approximately the same level as at high energy. Although this technique has less effect at larger radii the tunes in this region are still raised slightly. Consequently part of the tune map became very close to the  $\nu_r = \nu_z$  resonance. To avoid this the magnetic field gradient was increased to raise the tune such that they are above the resonance. This new tune map should make the design more robust as there are no tune crossings to be excited by field errors or space charge effects.

This set up has other effects on the beam dynamics beyond the effect on the tunes. Figure 7.3 shows the horizontal and vertical beta functions over one cell, i.e. one quarter

## 7. FURTHER DESIGN ITERATIONS

---



**Figure 7.3:** Beta functions of the modified design. The new vertical beta function is not symmetric creating an alternating gradient structure.

of the ring. The horizontal beta function is very similar to that of the original design both in shape and amplitude, peaking in the centre of the magnet. The vertical beta function however does show some differences. The original beta function is symmetric but the modified function is not. The beta function at the magnet edges are different, with the entrance beta function higher than the exit beta function. The peak beta function at the magnet entrance, is higher than the peak beta function of the original design which may result in a slightly reduced dynamic aperture when vertical apertures are applied.

## **7.2 A Dual Particle Design Optimised for Both Protons and Alpha Particles**

Although the original design can run both protons and alpha particles it has not been optimised for running both, having been originally designed for protons. Consequently it works much more effectively for protons than  $\text{He}^{2+}$  ions. By producing a field map that is half way between the ideal for each particle it was hoped that a more versatile machine could be created.

For engineering reasons RF frequencies higher than the 7.159MHz fundamental revolution frequency are preferred. This is to make the cavities smaller/more efficient. The size of an RF cavity is related to its resonant frequency in that its longest side must be some fraction of the wavelength, and so higher frequencies lead to smaller cavities. The most common types of cyclotron cavities are either half ( $\lambda/2$ ) or a quarter ( $\lambda/4$ ) wavelength resonators. The fundamental frequency of this design gives a  $\lambda/2 = 21$  m. By using 4th harmonic the frequency is increased to 28.6 MHz and therefore  $\lambda/2 = 5.24$  m. Using a  $\lambda/4$  instead of a  $\lambda/2$  cavity reduces the cavity size by half. Unfortunately it also reduces the Q factor making it less efficient which makes it a less desirable option for a commercial machine [138].

To run at higher frequencies the machine would have to run at higher harmonics (4th harmonic or higher), which as discussed in chapter 4.2.6 is possible for protons but not for  $\text{He}^{2+}$  ions which can only use 1st or 2nd harmonics. A field map properly optimised for both could give better performance for alpha particles allowing it to run at higher harmonics, but would likely impact the proton performance negatively. Before trying to design a field map that maximises the performance for both, the performance of both protons and alpha particles was characterised for field maps optimised for each respectively. This was done so that direct comparisons could be made and the degree to which the performances have been compromised quantified.

For a given frequency whichever harmonic the machine is operating in for protons will be doubled for alpha particles as they have a time of flight of approximately half that of protons. This means that if protons are operating at the 4th harmonic then alpha particles will be at the 8th. For this design an accelerating gradient of 400kV/turn was used. Figures 7.4a and 7.4b show the RF space for a field map optimised for protons when running protons on the 4th harmonic and  $\text{He}^{2+}$  ions on the 8th. The protons experience only a small amount of phase slip allowing for a large phase acceptance of around  $90^\circ$ . The  $\text{He}^{2+}$  ions however experience a huge phase slip and fall out of the accelerating phase before reaching 5 MeV. In figures 7.4c and 7.4d the RF phase spaces

## 7. FURTHER DESIGN ITERATIONS

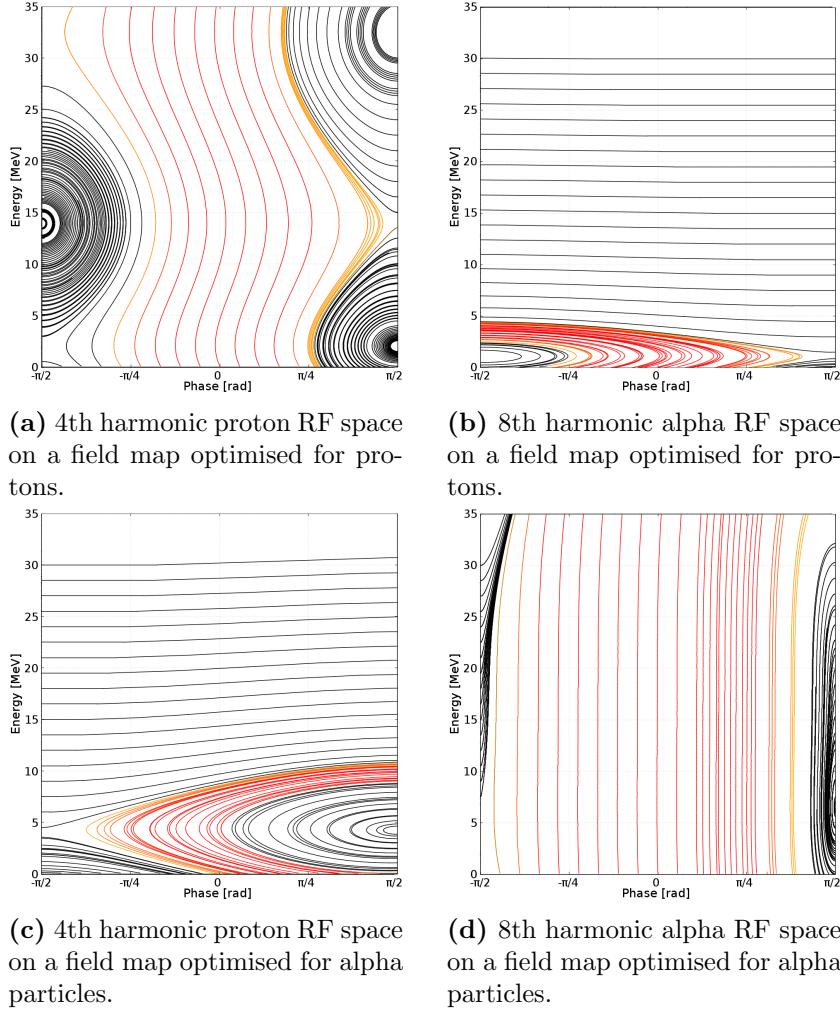


**Figure 7.4:** RF spaces for protons and alpha particles on field maps optimised for each particle respectively.

for a field map optimised for  $\text{He}^{2+}$  are shown. The  $\text{He}^{2+}$  phase slip is very small and has a very large acceptance of around  $150^\circ$ . In the proton phase space the particles can only reach a maximum energy of 10 MeV due to the large phase slip. The protons perform better on the  $\text{He}^{2+}$  field map than vice versa because the  $\text{He}^{2+}$  ions are operating at double the proton harmonic, experience double the phase slip and therefore can only reach half the energy.

Now that the performance of field maps optimised for protons and  $\text{He}^{2+}$  ions has been established, it is clear that neither can run the other particle at as high a harmonic as is desired. Next a new field map was created with a magnetic field gradient

## 7.2 A Dual Particle Design Optimised for Both Protons and Alpha Particles

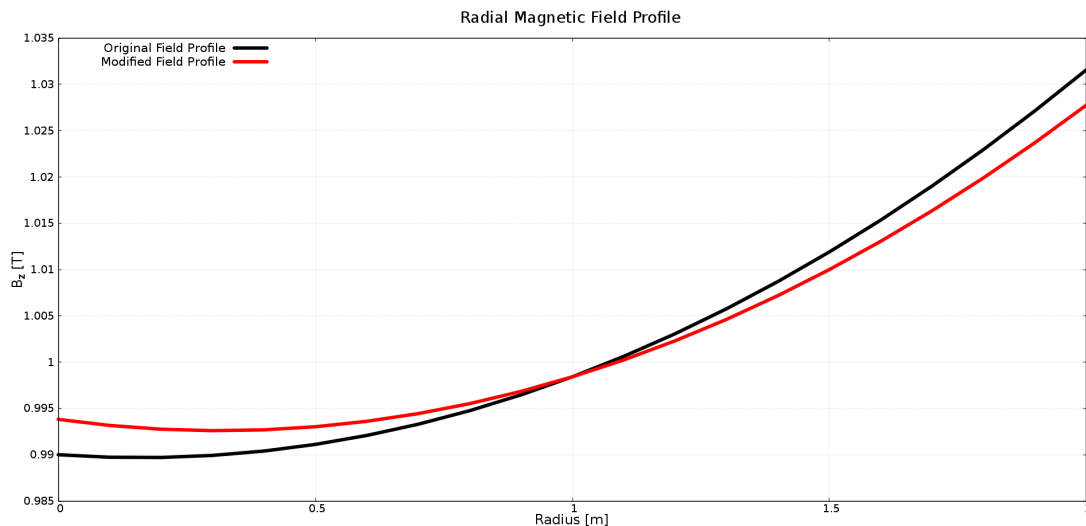


**Figure 7.5:** Comparison of the magnetic field of the new dual proton/alpha design with the original. The new field varies from the original by no more than  $\pm 0.005$  T.

somewhere in between that of the proton and the  $\text{He}^{2+}$  field maps. Figure 7.5 is a comparison of this new field map and the original field map. The adjustment is fairly small now being approximately 0.005 T higher at the start of the magnet and approximately 0.005 T lower at the outer edge.

When the RF phase space of the new field map is investigated, it is seen that the performance of both protons and  $\text{He}^{2+}$  ions is improved over when they are run on the “wrong” field map. Unfortunately despite this improvement they are still unable to reach 28 MeV when running at the 4th and 8th harmonic for protons and  $\text{He}^{2+}$  ions respectively. Figure 7.8 shows the RF phase spaces of the 1st and 3rd harmonics for both particles. At the 1st harmonic the phase acceptance for both particles is reduced compared to their ideal field maps, but is still relatively large at around  $80^\circ$  for alpha particles and approximately  $65^\circ$  for protons. By the 3rd harmonic the phase space has become much more restricted for both particles with only a very small accelerating channel available leaving a very small phase acceptance.

Although this design was not able to reach the performance requirement that was desired, it has led to improvements over the original in that it has made the performance for protons and  $\text{He}^{2+}$  ions the same. From this base field there are techniques that may be able to modify the field to suit whichever particle is being run at the time.

The field map being half way between the ideal magnetic field gradients for each

## 7. FURTHER DESIGN ITERATIONS

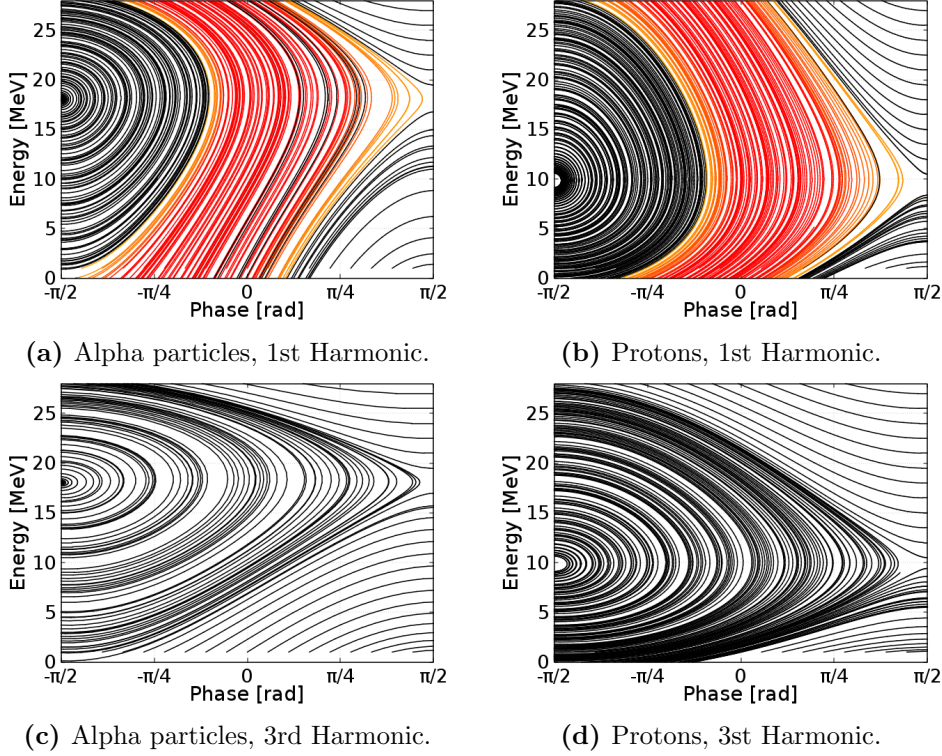


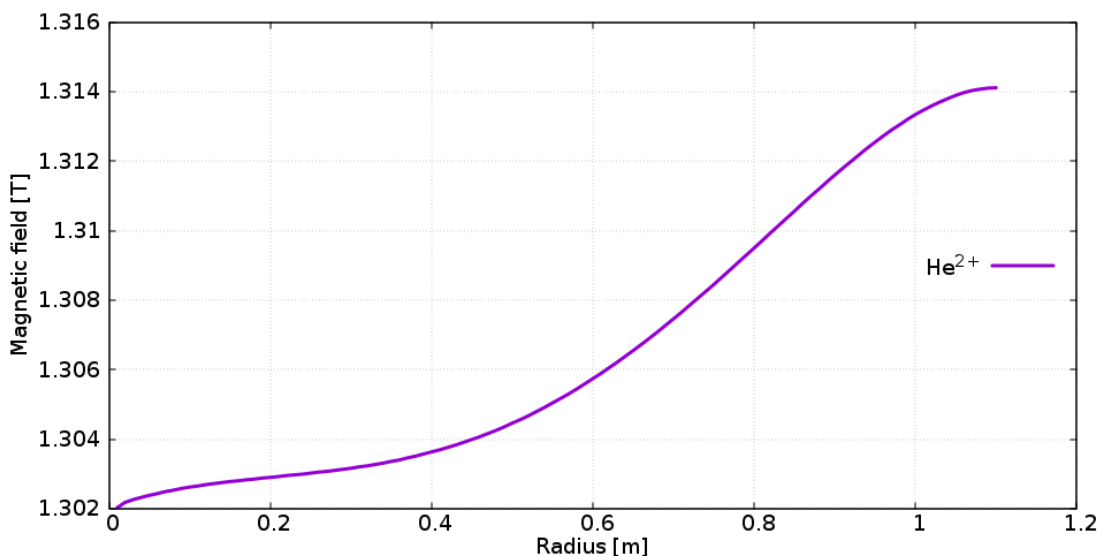
**Figure 7.6:** RF space for protons and alpha particles at the 1st and 3rd harmonics. The acceleration channel to 28 MeV is lost at higher harmonics.

particle could possibly be modified for running either protons or  $\text{He}^{2+}$  ions using trim coils, thus improving the performance of both. The required field gradient changes are a maximum of  $\pm 0.005$  T. Field changes of this magnitude have been achieved with trim coils in operating cyclotrons [139] so trim coils may be able to modify the field sufficiently to allow efficient acceleration of either protons or  $\text{He}^{2+}$  ions.

Another possible method of field modification is interchangeable magnetic shims. Magnetic shimming [140] is standard practice in cyclotron manufacturing to obtain the desired field accuracy. By creating two different interchangeable shims, one for each particle, the field can be modified to suit the desired particle[141]. The down side to this approach is that switching between particles would require the physical replacement of the shims which would be quite time consuming, during which the machine could not be run.

### 7.3 A Field Map Optimised for Alpha Particles

If a field map cannot be made that will accelerate both protons and  $\text{He}^{2+}$  ions at higher harmonics, then a dedicated  $\text{He}^{2+}$  machine may be worth investigating as there are many radioisotopes that require  $\text{He}^{2+}$  for production. A field map was therefore created by Carol Johnstone<sup>1</sup> using COSY specifically for  $\text{He}^{2+}$  acceleration.



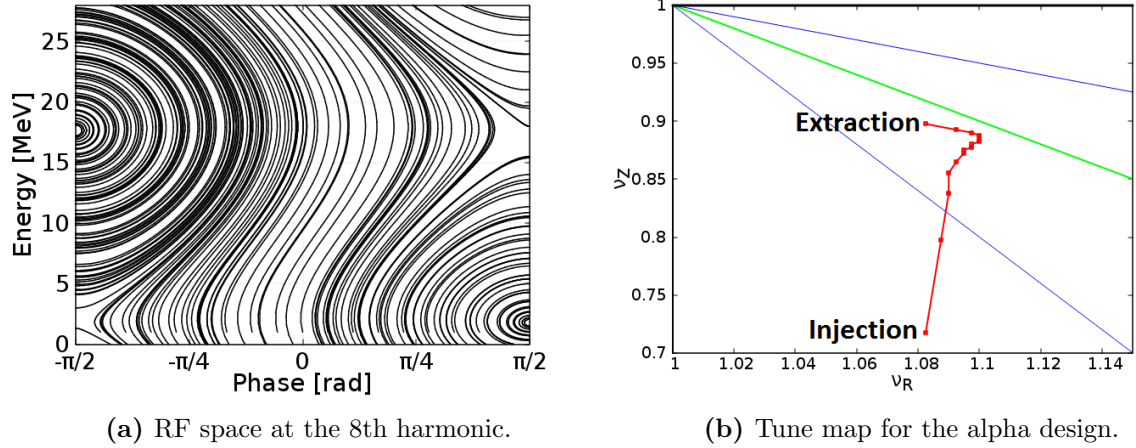
**Figure 7.7:** Magnetic field for the dedicated  $\text{He}^{2+}$  design.

Figure 7.7 show the new magnetic field gradient. The dipole field component is slightly higher than in the original design at 1.302 T making the machine more compact. The field rises by 0.012 T by the extraction radius with a final field at 1.314 T. This new gradient is much shallower than the original, reflecting that the  $\text{He}^{2+}$  ions are significantly less relativistic than protons. This results in a very isochronous field with acceleration at the 8th harmonic and above achievable. Figure 7.8a shows the RF space for  $\text{He}^{2+}$  ions at the 8th harmonic. In the original design  $\text{He}^{2+}$  ions could only use the 1st and 2nd harmonics, here they are able to be accelerated on the 8th with a phase acceptance of around  $100^\circ$ .

The tunes for this field map shown in fig 7.8b, are significantly different from those of previous versions. The horizontal tunes are quite stable, increasing slightly up to 27 MeV before dropping off toward the final energy. This pattern follows that of the magnetic field gradient shown in fig 7.7, which has the largest contribution to horizontal

<sup>1</sup>Senior Accelerator Physicist, Fermi National Accelerator Laboratory, Batavia, IL, USA

## 7. FURTHER DESIGN ITERATIONS



**Figure 7.8:** RF space at the 8th harmonic and tune map for the dedicated alpha field map. The phase acceptance is now around  $100^\circ$  compared to the original that could not accelerated at all on the 8th harmonic. The vertical tune is now lower than in the original design and no longer crosses an integer resonance.

tune. In the vertical plane the tune rises by 0.18 from injection to extraction. This increase takes the tunes through the  $2\nu_r - \nu_z = 3$  resonance and at higher energies close to the  $\nu_r + \nu_z = 2$  resonance. Overall the vertical tune is significantly smaller than in the first design. This is a result of the widening of the magnets from approximately  $40^\circ$  to  $48^\circ$ , which reduces the flutter thus lowering the tune. One noticeable difference from the original design is that the tunes do not cross the  $\nu_z = 1$  integer resonance which should make the machine more resistant to field and alignment errors.

### 7.4 Compact 35 MeV Design

There are many different costs associated with buying and operating an accelerator for radioisotope production. For a commercial accelerator these must be minimised in order to make the venture viable. One of the biggest costs is the associated infrastructure costs. For radiation protection cyclotrons have to be housed in a concrete bunker, which is a significant additional cost if there is not a bunker already in place. Self-shielding cyclotrons are available but these do not negate the need for a bunker completely, allowing for the use of thinner concrete walls [142]. Self shielding designs are also limited to smaller lower energy cyclotrons as the shielding requirements increase significantly with higher energies. Consequently there is significant incentive to produce as small a cyclotron as possible to save on the cost of the bunker.

The magnetic field of the standard design is 0.99 T at injection rising to 1.03 T at

extraction. The magnetic saturation point of steel is around 2.1 T which limits the field that can be produced. Higher fields could therefore be used to reduce the circumference of the machine. The higher fields will require larger magnet yokes so although the radius of the machine will be reduced its height will be increased. Superconducting magnets could be utilised to further increase the field and reduces the size of the machine. However the additional cost and complexity of a superconducting design outweighs any benefits so fields higher than 2.1 T were not considered.

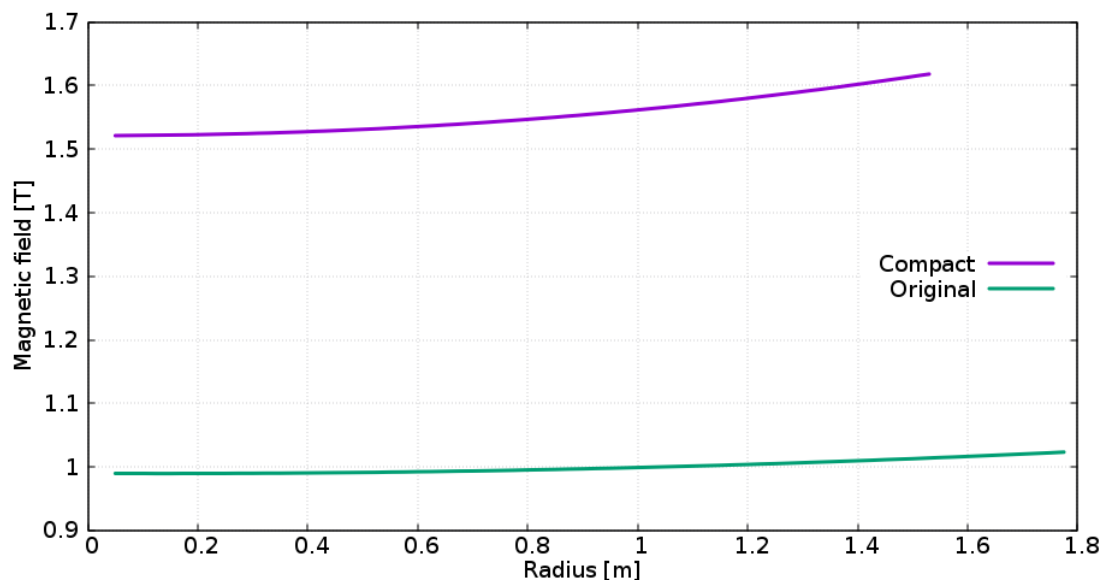


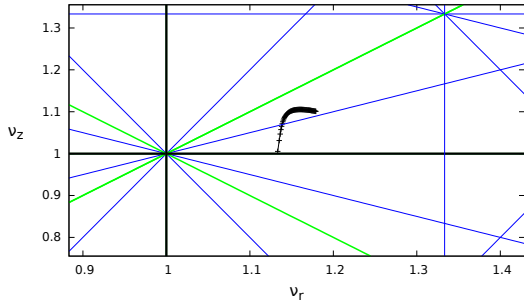
**Figure 7.9:** Comparison of the magnetic fields of the Compact 35 MeV design and the original.

A higher magnetic field version of the design was created to make the machine more compact. It was decided to extend the energy range to 35 MeV to include further possible isotopes. Figure 7.9 shows the difference in magnetic field gradients between the new field map and the original. The new field is 1.521 T at injection and 1.618 T at extraction. The field is lower than the 2.1 T limit in order to keep the magnet design simple by avoiding complications that arise as the iron approaches saturation.

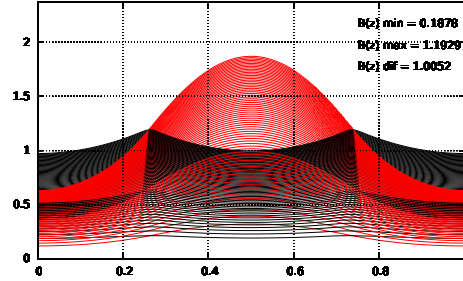
The tune map shown in fig 7.10a is very similar to the original design. Injection is very close to the  $\nu_z = 1$  resonance and it then passes through a third order resonance before stabilising. The injection point being so near an integer resonance may be problematic and the design may need to be tweaked, either by adjusting the magnetic field to raise the vertical tune or by injecting at a different energy. After injection the tunes quickly move away from the resonance so the growth of any instabilities is

## 7. FURTHER DESIGN ITERATIONS

limited.



(a) Tune map for the compact 35 MeV design.



(b) Horizontal (red) and vertical (black) beta functions of the compact 35 MeV design.

**Figure 7.10:** The tunes and beta functions for the new design. Both are very similar to those of the original design. The beta functions are a little smaller due to the higher magnetic fields.

The performance of the design under strong space charge forces was very good. Figure 7.11 shows the transverse and longitudinal emittances at increasing beam currents up to 14 mA at the 1st harmonic. The same pattern of initial growth and then stabilisation of the emittances is observed as in the original design. The final emittances however are lower than seen in the original design. A significant part of this is due to a higher accelerating gradient being used. As the design is more compact it was anticipated that turn separation would be more of an issue than with the original design, so the accelerating gradient was increased from 200 kV/turn to 400 kV/turn. The faster acceleration allows less time for the space charge forces to effect the beam and so lowers the emittance. Another contributing factor to the lower emittances is the smaller phase slip of this design, which means that the bunch uses a smaller section of RF space. This results in a smaller energy spread in the beam and can have a significant effect on the transverse emittances. The higher magnetic fields also produce smaller Beta functions, shown in fig 7.10b, compared to the standard design. This also contributes to the lower emittances.

Going to higher harmonics can be beneficial to high current performance. This works by having multiple bunches on each orbit each with a smaller amount of charge, and is discussed in more detail in in chapter 5. For the original design the ideal harmonic to run at was the 2nd or 3rd. Figure 7.12 shows the effect of the harmonic number in the new design for 14 mA of beam current. Which harmonic is most effective depends on the shape of the beam. Figure 7.12a is for a 2/2/2 mm spherical bunch and the

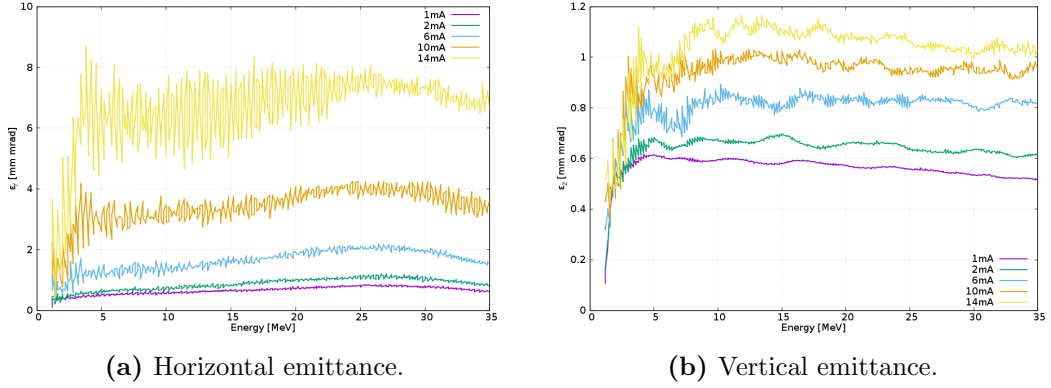


**Figure 7.11:** Radial and vertical emittances for increasing beam current at 1st harmonic.

emittance reduces as the harmonic increases to the 8th. This is a result of the smaller phase slip of this design and the small longitudinal size of the beam, which means that the entire bunch remains close to the RF crest throughout acceleration. This minimises growth in the energy spread of the beam. Higher harmonics would be needed before the energy spread of the beam starts to increase significantly. Figure 7.12b shows the same simulations but for an elongated 2/5/2 mm bunch. The longer beam results in lower emittances at lower harmonics as the space charge is more spread out. At higher harmonics (6 and above) it can be seen that the phase slip and long bunch means that the energy spread increases which causes growth in the horizontal emittance. As such the length of the bunch should be adjusted depending on which harmonic the machine is operating at.

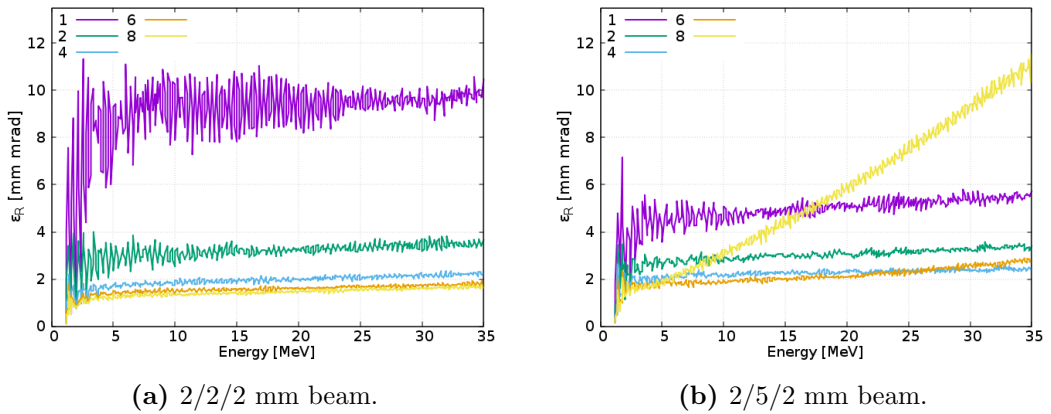


**Figure 7.12:** Effect of harmonic number on radial emittance for different beam lengths.

With higher magnetic fields and a smaller radius than before, the orbit separation

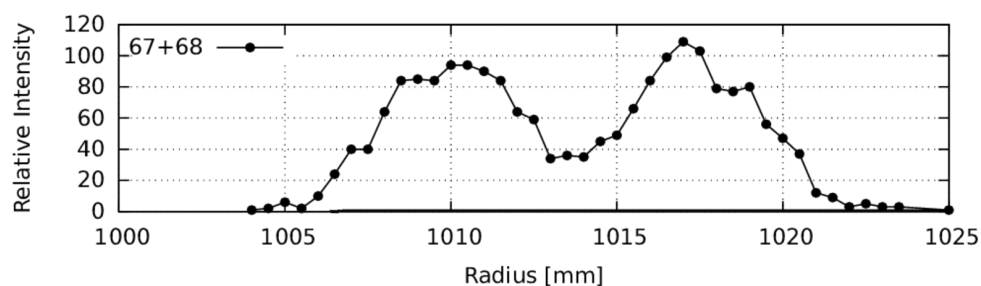
## 7. FURTHER DESIGN ITERATIONS

---

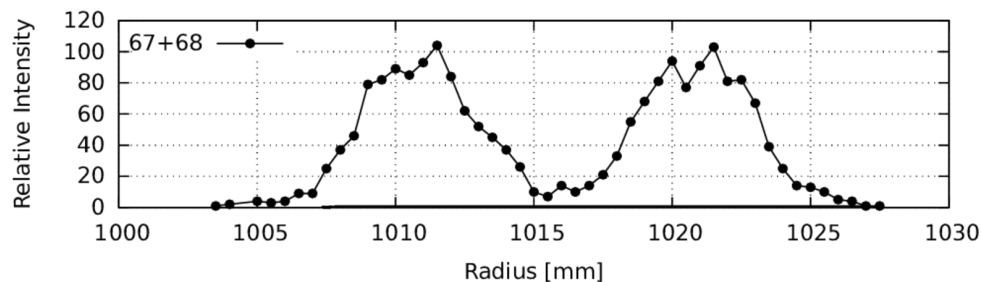
will be significantly reduced. This makes extraction more difficult as there needs to be a clear gap between bunches on adjacent orbits in order to extract cleanly. At high currents the problem is even greater as space charge forces induce beam widening.

Figure 7.13a shows the beam profile in the final two turns before extraction for 1 mA of beam current. There is significant overlap of these final two orbits, with the intensity dropping to only 35 % of the peak intensity between the orbits. Consequently the losses on an extraction septum would be significant and could cause both heating and activation issues.

One method of improving the orbit separation is to induce a coherent oscillation of the bunch around the accelerated orbit [24]. Figure 7.13b show the final two turns under the same conditions as in fig 7.13a but with a coherent oscillation induced by displacing the beam at injection. The intensity between orbits now drops to < 5 % of the peak. This improved separation allows for a much cleaner extraction, especially if combined with a collimation set up to reduce the size of the beam halo and tail.



(a) No coherent oscillations.



(b) With coherent oscillations.

**Figure 7.13:** Beam profiles for the last 2 turns under normal conditions and when a coherent oscillation has been induced. The orbit separation is significantly improved by the oscillations, easing extraction.

## 7.5 Conclusions

The new variations of the design were created to address some of the potential weaknesses of the original design.

The tune adjusted design was created to avoid the resonance crossings in the original field map. This was achieved by introducing a spiral angle to the design by shifting the magnets off centre. This effect is radially dependent so only affects the tunes at low energy. The resulting tune map does not cross any resonances up to the 3rd order. A downside to this design is that the new vertical beta function is slightly larger than before.

The dual proton/alpha design aimed to improve the performance for  $\text{He}^{2+}$  ions, while compromising the proton performance as little as possible. It was established that neither particle could run effectively on a field map optimised for the other. A new field map was created with a magnetic field gradient half way between the ideal fields for each particle. This new design resulted in similar performance for both protons and  $\text{He}^{2+}$ . Both particles could be accelerated to 28 MeV when using the 3rd harmonic or below. The phase acceptance at the 3rd harmonic however was very small and not practical for real operation. Both particles therefore were well short of running on the desired harmonic (4th for protons and 8th for  $\text{He}^{2+}$  ions). Other methods such as trim coils and interchangeable shims could allow the target harmonics to be attained.

A dedicated  $\text{He}^{2+}$  design was created, as it should be able to provide superior performance for  $\text{He}^{2+}$  ions compared to a dual particle design. The design features higher magnetic fields and wider magnets than the original field map. This results in a more compact machine. The design is easily able to accelerate on the desired 8th harmonic with a phase acceptance of around  $100^\circ$ . The wider magnets result in a lower vertical tune meaning that it no longer passes through the  $\nu_z = 1$  resonance.

The compact 35 MeV design was created to address the fact that the original design is not as compact as most of the commercial machines available [104], whilst also increasing the energy range to cover further radioisotopes. The magnetic fields are 0.5-0.6 T higher than the original, reducing the radius of the machine from 1.8 m (at 28 MeV) to 1.2 m (at 35 MeV). The tunes and beta functions are very similar to the original. The main difference being that the beta functions are lower due to the higher fields.

These designs have successfully addressed many of the weaknesses of the original design such as resonance crossings,  $\text{He}^{2+}$  acceleration and compactness of the design. Future work should try to combine some of these features to raise the all round perfor-

## **7. FURTHER DESIGN ITERATIONS**

---

mance of the design.

## 8

# Summary and Conclusions

Although the first FFAG designs were developed in the 1950's it is only recently that their potential is beginning to be realised. The difficulties in the design and manufacturing of complex magnetic fields, that held back early development, have been overcome with modern computer aided design and manufacturing techniques. This has opened up a new era of interest in FFAGs and designs have been made for a wide range of applications.

One area where FFAGs could be applied is for radioisotope production. High currents are needed to produce large enough yields to make production commercially viable. FFAGs are well suited for this as they have large dynamic apertures and so can handle the emittance growth from space charge effects. The market for radioisotopes is growing, particularly for medical application where they are used for both imaging and treatment. Many medical radioisotopes are accelerator produced including the main PET isotopes of  $^{18}\text{F}$  and  $^{11}\text{C}$ . There is also interest in new isotopes such as  $^{211}\text{At}$  which could be produced with a particle accelerator.  $^{99m}\text{Tc}$  which is used in over 80% of imaging procedures is currently produced in research reactors but a desire to diversify the supply chain has brought renewed interest in direct accelerator production.

In this thesis a design of a compact non-linear non-scaling FFAG has been presented. The imagined application of the design is for the production of radioisotopes, and in particular the production of  $^{99m}\text{Tc}$  and  $^{211}\text{At}$ .  $^{99m}\text{Tc}$  requires 14-20 MeV protons while  $^{211}\text{At}$  needs 28 MeV alpha particles. As such the energy range of the machine is from 75 keV to 28 MeV and the use of both protons and alpha particles has been investigated. The basic design consists of four separate radial sector magnets and two RF cavities. The magnetic field is defined by a polynomial and is optimised with the edge angle to maintain isochronicity and stabilise the tunes.

## 8. SUMMARY AND CONCLUSIONS

---

Simulations were carried out using the OPAL code to characterise the machines performance. The maximum time of flight variation across the energy range is  $\pm 0.15\%$  and the integrated variation  $0.632\%$ . This is sufficiently isochronous to allow for fixed frequency RF and CW operation. The betatron tunes are stable at median to high energy with just a small increase in the horizontal tune and no resonances (up to 3rd order) crossed. At low energy the fringe fields begin to overlap causing a depression of the vertical tune which results in the crossing of several resonances including an integer resonance. The dynamic apertures were found to be large peaking at around 12.5 MeV in the horizontal plane with  $150 \pi \text{ m mrad}$  and at 24 MeV in the vertical at  $41.4 \pi \text{ m mrad}$ .

Investigation of the RF phase space showed that an acceleration channel to 28 MeV opens up at 20 kV/turn when using the 1st harmonic. With a 100 kV/turn acceleration is achievable up to the 5th harmonic. There is significant coupling from the longitudinal to transverse planes due to the effect of the longitudinal emittance on the energy spread of the beam. The accelerating voltage also affects the energy spread of the beam as well as the crossing rate of any resonances. Consequently increasing voltages result in lower emittances.

Simulation of alpha particles using the same magnetic field revealed that tunes and dynamic apertures are very similar to those of protons. The RF phase space however is significantly more restricted. Only the 1st harmonic is usable unless very large accelerating gradients are used. The emittances are significantly larger than for protons, due largely to the greater phase slip and resulting increased energy spread of the beam.

An investigation of the effect of field errors on the dynamic aperture of the machine showed that it is quite resistant to them, requiring large field errors before a significant reduction in the dynamic aperture is observed.

Simulation of space charge effects revealed that the design is capable of accelerating high currents for both protons and alpha particles. Protons can be accelerated with up to 4mA beam current with no losses and at 20mA with 2.3% beam losses. Alpha particles can be accelerated with minimal losses with up to  $800 \mu\text{A}$ . For protons it was found that using the 2nd or 3rd harmonic gave the best results under high current conditions. The design compares well with currently available commercial cyclotrons which are capable of delivering  $400 \mu\text{A}$  to 1.2 mA of beam current for protons, and up to  $50 \mu\text{A}$  for alpha particles.

An internal target and recycled beam was investigated to see if it could improve  $^{99m}\text{Tc}$  yield compared to a thick target set up. Simulations show that even when using

a high  $Z$  material such as  $^{100}\text{Mo}$ , ionisation cooling still has an effect, helping cool the beam emittances. With a 0.005 mm target the beam intensity is reduced by 50% in 35 turns. The vertical aperture has a significant impact on the beam survival, with a 1 cm increase in the half aperture almost doubling the beam survival time. The other main influence on beam survival comes from minimising the longitudinal emittance growth. Two techniques were used to cool the beam longitudinally, a wedge shaped target and an additional RF cavity placed at the target radius. The wedge shaped target improved beam survival by 20% and the RF stabilisation improved it by 50%. When both techniques are implemented simultaneously the effect was amplified and an improvement of 140% was observed. With these improvements a theoretical yield of up to 18 GBq/ $\mu\text{A}$  could be achieved. This would represent a significant improvement on current thick target yield that can produce up to 5 GBq/ $\mu\text{A}$ .

Several variations of the design were created to investigate potential improvements. A tune adjusted design created a spiral angle in the machine by shifting the magnets off centre. The effect is radially dependent, reducing at larger radii, and so was effective at compensating for the natural tune suppression at low energy from fringe field overlap.

A design with a magnetic field half way between the ideal fields for protons and alpha particles was used to investigate the feasibility of running both particles with the same machine. The maximum usable harmonic for both protons and alpha particles was the 3rd, some way short of the desired 4th and 8th harmonics. As the dual particle approach did not meet the desired performance a dedicated alpha particle machine was designed. With the field map optimised for alpha particles, operation at the 8th harmonic was easily achieved with a phase acceptance of approximately  $100^\circ$ .

A more compact higher energy design was also created. The peak magnetic field was increased to 1.6 T which resulted in an extraction radius of 1.2m at 35 MeV. The tunes are very similar to the original design and the beta function has the same shape but is smaller due to the higher fields. Under high current conditions the design performs very well with lower emittances than the original design, for the same beam current.

## 8.1 Future Work

Further work is needed to maximise the potential of this design. At low energies there are several resonance crossings and this is where the dynamic aperture is most restricted and the majority of losses occur under high currents. Better control of the tunes in this area is therefore needed. The tune adjusted design needs to be simulated with space charge effects and field errors to assess if it is a suitable approach.

## 8. SUMMARY AND CONCLUSIONS

---

To improve the performance of the internal target the design should be modified to reduce the beta functions as this will reduce the emittance growth from scattering. Additionally widening the vertical aperture would greatly increase beam survival, but would also increase the size of the fringe fields. The feasibility of this should be investigated as should the use of field clamps to contain the stray field.

### 8.2 Conclusions

Overall the design performs well for protons with acceleration at up to the 6th harmonic achievable and with currents of up to 20 mA. This high current capability, if combined with an internal target, could produce  $^{99m}\text{Tc}$  yields significantly larger than currently possible. The improvement could be even greater for isotopes with sharp cross-section peaks and lower  $Z$  target materials. As the lattice was not designed for alpha particles their performance is not as optimised as for protons, but acceleration at the 1st harmonic is still possible potentially increasing the machines versatility. With further development this design could offer genuine advantages over current commercial cyclotrons for radioisotope production.

# References

- [1] E WILSON. *An introduction to particle accelerators*. Clarendon Press, 2001.
- [2] K WILLE. *The physics of particle accelerators: an introduction*. Clarendon Press, 2000.
- [3] KLAUS G STEFFEN. **High Energy Beam Optics**. *American Journal of Physics*, **34**(11):1071–1071, 1966.
- [4] H WIEDEMANN ET AL. *Particle accelerator physics*, **314**. Springer, 2007.
- [5] RJ VAN DE GRAAFF. **A 1,500,000 volt electrostatic generator**. *Phys. Rev*, **38**:1919, 1931.
- [6] TW AITKEN, BS HALLIDAY, WT JOHNSTONE, CW JONES, T JOY, MC MORRIS, NRS TAIT, AND RGP VOSS. **The nuclear structure facility at Daresbury**. *Nuclear Instruments and Methods*, **122**:235–265, 1974.
- [7] JD COCKCROFT AND ETS WALTON. **Experiments with high velocity positive ions. I.-Further Developments in the Method of Obtaining High Velocity Positive Ions**. *Proceedings of the royal society of London. Series A*, **136**:619–630, 1932.
- [8] RJ VAN DE GRAAFF. **Tandem electrostatic accelerators**. *Nuclear Instruments and Methods*, **8**(2):195–202, 1960.
- [9] A CLIMENT-FONT, F PÁSZTI, G GARCIA, MT FERNÁNDEZ-JIMÉNEZ, AND F AGULLÓ. **First measurements with the Madrid 5 MV tandem accelerator**. *Nuclear Instruments and Methods in Physics Research Section B: Beam Interactions with Materials and Atoms*, **219**:400–404, 2004.
- [10] PH ROSE AND AB WITTKOWER. **Tandem Van de Graaff accelerators**. *Scientific American*, **223**(2):24–33, 1970.

## REFERENCES

---

- [11] E RIMINI. *Ion implantation: basics to device fabrication*, **293**. Springer Science & Business Media, 2013.
- [12] X DING AND S BOUCHER. **A Method for Establishing Q-factors of RF Cavities**. In *Proceeding of the 1st International Particle Accelerator Conference: Kyoto, Japan*. JACoW, 2010.
- [13] ML GOOD. **Linear accelerator**, November 13 1956. US Patent 2,770,755.
- [14] EO LAWRENCE AND M. STANLEY LIVINGSTON. **The Production of High Speed Light Ions without the use of High Voltages**. *Physical Review*, **40**(1):19, 1932.
- [15] SY LEE. *Accelerator Physics*. World Scientific, 2004.
- [16] EO LAWRENCE. **Method and apparatus for the acceleration of ions**, February 20 1934. US Patent 1,948,384.
- [17] K STRIJCKMANS. **The isochronous cyclotron: principles and recent developments**. *Computerized Medical Imaging and Graphics*, **25**(2):69–78, 2001.
- [18] LH. THOMAS. **The Paths of Ions in the Cyclotron I. Orbits in the Magnetic Field**. *Physical Review*, **54**(8):580, 1938.
- [19] H. L. HAGEDOORN AND N. F. VERSTER. **Orbits in an AVF cyclotron**. *Nuclear Instruments and Methods*, **18**:201–228, 1962.
- [20] MIKE SEIDEL. **Cyclotrons for high-intensity beams**. Technical report, CERN, 2013.
- [21] M SEIDEL AND PA SCHMELZBACH. **Upgrade of the PSI Cyclotron Facility to 1.8 MW**. *Proc. Cycl. and their Appl*, 2007.
- [22] J REGINALD RICHARDSON, KR MACKENZIE, EJ LOFAREN, AND BYRON T WRIGHT. **Frequency modulated cyclotron**. *Physical Review*, **69**(11-12):669, 1946.
- [23] K GALL, S ROSENTHAL, G ROW, AND M AHEARN. **Inner gantry**, December 23 2014. US Patent 8,916,843.
- [24] TH STAMMBACH. **Introduction to cyclotrons**. In *Proceedings of the CERN Accelerator School, La Hulpe, Belgium*, pages 113–138. CERN, 1994.

- 
- [25] WB POWELL AND BL REECE. **Injection of Ions into a Cyclotron from an External Source.** *Nuclear Instruments and Methods*, **32**(2):325–332, 1965.
- [26] DJ CLARK. **Survey of external injection systems for cyclotrons.** In *Proceedings of the 5th International Cyclotron Conference*, **C690917**, pages 583–601, 1969.
- [27] W KLEEVEN. **Injection and extraction for cyclotrons.** In *Proceedings of the CERN Accelerator School, Jyväskylä, Finland*, pages 819–838. CERN, 1992.
- [28] J BELMONT AND JL PABOT. **Study of Axial Injection for the Grenoble Cyclotron.** *IEEE Trans. Nucl. Sci., NS-13*, **191**, 1966.
- [29] LJ MILINKOVIC, D TOPREK, AND B BRAJUSKOVIC. **Injection and central region studies for the VINCY Cyclotron.** In *Proceedings of the Third European Particle Accelerator Conference, Berlin*, **2**, page 1516, 1992.
- [30] RW MÜLLER. **Novel inflectors for cyclic accelerators.** *Nuclear Instruments and Methods*, **54**(1):29–41, 1967.
- [31] J BELMONT. **Ion transport from the source to first cyclotron orbit.** *Nukleonika*, **48**:13–20, 2003.
- [32] R BEURTEY AND J THIRION. **Sur une methode d’injection de particules polarisees dans un cyclotron ou un synchrocyclotron.** *Nuclear Instruments and Methods*, **33**:338–338, 1965.
- [33] VA GLADYSHEV, LN KATSAUROV, AN KUZNETSOV, LP MARTYNOVA, AND EM MOROZ. **Introduction of an ion beam into the cyclotron.** *Soviet Atomic Energy*, **18**(3):268–273, 1965.
- [34] WG DAVIES AND AR RUTLEDGE. **Design of the injection system for the Chalk River superconducting cyclotron project.** *IEEE Transactions on Nuclear Science*, **26**(2):2086–2089, 1979.
- [35] JH NEILER AND WM GOOD. **Fast neutron physics.** *Wiley (Interscience)*, New York, 1960.
- [36] WT MILNER. **Double-drift beam bunching systems.** *IEEE Transactions on Nuclear Science*, **26**(1):1445–1449, 1979.

## REFERENCES

---

- [37] RR WILSON AND MD KAMEN. **Internal targets in the cyclotron.** *Physical Review*, **54**(12):1031, 1938.
- [38] J BOTMAN AND HL HAGEDOORN. **Extraction from cyclotrons.** *CERN Accelerator School*, 1996.
- [39] J REGINALD RICHARDSON, EW BLACKMORE, G DUTTO, CJ KOST, GH MACKENZIE, AND MK CRADDOCK. **Production of simultaneous, variable energy beams from the TRIUMF cyclotron.** *IEEE Transactions on Nuclear Science*, **22**(3):1402–1407, 1975.
- [40] WM POWELL. **Beam extractor**, January 20 1953. US Patent 2,626,351.
- [41] JS GOODEN, HH JENSEN, AND JL SYMONDS. **Theory of the proton synchrotron.** *Proceedings of the Physical Society*, **59**(4):677, 1947.
- [42] BJ HOLZER. **Lattice design in high-energy particle accelerators.** *CERN Accelerator School*, 2016.
- [43] T SUZUKI. **Equations of motion and Hamiltonian for synchrotron oscillations and synchro-betatron coupling.** Technical report, KEK, 1996.
- [44] KR SYMON. **MURA days.** In *Proceedings of the 2003 Particle Accelerator Conference*, **1**, pages 452–456. IEEE, 2003.
- [45] LW JONES AND KM TERWILLIGER. **A Note on the accelerated beam obtained in the Michigan radial sector FFAG electron model.** Technical report, MURA, 1956.
- [46] DW KERST, HJ HAUSMAN, RO HAXBY, LJ LASLETT, FE MILLS, T OHKAWA, FL PETERSON, AM SESSLER, JN SNYDER, AND WA WALLENMEYER. **Operation of a spiral sector fixed field alternating gradient accelerator.** *Review of Scientific Instruments*, **28**(11):970–971, 1957.
- [47] KR SYMON AND MURA STAFF. **The Mura Two-Way Electron Accelerator.** In *Proceedings of the 2nd International Conference on High-Energy Accelerators and Instrumentation*, CERN, Geneva, Switzerland, pages 71–76, 1959.
- [48] JS BERG. **Recent results from optimization studies of linear non-scaling FFAGs for muon acceleration.** Technical report, BNL, 2004.

- 
- [49] S KOSCIELNIAK AND C JOHNSTONE. **Longitudinal dynamics in an FFAG accelerator under conditions of rapid acceleration and fixed, high RF.** In *Proceedings of the Particle Accelerator Conference*, **3**, pages 1831–1833. IEEE, 2003.
- [50] C JOHNSTONE, M BERZ, K MAKINO, S KOSCIELNIAK, AND P SNOPOK. **Advances in nonlinear non-scaling FFAGs.** *International Journal of Modern Physics A*, **26**(10n11):1690–1712, 2011.
- [51] N HERVÉ, N OLIVIER, AND D SYLVAIN. *Accelerator driven subcritical reactors.* CRC Press, 2003.
- [52] M AIBA ET AL. **Development of a FFAG proton synchrotron.** In *Proceedings of EPAC*, **581**, 2000.
- [53] M YOSHIMOTO ET AL. **Recent beam studies of the PoP FFAG proton synchrotron.** In *Proceedings of the 2001 Particle Accelerator Conference*, **1**, pages 51–53. IEEE, 2001.
- [54] M WATANABE, Y CHIBA, T KATAYAMA, T KOSEKI, K OHTOMO, AND H TSUTSUI. **Measurement of RF characteristics of magnetic alloys for an RF cavity of the accumulator cooler ring.** *Nuclear Instruments and Methods in Physics Research Section A: Accelerators, Spectrometers, Detectors and Associated Equipment*, **532**(1-2):503–507, 2004.
- [55] S MACHIDA ET AL. **Commissioning of 150MeV FFAG synchrotron.** In *proceedings of the 2004 European Accelerator Conference*, 2004.
- [56] M TANIGAKI, K MISHIMA, S SHIROYA, Y ISHI, S FUKUMOTO, Y MORI, S MACHIDA, AND M INOUE. **Construction of FFAG accelerators in KURRI for ADS study.** In *Proceedings of the 2005 Particle Accelerator Conference*, pages 350–352. IEEE, 2005.
- [57] SL SHEEHY ET AL. **Characterization techniques for fixed-field alternating gradient accelerators and beam studies using the KURRI 150 MeV proton FFAG.** *Progress of Theoretical and Experimental Physics*, (7), 2016.
- [58] CH PYEON. **Accelerator-Driven System (ADS) Study in Kyoto University Research Reactor Institute (KURRI).** In *Nuclear Back-end and Transmutation Technology for Waste Disposal*, pages 81–91. Springer, 2015.

## REFERENCES

---

- [59] T ADACHI ET AL. **A 150 MeV FFAG synchrotron with "Return-Yoke Free" magnet.** In *Proceedings of the 2001 Particle Accelerator Conference*, **5**, pages 3254–3256. IEEE, 2001.
- [60] T UESUGI ET AL. **Emittance Growth at Charge-Exchanging Multi-Turn Injection in KURRI FFAG.** In *Proceeding of the 8th International Particle Accelerator Conference: Copenhagen, Denmark*, pages 3747–3749. JACoW, 2017.
- [61] RF BARTH, JA CODERRE, MGH VICENTE, AND TE BLUE. **Boron neutron capture therapy of cancer: current status and future prospects.** *Clinical Cancer Research*, **11**(11):3987–4002, 2005.
- [62] K OKABE, T UESUGI, Y KURIYAMA, T PLANCHE, JB LAGRANGE, Y ISHI, I SAKAI, AND Y MORI. **Design and construction of FFAG magnets for the ERIT system at KURRI.** *IEEE Transactions on Applied Superconductivity*, **20**(3):740–743, 2010.
- [63] Y MORI, Y ISHI, Y KURIYAMA, Y SAKURAI, T UESUGI, K OKABE, AND I SAKAI. **Neutron source with emittance recovery internal target.** In *Proceedings of the 2009 Particle Accelerator Conference*, pages 3145–3147, 2009.
- [64] K OKABE, M MUTO, AND Y MORI. **Recent Studies of the FFAG-ERIT System for BNCT.** In *Proceedings of the 2009 Particle Accelerator Conference*, 2009.
- [65] D MÖHL AND AM SESSLER. **Beam cooling: principles and achievements.** *Nuclear Instruments and Methods in Physics Research Section A: Accelerators, Spectrometers, Detectors and Associated Equipment*, **532**(1-2):1–10, 2004.
- [66] S MACHIDA ET AL. **Acceleration in the linear non-scaling fixed-field alternating-gradient accelerator EMMA.** *Nature Physics*, **8**(3):243, 2012.
- [67] JM GARLAND, BD MURATORI, HL OWEN, AND JW MCKENZIE. **Characterisation of the ALICE Accelerator as an Injector for the EMMA ns-FFAG.** In *Proceeding of the 1st International Particle Accelerator Conference: Kyoto, Japan*. JACoW, 2010.
- [68] BD MURATORI, SL SMITH, SI TZENOV, AND C JOHNSTONE. **Injection and Extraction for the EMMA NS-FFAG.** In *Proc. EPAC08, Genoa*, 2008.

- 
- [69] R BARLOW ET AL. **EMMA-The worlds first non-scaling FFAG**. *Nuclear Instruments and Methods in Physics Research Section A: Accelerators, Spectrometers, Detectors and Associated Equipment*, **624**(1):1–19, 2010.
- [70] DJ KELLIHER AND S MACHIDA. **Orbit Distortion and its Correction in a Non-scaling FFAG**. In *Proceedings of EPAC08*, 2008.
- [71] CD BEARD, N BLISS, SA GRIFFITHS, C HILL, PA MCINTOSH, A MOSS, A WHEELHOUSE, C WHITE, AND D TEYTELMAN. **RF system design for the EMMA FFAG**. In *Proceedings of EPAC 2008, Genoa, Italy*. IET, 2008.
- [72] S MACHIDA ET AL. **First results from the EMMA experiment**. In *Proceedings of the 2nd International Particle Accelerator Conference*, 2011.
- [73] J GARLAND, H OWEN, D KELLIHER, S MACHIDA, AND BD MURATORI. **An Experimental Investigation of Slow Integer Tune Crossing in the EMMA Non-scaling FFAG**. In *Proceedings of the 3rd International Particle Accelerator Conference*, 2012.
- [74] J TAYLOR, T EDGECOCK, S GREEN, AND C JOHNSTONE. **HEATHER-HELIUM Ion Accelerator for RadioTHERapy**. In *Proceeding of the 8th International Particle Accelerator Conference: Copenhagen, Denmark*, pages 4768–4771. JACoW, 2017.
- [75] R APPLEBY, S TYGIER, K HOCK, J GARLAND, AND H OWEN. **NORMA-The Normal-Conducting, Scaling Racetrack FFAG**. In *Proceeding of the 5th International Particle Accelerator Conference: Dresden, Germany*. JACoW, 2014.
- [76] D TRBOJEVIC, S BROOKS, W LOU, B PARKER, AND N TSOUHAS. **Permanent Halbach Magnet Proton and Superconducting Carbon Cancer Therapy Gantries**. In *Proceeding of the 8th International Particle Accelerator Conference: Copenhagen, Denmark*, pages 4679–4682. JACoW, 2017.
- [77] Y ISHI ET AL. **Future Plans of ADS Proton Drivers at Kyoto University Research Reactor Institute**. In *Proceeding of the 8th International Particle Accelerator Conference: Copenhagen, Denmark*, pages 4695–4697. JACoW, 2017.
- [78] S SHEEHY AND C JOHNSTONE. **A 1 GeV CW FFAG High Intensity Proton Driver**. In *Proceeding of the 3rd International Particle Accelerator Conference: New Orleans, Louisiana, USA*. JACoW, 2012.

## REFERENCES

---

- [79] GH REES. **Non-isochronous and isochronous, non-scaling, FFAg designs.** In *Proceedings of the 18th International Conference on Cyclotrons and their Applications, Sicily, MOP1197*, pages 189–192, 2007.
- [80] CR PRIOR. **Studies of High Intensity Proton FFAGs at RAL.** In *Proceedings of the 57th ICFA Advanced Beam Dynamics Workshop on High-Intensity and High-Brightness Hadron Beams, Malmo, Sweden*, 2016.
- [81] R BARLOW, JK POZIMSKI, K PEACH, N BLISS, N MARKS, H OWEN, MW POOLE, AND TR EDGECOCK. **The CONFORM project: Construction of a nonscaling FFAg and its applications.** In *Proceedings of the 2007 Particle Accelerator Conference, Albuquerque, New Mexico, USA*, 2007.
- [82] KJ PEACH ET AL. **PAMELA overview: design goals and principles.** In *Proceedings of the 2009 Particle Accelerator Conference, Vancouver, Canada*. JACoW, 2009.
- [83] S SHEEHY, K PEACH, H WITTE, T YOKOI, D KELLIHER, AND S MACHIDA. **PAMELA Lattice Design and Performance.** In *Proceedings of the 2009 Particle Accelerator Conference, Vancouver, Canada*, 2009.
- [84] KJ PEACH ET AL. **PAMELA: Overview and status.** In *Proceeding of the 1st International Particle Accelerator Conference: Kyoto, Japan*. JACoW, 2010.
- [85] DI MEYER AND R FLASCK. **A new configuration for a dipole magnet for use in high energy physics applications.** *Nucl. Instrum. Methods 80: 339-41(1970).*, 1970.
- [86] M HARRISON, T LUDLAM, AND S OZAKI. **RHIC project overview.** *Nuclear Instruments and Methods in Physics Research Section A: Accelerators, Spectrometers, Detectors and Associated Equipment*, **499(2-3):235–244**, 2003.
- [87] V PTITSYN AND eRHIC COLLABORATION. **eRHICFuture Electron-Ion Collider at BNL.** In *AIP Conference Proceedings*, **842**, pages 1046–1048. AIP, 2006.
- [88] L MERMINGA. **Energy-Recovery Linacs.** *Synchrotron Light Sources and Free-Electron Lasers: Accelerator Physics, Instrumentation and Science Applications*, pages 1–33, 2014.

- 
- [89] D TRBOJEVIC ET AL. **ERL with non-scaling fixed field alternating gradient lattice for eRHIC**. In *Proceeding of the 6th International Particle Accelerator Conference: Richmond, Virginia, USA*. JACoW, 2015.
- [90] EC ASCHENAUER ET AL. **eRHIC design study: an electron-ion collider at BNL**. *arXiv preprint arXiv:1409.1633*, 2014.
- [91] K HALBACH. **Design of permanent multipole magnets with oriented rare earth cobalt material**. *Nuclear instruments and methods*, **169**(1):1–10, 1980.
- [92] H WITTE, JS BERG, N TSOUHAS, J CINTORINO, G MAHLER, AND P WANDERER. **A permanent magnet quadrupole magnet for CBETA**. In *Proceeding of the 8th International Particle Accelerator Conference: Copenhagen, Denmark*. JACoW, 2017.
- [93] D TRBOJEVIC ET AL. **CBETA-Cornell University Brookhaven National Laboratory electron energy recovery test accelerator**. In *Proceeding of the 8th International Particle Accelerator Conference: Copenhagen, Denmark*, pages 1285–1289. JACoW, 2017.
- [94] G HOFFSTAETTER, D TRBOJEVIC, AND C MAYES. **CBETA Design Report**. Technical report, Brookhaven National Laboratory (BNL), Upton, NY (United States), 2017.
- [95] B SINGH, J SINGH, AND A KAUR. **Applications of radioisotopes in agriculture**. *International J. of Biotechnol. Bioeng. Res*, **4**(3):167–174, 2013.
- [96] JS CHARLTON, JA HESLOP, AND P JOHNSON. **Industrial applications of radioisotopes**. *Physics in technology*, **6**(2):67, 1975.
- [97] S SAHOO AND S SAHOO. **Production and applications of radioisotopes**. *Physics Education*, **5**, 2006.
- [98] PM DEVLIN. *Brachytherapy: applications and techniques*. Springer Publishing Company, 2015.
- [99] A GERBAULET. *The GEC ESTRO handbook of brachytherapy*. Estro Brussels, 2002.
- [100] G VAIDYANATHAN AND MR ZALUTSKY. **Applications of  $^{211}\text{At}$  and  $^{223}\text{Ra}$  in targeted alpha-particle radiotherapy**. *Current radiopharmaceuticals*, **4**(4):283–294, 2011.

## REFERENCES

---

- [101] F GUÉRARD, JF GESTIN, AND MW BRECHBIEL. **Production of [211At]-astatinated radiopharmaceuticals and applications in targeted  $\alpha$ -particle therapy.** *Cancer Biotherapy and Radiopharmaceuticals*, **28**(1):1–20, 2013.
- [102] GB SAHA. *Basics of PET imaging: physics, chemistry, and regulations*. Springer, 2015.
- [103] MN WERNICK AND JN AARSVOLD. *Emission tomography: the fundamentals of PET and SPECT*. Elsevier, 2004.
- [104] **Cyclotron produced radionuclides: Principles and practice.** Technical report, International Atomic Energy Agency, Vienna, 2008.
- [105] B PONSARD. **Mo-99 supply issues: Status report and lessons learned.** Technical report, INIS-BE–10K0001, 2010.
- [106] CS CUTLER AND SW SCHWARZ. **Diversification in the supply chain of 99Mo ensures a future for 99mTc.** *J Nucl Med*, **55**(7):1208–1213, 2014.
- [107] MC LAGUNAS-SOLAR, PM KIEFER, OF CARVACHO, CA LAGUNAS, AND YP CHA. **Cyclotron production of NCA 99mTc and 99Mo. An alternative non-reactor supply source of instant 99mTc and 99Mo 99mTc generators.** *International Journal of Radiation Applications and Instrumentation. Part A. Applied Radiation and Isotopes*, **42**(7):643–657, 1991.
- [108] A CELLER, X HOU, F BÉNARD, AND T RUTH. **Theoretical modeling of yields for proton-induced reactions on natural and enriched molybdenum targets.** *Physics in Medicine & Biology*, **56**(17):5469, 2011.
- [109] H FUKUDA ET AL. **Experimental study for cancer diagnosis with positron-labeled fluorinated glucose analogs:[18 F]-2-fluoro-2-deoxy-D-mannose: A new tracer for cancer detection.** *European journal of nuclear medicine*, **7**(7):294–297, 1982.
- [110] DE GROOM AND SR KLEIN. **Passage of particles through matter.** *The European Physical Journal C-Particles and Fields*, **15**(1-4):163–173, 2000.
- [111] AA ALHARBI ET AL. *Radioisotopes-Applications in Bio-Medical Science*. InTech, 2011.

- 
- [112] RH LARSEN, BW WIELAND, AND MR ZALUTSKY. **Evaluation of an internal cyclotron target for the production of  $^{211}\text{At}$  via the  $^{209}\text{Bi}(\alpha, 2n)^{211}\text{At}$  reaction.** *Applied radiation and isotopes*, **47**(2):135–143, 1996.
- [113] M BERZ AND OTHERS. **COSY INFINITY version 9.1 programmers manual.** Technical report, Michigan State University, East Lansing, SUHEP-101214, 2011.
- [114] A ADELMANN AND OTHERS. **The OPAL (Object Oriented Parallel Accelerator Library) Framework.** Technical report, Paul Scherrer Institut, PSI-PR-08-02, 2008-2014.
- [115] DANIEL WINKLEHNER, ANDREAS ADELMANN, ACHIM GSELL, TULIN KAMAN, AND DANIELA CAMPO. **Realistic simulations of a cyclotron spiral inflector within a particle-in-cell framework.** *Physical Review Accelerators and Beams*, **20**(12):124201, 2017.
- [116] S TYGIER AND D KELLIHER. **PyZgoubi.** <http://sourceforge.net/projects/pyzgoubi/>. accessed 2018.
- [117] F MEOT. **Zgoubi.** <https://sourceforge.net/projects/zgoubi/>. accessed 2018.
- [118] M ET AL SEIDEL. **Production of a 1.3 MW proton beam at PSI.** In *Proceeding of the 1st International Particle Accelerator Conference: Kyoto, Japan*, page 1309. JACoW, 2010.
- [119] RE LAXDAL, A ALTMAN, AND T KUO. **Beam measurements on a small commercial cyclotron.** Technical report, CM-P00068425, 1994.
- [120] L MEDEIROS ROMAO, M ABS, JC AMELIA, W BEECKMAN, JL DELVAUX, Y JONGEN, W KLEEVEN, Y PARADIS, D VANDEPLASSCHE, AND S ZAREMBA. **IBA C70 cyclotron development.** In *Conference on Cyclotrons and their Applications*, 2007.
- [121] AW CHAO. *Physics of collective beam instabilities in high energy accelerators.* Wiley, 1993.
- [122] T PLANCHE, Y-N RAO, AND R BAARTMAN. **Space Charge Effects in Isochronous FFAGs and Cyclotrons.** *Proceedings of HB2012*, pages 231–234, 2012.

## REFERENCES

---

- [123] HG BLOSSER. **Problems and Performance in the Cyclotron Central Region.** *IEEE Transactions on Nuclear Science* 13.4, **13.4**:1–13, 1966.
- [124] TH STAMMBACH, S ADAM, HR FITZE, W JOHO, M MÄRKI, M OLIVO, L REZZONICO, P SIGG, AND U SCHRYBER. **The feasibility of high power cyclotrons.** *Nuclear Instruments and Methods in Physics Research Section B: Beam Interactions with Materials and Atoms*, **113**(1-4):1–7, 1996.
- [125] K HATANAKA ET AL. **Upgrade Project of the RCNP AVF Cyclotron Facility.** *Proceedings of Cyclotrons 2004, Tokyo, Japan, 2004.*
- [126] MM GORDON. **The longitudinal space charge effect and energy resolution.** In *Proceedings of the 5th International cyclotron conference-Oxford*, 1969.
- [127] BEST CYCLOTRON. **Best 30p Cyclotron.** [http://www.bestcyclotron.com/product\\_30p.html](http://www.bestcyclotron.com/product_30p.html). accessed 2018.
- [128] ACS. **ACS TR-30.** <http://www.advancedcyclotron.com/cyclotron-solutions/tr30>. accessed 2018.
- [129] IBA. **IBA Cyclone 30.** [https://www.iba-radiopharmasolutions.com/sites/default/files/resources/files/cbr\\_c30\\_v5\\_r00.pdf](https://www.iba-radiopharmasolutions.com/sites/default/files/resources/files/cbr_c30_v5_r00.pdf). accessed 2018.
- [130] K OKABE, Y MORI, Y ISHI, AND T UESUGI. **Study of FFAG-ERIT neutron source.** In *1st International Particle Accelerator Conference*, pages 418–420, 2010.
- [131] ANKENBRANDT ET AL. **Status of muon collider research and development and future plans.** *Physical Review Special Topics-Accelerators and Beams*, **2**(8):081001, 1999.
- [132] M BOGOMILOV ET AL. **The MICE Muon Beam on ISIS and the beam-line instrumentation of the Muon Ionization Cooling Experiment.** *Journal of Instrumentation*, **7**(05):P05009, 2012.
- [133] C RUBBIA, A FERRARI, Y KADI, AND V VLACHOUDIS. **Beam cooling with ionization losses.** *Nuclear Instruments and Methods in Physics Research Section A: Accelerators, Spectrometers, Detectors and Associated Equipment*, **568**(2):475–487, 2006.

- 
- [134] C ROGERS ET AL. **Solenoidal Focussing Internal Target Ring**. In *Proceeding of the 8th International Particle Accelerator Conference: Copenhagen, Denmark*, pages 1757–1759. JACoW, 2017.
- [135] D BRUTON, R BARLOW, T EDGECOCK, AND C JOHNSTONE. **Thin Internal target studies in a Compact FFAG**. In *Proceeding of the 8th International Particle Accelerator Conference: Copenhagen, Denmark*, pages 2411–2413. JACoW, 2017.
- [136] JD ANDERSSON, B THOMAS, SV SELIVANOVA, E BERTHELETTE, JS WILSON, AJB MCEWAN, AND K GAGNON. **Robust high-yield  $\sim 1$  TBq production of cyclotron based sodium [ $^{99m}\text{Tc}$ ] pertechnetate**. *Nuclear medicine and biology*, **60**:63–70, 2018.
- [137] DW KERST, LAWRENCE W JONES, KR SYMON, AND KM TERWILLIGER. **A Fixed field alternating gradient accelerator with spirally ridged poles**. Technical report, MURA, 1954.
- [138] PK SIGG. **RF for cyclotrons**. In *Proceedings of the CERN Accelerator School*. CERN, 2006.
- [139] M DUVAL, MP BOURGAREL, AND F RIPOUTEAU. **New compact cyclotron design for SPIRAL**. *IEEE Transactions on Magnetics*, **32**(4):2194–2196, 1996.
- [140] ME ROSE. **Magnetic field corrections in the cyclotron**. *Physical Review*, **53**(9):715, 1938.
- [141] A CALANNA, L CALABRETTA, R JOHNSON, L PIAZZA, V SABAUDUC, AND T BOIESAN. **Compact Cyclotron for 35 MeV Protons and 8 AMeV of  $\text{H}^2$** . In *Proceeding of the 6th International Particle Accelerator Conference: Richmond, Virginia, USA*, 2015.
- [142] K MASUMOTO, T FUJIBUCHI, K KUGA, T FUKUMURA, A TOYODA, S SATO, H NAKAMURA, H IIDUKA, AND M SASAKI. **Effectiveness of self-shielding type cyclotrons**. *Prog. Nucl. Sci. Tech.*, **4**:223–227, 2014.